University of Stuttgart
Institute of Nuclear Technology
and Energy Systems

Direct Numerical Simulation of Heat Transfer to Supercritical Carbon Dioxide in Pipe Flows

Xu Chu

December 2016 IKE 8-125

IKE

University of Stuttgart
Institute of Nuclear Technology
and Energy Systems

Direct Numerical Simulation of Heat Transfer to Supercritical Carbon Dioxide in Pipe Flows

von der Fakultät 4: Energie-, Verfahrens- und Biotechnik der Universität Stuttgart zur Erlangung der Würde eines Doktor-Ingenieurs (Dr.-Ing.) genehmigte Abhandlung

vorgelegt von
Dipl.-Ing. Xu Chu
aus Anshan, China

Hauptberichter: Prof. Dr.-Ing. habil. Eckart Laurien

Mitberichter: Prof. Dr.-Ing. habil. Ulrich Rist

Tag der mündlichen Prüfung: 02.12.2016

Erscheinungsjahr: 2016

ISSN-Nr: 0173-6892

Danksagungen

I would like to express my gratitude to my Doktorvater, Prof. Eckart Laurien, for offering me the opportunity to work with him on a number of exciting problems that eventually constitute this thesis. I am constantly surprised by his intelligence, creativity and sense of responsibility. I always feel fortunate to have his support and advice along the way.

I also thank Prof. Ulrich Rist for many interesting and insightful discussions that broaden my view of research, especially in giving me suggestions on a number of challenging problems.

It was a great pleasure working with Prof. Starflinger and all my colleagues in IKE. It is very enjoyable to be a member of IKE family.

Abstract

Turbulent heat transfer of supercritical carbon dioxide in pipe flow is investigated using Direct Numerical Simulation (DNS). A numerical solver based on the open-source code OpenFOAM is developed and runs parallel efficiently on high-performance computing (HPC) platforms. The numerical method is initially validated with experiments of heated air flow from Shehata and McEligot [SM95], where flow relaminarization is observed in the strongly heated cases. A new semi-local wall coordinate is applied to replace the conventional one.

In the vertical pipe flows with supercritical CO_2, various simulation conditions are considered including forced-convection and upward and downward flow in the mixed convection. It is identified that both flow acceleration and buoyancy effect can result in significant turbulence modification. Flow relaminarization and transition are observed by various turbulence statistics in the upward flow in pipes. The turbulence structures are significantly modified with the disappearance of organized turbulent streaks.

In the horizontal pipe flows, buoyancy results in flow stratification with low density in the upper region and high density in the lower region of pipe. Low-velocity flow near the circumferential wall is heated firstly and transported to the top region by a secondary flow. The modification of the velocity field affects the shear production of turbulence near the top surface.

Therefore, the turbulent kinetic energy and the radial turbulent heat flux are strongly suppressed in this region. The attenuated convective heat transfer enhances the flow stratification.

The results of the present work contribute a data base for turbulence and heat transfer modeling, which is suitable for industrial applications.

Zusammenfassung

Der turbulente Wärmeübergang des superkritischen CO_2 in Rohrströmungen wird mit direkter numerischer Simulation (DNS) untersucht. Ein numerischer Solver wird basierend auf dem open source Code OpenFOAM entwickelt, der in effizienter Weise parallel auf Hochleistungsrechenplattfomen läuft. Die numerische Methode wird anfänglich an Experimenten heißer Luft von Sheheata und McEligot validiert, bei denen eine Re-Laminisierung der Strömung für den stark beheizten Fall beobachtet wurde. Hier wurde anstelle der konventionellen Wandkoordinate eine neue semi-lokale Wandkoordinate implementiert.

In vertikalen Rohrströmungen mit superkritischem CO_2 werden zahlreiche Simulationsbedingungen inklusive erzwungener Konvektion, sowie Auf- und Abwärtsströmungen betrachtet. Es wurde festgestellt, dass sowohl die Beschleunigung als auch die Auftriebskraft zu einer deutlichen Änderung der Turbulenz zur Folge hat. Strömungsrelaminarisierung und Transition können durch Betrachtung zahlreicher Turbulenzstatistiken bei Aufwärtsströmung beobachtet werden. Die Turbulenzstrukturen werden durch das Verschwinden turbulenter Strähnen deutlich verändert.

Bei horizontalen Rohrströmungen führt der Auftrieb zu Strömungsrelaminarisierung mit einer geringen Dichte im oberen, und höherer Dichte im unteren Bereich des Rohres. Strömungen mit niedriger Geschwindigkeit wer-

den in Wandnähe aufgeheizt und werden durch Sekundärströmungen nach oben transportiert. Die Veränderung des Geschwindigkeitsfeldes führt zu Turbulenzproduktion durch Scherung nahe der Oberseite. Deshalb werden die turbulente kinetische Energie und der radiale turbulente Wärmestrom in dieser Region stark gedämpft. Der abgeschwächte konvektive Wärmeübergang verstärkt die Strömungsrelaminarisierung.

Die Ergebnisse dieser Arbeit tragen ihren Teil zu einer Datenbasis für Turbulenz- und Wärmeübergangsmodellierung bei, die für industrielle Anwendungen geeignet sind.

Contents

Nomenclature

Latin Letters

C_p = specific heat capacity at constant pressure, J/kg K
D = pipe diameter, m
g = acceleration due to gravity, m/s^2
h = specific enthalpy, J/kg
P = pressure, MPa
q = heat flux, W/m^2
r = radius position, m
R = pipe radius, m
t = time, s
T = temperature, K
T_τ = friction temperature in conventional wall unit, $T_\tau = q_w/(\rho_w C_{p,w} U_\tau)$
U_i = velocity component, m/s
U_{VD} = velocity in Van Direst transformation $U_{VD} = \sqrt{\rho/\rho_w}U$
U_τ = friction velocity in conventional wall unit, $U_\tau = \sqrt{\tau_w/\rho_w}$
U_τ^* = friction velocity in semi-local wall unit, $U_\tau^* = \sqrt{\tau_w/\rho}$
y = normalized distance to the wall, $(R-r)/R$
z = streamwise position, m

Greek Letters

β = volume expansion coefficient, K^{-1}
η = Kolmogorov length scale
κ = thermal conductivity, W/m K
μ = dynamic viscosity, Pa s
ν = kinetic viscosity, m^2/s
ρ = density, kg/m^3
τ = viscous stress tensor
θ = circumferential direction in Cylindrical coordinate
ϕ = symbol for state variable

non-dimensional numbers

C_f = Skin friction coefficient
Gr = Grashof Number

K_v = Dimensionless Number for flow acceleration
Nu = Nusselt Number
Pr = Prandtl Number
Ri = Richardson Number
Re = Reynolds Number
Re_τ = turbulent Reynolds Number in conventional wall unit, $Re_\tau = \frac{U_\tau R}{\nu_b}$
Re^*_τ = turbulent Reynolds Number in semi-local wall unit, $Re^*_\tau = \frac{U^*_\tau R}{\nu}$
St = Stanton Number
y^+ = wall distance in conventional wall unit, $y^+ = yU_\tau/\nu_w$
y^* = wall distance in semi-local wall unit, $y^* = yU^*_\tau/\nu$
U^+ = dimensionless velocity, $U^+ = U/U_\tau$
U^+_{VD} = dimensionless velocity in Van Direst transformation, $U^+_{VD} = U_{VD}/U_\tau$
θ^+ = dimensionless temperature in conventional wall unit, $\theta^+ = (T_w - T)/T_\tau$
θ^* = dimensionless temperature in semi-local wall unit, $\theta^* = (T_w - T)/T_\tau$

Subscripts/Superscripts

b = bulk value
c = critical value
k = relevant terms for turbulent kinetic energy
min = minimal value
max = maxmal value
pc = pseudo-critical value
r = radial component
ref = reference temperature T and pressure P
rms = root mean squared
w = wall value
0 = inlet value
τ = turbulent value
θ = circumferential component

Acronyms

CFD = Computational Fluid Dynamics
DNS = Direct Numerical Simulation
HPC = High Performance Computing

HPLWR = High Performance Light Water Reactor
FDM = Finite Difference Method
FVM = Finite Volume Method
LES = Large eddy simulation
N-S = Navier-Stokes
PISO = Pressure implicit with splitting of operator
Pk = Production rate of turbulence from shear
RANS = Reynolds-averaged Navier Stokes
RK = Runge–Kutta
SCWR = Supercritical Water-Cooled Reactor
SEM = Spectral Element Method
TKE = Turbulent Kinetic Energy
TBL = Turbulent Boundary Layer
VHTR = Very-High-Temperature Reactor

Chapter 1

Introduction

1.1 Motivation

Using a supercritical fluid in a power cycle is widely considered as an advanced solution for energy conversion. High efficiency, compact size, and reduced complexity are the main advantages of these cycles [DDH04]. State-of-the art fossil power plants use the supercritical-water Rankine cycle to increase the thermal efficiency to about 45% [DP05], compared to sub-critical cycles with an efficiency up to 35%. The Supercritical Water-Cooled Reactor (SCWR) was chosen as one of Generation IV nuclear reactor concepts, which is also called as High Performance Light Water Reactor (HPLWR) in Europe [SSM+11]. Besides, supercritical carbon dioxide (CO_2) power cycles are being intensively investigated for high temperature solar, nuclear and fossil energy production [WRV+10]. Compared with water (critical pressure P_c=22.06 MPa, critical temperature T_c=647.1 K), CO_2 (P_c=7.38 MPa, T_c=304.1 K) has lower critical pressure and critical temperature [LMF+11]. Supercritical fluids have distinctive properties. At supercritical pressure, the fluid phase change from liquid to gas does not exist as in subcritical flows. When at constant supercritical pressure, the temperature rises above the

pseudo-critical point T_{pc}, the density ρ, the thermal conductivity κ and the dynamic viscosity μ decrease drastically, and the specific heat capacity C_p shows a peak value in a very narrow temperature range. Fig. 1.1 shows the variable properties of CO_2 as a function of the temperature T at a pressure $P = 8$ MPa, which is above the critical pressure. Dostal [DDH04] accomplished a systematic system design and multiple-parameter optimization for a supercritical CO_2 Brayton power cycle in the use of advanced nuclear reactors. The thermal efficiency of this advanced design is close to 50% and the reactor system with the direct supercritical CO_2 cycle is 24% less expensive than the steam indirect cycle. This idea and its relevant concepts are being considered by various applications e.g. concentrating solar power, geothermal and military usage [WRV+10]. Currently in the Institute of Nuclear Technology and Energy Systems (IKE) from the University of Stuttgart, a thermal loop with supercritical carbon dioxide (SCARLETT) is being built up for the systematic study of this concept, where also the computational results from the current DNS can be validated.

In the 1960s, the development of conventional fossil-fired power plants with water operating at supercritical pressure had led to research of convective heat transfer with supercritical fluids. Although the decreased heat transfer due to a critical heat flux can be excluded, the significant variation of thermo-physical properties can also lead to deteriorated heat transfer under certain conditions, which has been observed and confirmed by classical studies and also recent works [LAC09,KJL07,LJZZ10]. These experiments have been carried out mainly with supercritical water H_2O and carbon dioxide CO_2, in which CO_2 is chosen more often because of the advantages brought by its low critical pressure and temperature. Most of the experiments can only deliver measurement of the wall temperature of the pipe. Detailed flow turbulence information in the pipe can barely be found. The numerical approach based on the Reynolds-averaged Navier-Stokes Equations (RANS) is another way to investigate these phenomena. Extensive work has been performed by various authors [HKB08,PBSA15], but shows that classical turbulence models as well as advanced four-equation models, cannot reproduce this mechanisms well enough. Under this background, Direct Numerical

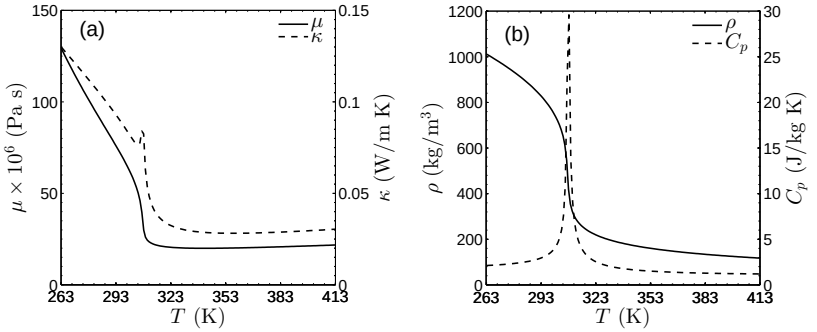

Figure 1.1: Variation of thermo-physical properties as a function of the temperature at a supercritical pressure of $P_0 = 8$ MPa, data from NIST data base [LMF+11]

Simulation (DNS), which aims to resolve all turbulence scales directly, i.e. without a turbulence model, is necessary. Unlike experiments, DNS provides us an insight view of the velocity and temperature fields of the flow, which is until now still rare in this area. It is obvious, that more insight through DNS is needed to study these phenomena, which combines a lot of interesting factors such as heat transfer with significantly variable thermo-physical properties, buoyancy effects, relaminarization and transition to turbulence.

1.2 Literature Review

1.2.1 Experiments

Heat transfer experiment with supercritical fluids were often performed in the vertical pipe, which is related to vertical flow in rod-bundles in a nuclear reactor core. The experiments introduced here are also limited to vertical tubes. The heat transfer deterioration and flow relaminarization was firstly confirmed in early works during the 1960s [SG69,HJ69,PPS72]. A review of these early works was written by Jackson [Jac13], and a more comprehensive one by Duffey and Pioro [DP05]. Recently, more experimental facilities with supercritical fluid (water, CO_2 and Freon) have been built. Some of the

representative works will be introduced here.

Li *et al.* [LJZZ10] introduced their work about heat transfer characteristics of supercritical CO_2 in a vertical pipe at a low inlet Reynolds number $Re_0 = 9000$. The Re_0 is significantly lower than other experiments and therefore shows potential to be used as validation data for DNS. In another publication from the same group, Jiang *et al.* [JLZL13] concluded that flow acceleration due to heating and pressure drop can strongly influence the turbulence and reduce the heat transfer for high heat fluxes and low inlet Reynolds numbers.

Bae and Kim [BK09] extended their experiments from circular tube to annular channel. From the test results, a correlation, which covers both a deteriorated and a normal heat transfer regime, was developed. Further non-circular tubes e.g. triangular and square cross-sections were employed by Kim *et al.* [KJL07b]. Based on the wall temperature data, they proposed an improved heat transfer correlation, which can be applicable to both forced convection and mixed convection regimes.

Licht *et al.* [LAC09] accomplished a series of integral heat transfer measurements with water in a vertical annulus. The bulk water temperature varied between 175–400°C with upward mass velocities of 300 kg/m^2 s and 1000 kg/m^2 s and heat fluxes of 0, 200 kW/m^2, and 440 kW/m^2, all at a pressure of 25 MPa. Valuable information of mean and fluctuating velocities was obtained with a two-component laser-Doppler velocimetry system, which distinguished this experiment from other ones with only wall temperature measurements. The experimentally measured heat transfer and velocity data also serve as a database to compare existing CFD models, such as RANS modeling and possibly even large Eddy simulations (LES) and DNS.

These experiments, however, provide little information about the turbulent structure and their development during heat transfer deterioration, nor can the mechanism of turbulence modification due to acceleration and gravity be identified.

1.2.2 Turbulence Modeling

During the last ten years, CFD simulation with turbulence modeling (RANS) becomes a common way to study the heat transfer character to supercritical fluids. A lot effort has been made to reproduce experimental results with different turbulence model from various numerical solvers. He *et al.* [HKB08] used $k-\epsilon$ and $v-f$ turbulence models using their 'inhouse' CFD code named SWIRL to simulate experiments by Fewster [Few76]. They also carried out a more comprehensive benchmark of models in [HKJ08] with reference to DNS data [HKB08]. They claimed that the $v-f$ model shows the most promising results of all candidates. More complex 4-equation turbulence models were tested by Pucciarelli *et al.* [PBSA15]. It was concluded that compared with common 2-equation models, complex 4-equation turbulence models provide limited improvements in the comparison with experimental data. Mohseni *et al.* [MB12] used a two dimensional CFD code to establish a modified $k-\epsilon$ turbulence model. Various areas of modifications have been tried. But the modeling of turbulence is still unresolved and unreliable. For the deteriorated regime of heat transfer, considerable improvements have been achieved. Bae [Bae16] described a procedure for a new formulation of the turbulent Prandtl number $\mathrm{Pr_t}$ which varies with physical properties and variable fluid–thermal variables instead of treating them as constant. This application shows improvement in reproducing the fluid temperature in supercritical fluids flowing in small-diameter vertical tubes.

Despite of the unresolved problem of turbulence modeling, more complex geometry and several other situation besides vertical circular pipe have been considered. Forooghi *et al.* [FADH15] used the commercial solver FLUENT to investigate the influence of buoyancy to the heat transfer of supercritical CO_2in inclined pipes. Furthermore, they extended their work to vertical concentric and eccentric annuli with the same numerical method [FH13a]. Corrugated channels, which are similar as the channels in a printed circuit heat exchanger (PCHE) were also studied in another work of his [FADH15]. Cheng *et al.* [CKY07] used ANSYS CFX as the numerical code. Three different flow channels are selected, i.e. circular tubes, the sub-channel of a square-

array rod bundles and the sub-channel of a triangular-array of rod bundles. Recently, Rohde *et al*. [RPP+16] reported a joint blind, numerical benchmark study on supercritical water heat transfer experiments in a 7-rod bundle. It described ten independent numerical investigations and their comparison with wall temperatures measured at different positions in a 7-rod bundle with spacer grids in a supercritical water test facility at Japan Atomic Energy Agency (JAEA). A number of models have been used, ranging from a one-dimensional (1-D) analytical approach with heat transfer correlations to a RANS simulation with the SST turbulence model on a mesh consisting of 62 million cells. None of the numerical simulations accurately predicted the wall temperature for the test case in which deterioration of heat transfer occurred. Therefore, it becomes obvious, that the RANS method is not able to reproduce heat transfer results in these cases currently.

1.2.3 Direct Numerical Simulation

Direct Numerical Simulation (DNS) enables us an insight view of the plenty turbulence statistics, which is until now still rare for flow with supercritical fluid. Bae *et al*. [BYC05] uses an in-house DNS code (second-order finite difference method (FDM) in cylindrical coordinate) for vertical pipe flow at $\mathrm{Re}_0 = U_0 D/\nu_0 = 5400$. The pipe diameter ranges from $D = 1$ mm to 3 mm. The inlet temperature T_0 is adjusted slightly lower than T_{pc}. In 2009, he reported another DNS work for annular pipe at $\mathrm{Re}_0 = 9000$ [BYCM06]. Recently, Nemati *et al*. [NPBP15] tried to reproduce the DNS from Bae *et al*. [BYC05] with their own code and higher resolution. But some discrepancy with the original one is observed.

Not restricted to supercritical fluid, heat transfer mechanism in incompressible turbulent flow has been discussed by different authors using DNS. Patel *et al*. [PPBP15] demonstrated the turbulence modulation of DNS channel flow with different constitutive relations for density and viscosity. The results are used to validate the newly introduced wall-coordinate for turbulent statistics. Zonta *et al*. [ZMS12] presented a systematic analysis of variable viscosity using a pseudo-spectral DNS of turbulent channel flow

with constant temperature difference between walls ,isolated from gravity. In another work, they analyzed the behavior of stably-stratified turbulent channel flow with temperature-dependent fluid properties: viscosity μ and thermal expansion coefficient β [ZOS12], with gravity. In the study of Lee *et al.* [LSHZ13], DNS of turbulent boundary layers (TBL) over isothermally heated walls were performed, and the effect of viscosity stratification on the turbulence statistics and skin friction were investigated.

With highly-resolved DNS, the heated turbulent pipe flow with supercritical fluid can be investigated without the uncertainty brought by turbulence modeling. DNS can also deliver a great number of flow statistics that are absent in the experimental output. Despite of the restriction in the DNS, e.g. low Reynolds-number, DNS is an optimal choice for our research objective. The statistics obtained from DNS can be used for developing or calibrating turbulence models.

1.3 Aim of this work

In the frame of this work, a numerical method should be developed in the first place, which is suitable for the high-performance computing. Open-source CFD package OpenFOAM [Ope15] has been implemented by a lot of researchers worldwide for solving various fluid mechanics problems [KSCK14,JUH15,VKDB14]. It shows a strong scalability on the parallel HPC system [VKDB14], with up to O(10^3) computation cores. For the DNS with variable-property fluid, no previous experience can be found in the existing literature. A series of code verification with other DNS results and experiments is necessary.

In this research thesis, heat transfer behavior of the supercritical fluid in the pipe flow is investigated using the developed DNS method. Various conditions are considered including forced-convection, upward and downward flow of mixed-convection and together with the horizontal pipes. Both vertical and horizontal flows have their industrial applications. The vertical flow is a common layout in the rod-bundles of the nuclear reactor concept. The

horizontal flow can be found in the printed circuit heat exchanger (PCHE), which is a key component in the design of a thermal cycle. The generated DNS data are being served for further turbulence modeling [PL16].

Chapter 2

Numerical Procedure for Direct Numerical Simulation

In this chapter, the numerical method for the current DNS will be introduced. The development of high performance computer (HPC) enables us to apply DNS for a broad range of researches. Besides in-house code, various open-source code are also available online nowadays, which can be employed for our research purpose with proper modifications. Apparently, they can shorten the code-developing time and they even surpass some of the in-house code by code quality and regular maintenance. OpenFOAM [Ope15] is a widely-used finite-volume-method (FVM) written in C++, originally developed by Imperial College in London. Another candidate of FVM code is Code Saturne developed by University of Manchester. A third choice will be a highly-scalable spectral-element-method (SEM) code Nek5000 [FLK16] developed by MIT in 1980s. This SEM code allows us to easily increase the code accuracy by employing higher-order Lagrange polynomial interpolants on

Gauss–Lobatto–Legendre (GLL) points. Besides these universal codes above, Incompact3D [LL11] is a DNS code based on 6-order compact difference method, which is superior to the 2-order accuracy of FVM.

Among these candidates, OpenFOAM owns the biggest user-group and its reliability has been proved by many researchers worldwide, which is convenient for usage. Therefore, we decide to develop our numerical method based on it. OpenFOAM has been applied for DNS by various authors [KSCK14,JUH15]. The DNS suitability was tested by Komen *et al.* [KSCK14] on simple pipe- and channel flows with turbulent Reynolds number Re_τ up to 395 based on channel half height/pipe radius. It was concluded that when hexahedral meshes are used, the differences between the OpenFOAM and the reference DNS solutions are the same as the mutual differences between these different reference DNS solutions. It can be expected that OpenFOAM is able to deliver similar DNS results as other second-order accurate DNS codes. Vuorinen *et al.* [VKDB14] implemented a low-dissipative, explicit Runge–Kutta (RK) based projection methods including classical fourth order RK-method and the accelerated third order RK-method as an alternative to standard Pressure Implicit with Splitting of Operator (PISO) algorithm in the distributed version. In the test cases of DNS turbulent channel flow, LES of a mixing layer and 2D inviscid Taylor–Green vortex, he stated that PISO is a relatively non-dissipative algorithm as well.

2.1 Integration Domain, Boundary Conditions

Fig. 2.1 shows the pipe geometry and boundary conditions in the present DNS. At the inlet, an inflow generator of the length $L_1 = 5D$ with an isothermal wall is adopted to generate approximately fully developed inflow turbulence. A recycling/rescaling procedure [LWS98] is applied in this domain, which does not require any priori knowledge of turbulent flow profiles. For accelerating the turbulence development, the velocity field is initialized with perturbation method introduced by Schoppa and Hussain [SH00]. In the second section of pipe $L_2 = 30D$, constant wall heat flux q_w is applied in the whole domain. It

should be mentioned that the applied wall heat flux q_w in the experiment can be only considered as approximately constant. The boundary condition of velocity field at outlet is the convective boundary condition $\frac{\partial \phi}{\partial t} + U_c \frac{\partial (\phi)}{\partial x} = 0$, where ϕ can be any dependent variable, e.g. velocity U. U_c represents the convective velocity to maintain the overall mass conservation. The direction of gravity g can be adjusted for vertical or horizontal flows.

The velocity inlet boundary condition (BC) of LES/DNS should be treated carefully. In many cases, the fluid behavior within the domain is determined largely by the inlet behavior. The inflow generator should generate the turbulence structure within a short pipe length. Besides, simplicity to implement and modify should also be considered. Tabor et al. [TB10] wrote a review of inlet boundary condition for LES/DNS based on OpenFOAM, including precursor simulation methods, internal mapping methods and different synthesis turbulent inflow generator. He concluded that although the synthesis inflow generator is easy to specify parameters of the turbulence, such as length scales or turbulent energy levels, it is inherently inaccurate, and requires long enough inlet development section. Precursor simulation methods produce true turbulence data and thus are inherently more accurate, however, can be cumbersome to modify to generate the required state of turbulence. The internal mapping method, also referred as recycling/rescaling method, is able to generate turbulent flow within relatively short distance. Besides, it is simple to adapt it to wide range of simulation conditions. The library method is often used in similar works by other authors [BYC05,NPBP15] and also in early works of current simulations[CL16a]. It was found that the turbulence statistics has a weak dependence on different implementation of inlet BC (recycling/rescaling method or library method). In order to run cases with different conditions (pipe diameter, inlet velocity) efficiently, the mapping inlet boundary condition is used instead.

A typical mesh system is depicted in Fig. 2.2, which consists of 62400 cells in the whole cross section. The resolution in radial and circumferential direction is about 160×480 respectively. The cell system consists of four blocks in the around and one block in the center, where the concentrated cells in the center of cross section can be avoided.

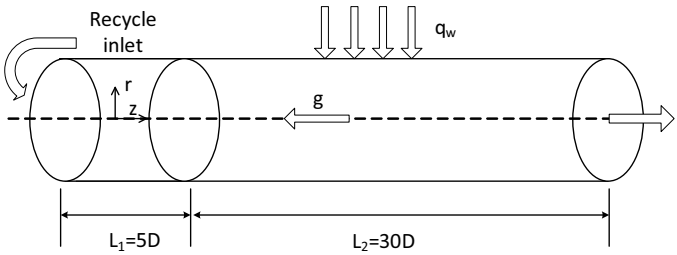

Figure 2.1: Flow domain and boundary conditions

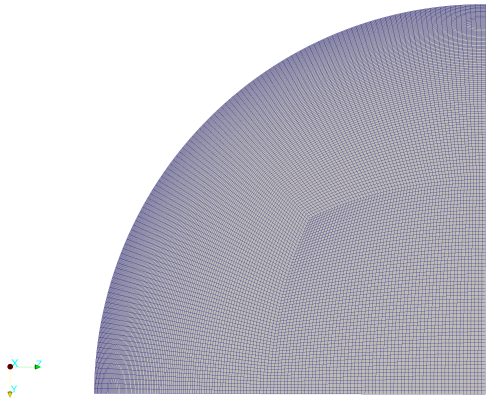

Figure 2.2: Cross-sectional view of a quarter-section of the computational mesh for the simulation

2.2 Governing Equations

Considering the significantly variable properties in low-speed number turbulent flow, Navier-Stokes (N-S) equations are constructed in low-Mach-number form (Eqns. 2.1-2.3), in which the compressibility effect is excluded from the full compressible N-S equations. Li *et .al* [LHT+08] uses the full compressible Navier-Stokes equations in his DNS of supercritical CO_2, and found that compressibility effects related to pressure fluctuation of velocity fluctuation

can be ignored. This form of governing equations is also applied by other authors [BYC05,NPBP15] in this area.

$$\frac{\partial \rho}{\partial t} + \nabla \cdot \rho U = 0 \tag{2.1}$$

$$\frac{\partial \rho U}{\partial t} + \nabla \cdot (\rho UU) = -\nabla P + \nabla \cdot (\mu \nabla U) \pm \rho g \delta_{i1} \tag{2.2}$$

$$\frac{\partial \rho h}{\partial t} + \nabla \cdot (\rho Uh) = \nabla \cdot (\kappa \nabla h) \tag{2.3}$$

$$h = h(P_0, T), \rho = \rho(P_0, T), \mu = \mu(P_0, T), C_p = C_p(P_0, T), \kappa = \kappa(P_0, T) \tag{2.4}$$

In Eqns. 2.1-2.3, t, U, P and h represent time, velocity, pressure and enthalpy respectively. ρ, μ and κ are the density, dynamic viscosity and thermo conductivity of the fluid properties.

2.3 Discretization

The equations are discretized and solved with OpenFOAM V2.4. To compute the derivatives of the velocity, the variables at the interfaces of the grid cells are obtained with linear interpolation. The temporal term is discretized with the second-order implicit Euler scheme. The spatial discretization is handled with central differencing scheme and a third-order upwind scheme QUICK is adopted for the convective term in the energy equation. The Pressure-Implicit with Splitting of Operators (PISO) algorithm introduced by Issa [Iss86] is applied for pressure-velocity coupling.

Fig. 2.3 demonstrates a typical control volume in the FVM discretization, where the length vector d is the distance between the center of the cell of

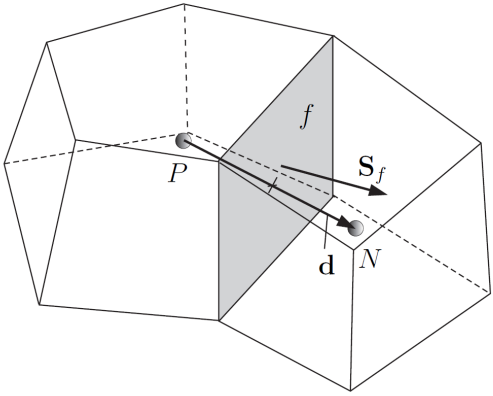

Figure 2.3: Control volumes of the FVM discretization

interest P and the center of a neighboring cell N. In the present FVM solver, the convective term is integrated over a control volume V and linearized as follows:

$$\int_V \nabla \cdot (\rho U \phi) dV = \int_S dS \cdot (\rho U \phi) = \sum_f S_f \cdot (\rho U)_f \phi_f = \sum_f F \phi_f \quad (2.5)$$

The Gauss'schen integration theorem is employed here with $F = S_f \cdot (\rho U)_f$ on cell surface area vector S. In Eqns. 2.1-2.3, the state variable ϕ denotes as $\phi = 1$, $\phi = U$ and $\phi = h$ respectively. The face value ϕ_f needs to be evaluated with neighboring cell values. In a central differencing scheme, $\phi_f = f_x \phi_P + (1 - f_x)\phi_N$, where $f_x = \overline{fN}/|d|$. And $\overline{fN}$ is the distance between face f and cell center P.

Similarly, the discretization of Laplacian term (Eqn. 2.2) in a control

volume reads as:

$$\int_V \nabla \cdot (\Gamma \nabla \phi) dV = \int_S dS \cdot (\Gamma \nabla \phi) = \sum_f \Gamma_f S_f \cdot (\nabla \phi)_f \tag{2.6}$$

where the face gradient discretization is implicit using:

$$S_f \cdot (\nabla \phi)_f = |S_f| \frac{\phi_N - \phi_P}{|d|} \tag{2.7}$$

The integration of time derivative $\partial / \partial t$ in a control volume is discretized as a source term:

$$\int_t^{t+\Delta t} \frac{\partial}{\partial t} (\int_V \rho \phi dV) dt = \frac{(\rho_P \phi_P V)^{t+\Delta t} - (\rho_P \phi_P V)^t}{\Delta t} \Delta t \tag{2.8}$$

Now, the discretized continuity equation and momentum equation are in the form of

$$(\rho_P V)^{t+\Delta t} - (\rho_P V)^t + \sum_{f=1}^{N} S_f \cdot (\rho U)_f = 0 \tag{2.9}$$

$$(\rho_P U_p V)^{t+\Delta t} - (\rho_P U_p V)^t + \sum_{f=1}^{N} S_f (\rho U U)_f = -\nabla P V + \sum_f \mu_f S_f \cdot (\nabla U)_f + S u_P \tag{2.10}$$

It is obvious that the convective term and Laplacian term consist of velocity field in the cell of interest P and its neighbors. A reorgnized form of the

discretized momentum equation is written as:

$$a_P U_P = \sum_N a_N U_N + S u_p + \nabla P \tag{2.11}$$

Where U_P is the velocity of cell P and U_N indicates the velocity field of the neighbor, while a_N and a_P are their factors. Considering the buoyancy force, P_{rgh} is defined: $P_{rgh} = P - \rho g \cdot z$, z is the height in the gravitational direction. Therefore,

$$\begin{aligned} \nabla P &= \nabla P_{rgh} + g \cdot \nabla \rho z \\ &= \nabla P_{rgh} + g\rho(\nabla z) + gz(\nabla \rho) \\ &= \nabla P_{rgh} + \rho g + gz(\nabla \rho) \end{aligned} \tag{2.12}$$

As a result, the momentum equation Eqn. 2.10 combined with Eqn. 2.11 and Eqn. 2.12 becomes

$$a_P U_P = \sum_N a_N U_N + S u'_P - (\nabla P_{rgh} + g \cdot z \nabla \rho) \tag{2.13}$$

Introducing a new operator $H(u) = \sum_N a_N^u U_N + S u'_p$, so that:

$$\begin{aligned} a_P U_P &= H(u) - (\nabla P_{rgh} + g \cdot z(\nabla \rho)) \\ U_P &= (\frac{H(u)}{a_p}) - (\frac{1}{a_p})(\nabla P_{rgh} + gz(\nabla \rho)) \end{aligned} \tag{2.14}$$

Similarly, the velocity on the cell faces becomes:

$$U_f = (\frac{H(u)}{a_p})_f - (\frac{1}{a_p})_f (\nabla P_{rgh} + gz(\nabla \rho))_f \tag{2.15}$$

and the conservative mass flux on the cell faces is:

$$F_f = S_f((\rho \frac{H(u)}{a_p})_f - (\frac{1}{a_p})_f(\nabla P_{rgh} + gz(\nabla\rho))_f) \tag{2.16}$$

Substitute this in the continuity equation Eqn 2.9 to build:

$$\sum_{f=1}^{N}(\frac{1}{a_p})_f \rho_f S_f \cdot (\nabla P_{rgh} + gz(\nabla\rho))_f = \sum_{f=1}^{N} \rho_f S_f (\frac{H(u)}{a_p})_f \tag{2.17}$$

Algorithmus 2.1 Semi-implicit pressure-velocity coupling PISO

1. Explicit solve discretisized momentum equation, as in Eqn 2.12;
2. Explicit solve discretisized energy equation;
3. Implicit pressure correction:
3.1 Update cell value $\frac{H(u)}{a_p}$, the first term in RHS of Eqn 2.13;
3.2 Interpolation surface flux $S_f((\rho \frac{H(u)}{a_p})_f + (\frac{1}{a_p})_f g \cdot h(\nabla\rho)_f)$, in RHS of Eqn 2.15;
3.3 Reconstruct and solve the continuity equation, Eqn 2.16
3.4 Update the velocity

2.4 High-performance computing performance

Parallel computational performance will be discussed in this subsection. The hardware utilized for computation is 'Hazel Hen' located at the High-Performance Computer Center Stuttgart (HLRS, Stuttgart). Hazel Hen is a Cray XC40 system that consists of 7712 compute nodes. Each node has two Intel Haswell processors (E5-2680 v3, 12 cores) and 128GB memory, and the nodes are interconnected by a Cray Aries network with a Dragonfly topology. This amounts to a total of 185,088 cores and a theoretical peak performance of 7.4 PFlop/s.

The parallel efficiency is dependent of several factors including but not limited to the hardware architecture, MPI/OpenMP communication protocol,

domain decomposition and linear solver for the iterative equations. In the domain decomposition, the load balance of each computational core and the total communication faces should be considered. Fig. 2.4 shows the domain decomposition of a short section from the whole pipe. A three-dimensional decomposition is applied to reduce the communication surfaces, which is advantageous in performance against one-dimensional and two-dimensional method.

The parallel scalability of the current numerical solver has been tested on the Hazel Hen platform, as shown in Fig. 2.5. The speedup and efficiency are calculated with the reference performance of 140 cores. With the current decomposition method, the number of used cores is not guaranteed as a multiple of 24, which is the number of cores on a single computational node in Hazel Hen. Under the condition of the present mesh size (80 Mio. cells), the solver shows a linear even super linear scalability until 700 cores. A considerable speedup has been determined up to 1400 cores (80% efficiency) and 2800 cores (60% efficiency). At 2800 cores, 28570 cells are distributed on each computational core. In a daily job, it costs about 4 days on 1400 cores for running 10 flow through time in the pipe. In the foreseeable future, the mesh resolution will increase to 300 Mio. aiming at a higher Reynolds number and an improved resolving of Batchelor scale in the thermal field.

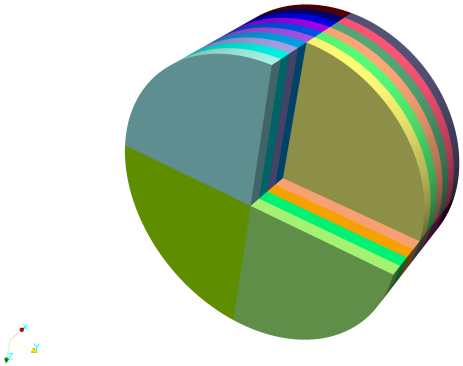

Figure 2.4: Domain decomposition of a short section from the whole pipe

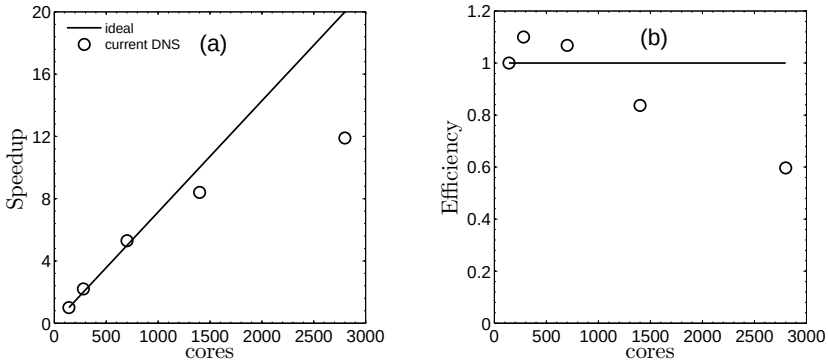

Figure 2.5: HPC performance of current DNS case (80 Mio. cells) on Hazel Hen, speedup (a) and efficiency (b)

Chapter 3

Validation of the numerical method

A validation is necessary for the newly implemented numerical solver. Heat transfer experiments of supercritical fluid are mostly evolved with high Reynolds number, which is beyond the capability of DNS. Therefore, a well-recognized experiment of heated air flow in pipe [SM95] is used for the validation. The flow relaminarization is expected in the DNS, which will also be discussed in detail in this chapter. The content in this chapter is also summarized in [CL16b].

Well-resolved Direct Numerical Simulation (DNS) is applied to investigate strongly heated air flow in a vertical pipe ($L = 30D$) at inlet Reynolds numbers of $\mathrm{Re}_0 = 4240$ and 6020. The DNS is based on the experimental cases of Shehata and McEligot [SM95] and shows excellent agreement with heat-transfer and flow statistical results. Flow relaminarization is observed in the strongly heated cases. We apply a new semi-local wall coordinate to replace the conventional one. With the semi-local wall coordinates, which considers the local property variation, both the velocity and temperature fields show

the process of relaminarization. This relaminarization is also indicated by the significant decrease of turbulence intensity and Reynolds shear stress. In the quasi-laminar flow, the viscous sublayer becomes thicker. Turbulence in this layer shows a growing anisotropic character. And turbulence in the pipe center becomes approximately isotropic. This two-layer character is clearly displayed by flow visualization.

3.1 Introduction

Strongly heated gas flow in a vertical pipe has much fundamental usage in engineering applications, such as the very-high-temperature reactor (VHTR) in the nuclear industry, which is designed with an outlet temperature of up to 1000°C. When the turbulent gas flow is intensively heated, the variable thermo-physical properties can lead to a flow retransition from turbulent to quasi-laminar, called 'relaminarization' in some literature [SM95]. Accordingly, heat transfer efficiency drops rapidly and it results in a sharp rise of pipe wall temperature. In earlier studies, Carr *et al*. [CCB73] reported experiments of heated air in pipe flow with measurements of velocity, temperature and turbulence data, where they observed a distortion of the flow structure at low Reynolds numbers (Re), and a depressed axial turbulence intensity. Another detailed report with well documented data was published by Shehata and McEligot [SM95], which is an extension of measurements by Perkins and McEligot [PM75]. In their experiments with heated air flow in a vertical pipe, they used three cases to represent 'turbulent', 'subturbulent' and 'laminarizing' flow with inlet Reynolds numbers of $Re_0 = 4240$ and 6020. In these forced-convection dominant cases, various flow statistics at different positions along the pipe are presented. A further analysis of the mean flow statistics can be found in [SM95] by the same authors. Jackson *et al*. [JMB89] reviewed these early studies as mixed convection in vertical tubes.

The moderate Reynolds numbers and detailed flow statistics of the experiments from Shehata and McEligot [SM95] enable validation and further investigations using numerical approaches including Direct Numerical Simulation (DNS). The DNS by Satake *et al*. [SKSM00] was conducted to reproduce these results. This numerical solver is based on the incompressible Navier-Stokes equations with a body-force term to account for the buoyancy effect. They applied the measured wall temperature distribution as the thermal boundary condition and focused on the statistics of the turbulence field. The DNS study from You *et al*. [YYC03] aimed at examining the buoyancy effects of mixed convection heat transfer through comparing upward

and downward flow cases. They discussed the 'external'- and 'structural'-effects of the buoyancy. A more recent work was accomplished by Bae *et al.* [BYCM06], in which the low-Mach-number form of the Naiver-Stokes equations was adopted to include temperature-dependent properties and exclude compressibility effects. A dissimilarity of velocity and temperature fields was found in their study and it was concluded to be the result of density variation. Besides those studies, Xu *et al.* [XLP+04] conducted large eddy simulation (LES) using Cartesian-based, compressible filtered Navier-Stokes equations. Their results showed that strong heat flux resulted in remarkable reductions of turbulent intensities and shear stresses. Mikielewicz *et al.* [MSJM02] assessed the performance of eleven turbulence models using the same results from Shehata and McEligot [SM95]. Mikielewicz *et al.* [MSJM02] showed that the Launder-Sharma turbulence model performed best in predicting streamwise wall temperature profiles and the agreement with measured velocity and temperature is promising.

In these studies above, it was concluded that the flow relaminarization occurred when a strong wall heat flux was applied. But the mean velocity profile in wall units did not show a clear tendency to be laminar as the temperature field did [SM98,BYCM06]. This observed dissimilarity between velocity and temperature profiles still needs a proper explanation. Further observations of the quasi-laminar flow field will also be valuable. In the present study, we attempt to develop a well-resolved DNS treating the experiments from Shehata and McEligot [SM95]. The current DNS intends to match the experimental measurement closely. The velocity and temperature fields will be displayed in new semi-local wall coordinates. This new representation is intended to eliminate the dissimilarity between both fields and to offer us a new vision of flow relaminarization. The turbulence statistics offer us an insight at the process of relaminarization. Finally, the character of this quasi-laminar flow will be discussed.

3.2 Computational Details

3.2.1 Governing Equations

In the present DNS study, air flow in a pipe is intensively heated through the wall, which leads to a variation of fluid properties. For considering the significant property variation in low-Mach number turbulent flow, Navier-Stokes equations are constructed in the low-Mach-number form as introduced in Eqns. 2.1-2.3, in which the compressibility effect is excluded. The perfect gas approximation and power law representations suggested by the authors in the experiment [SM95,BYCM06] are employed for air properties, as shown in Eqn. 3.1. The reference properties for dynamic viscosity μ_{ref} (Pa s), thermal conductivity κ_{ref} (W/m K) and specific heat capacity $C_{p,ref}$ (J/kg K) are based on $T_{ref} = 296.7$ K and $P_{ref} = 0.1$ MPa. The validity of these modelings are tested and proved with the data base of REFPROF 9.1 by NIST at $P_0 = 0.927$ MPa. In the temperature range of 280 K to 900 K, density shows a maximum difference of 0.06%, while maximum mismatches of 4.5%, 0.7% and 1.8% are found in the values of μ, C_p and κ respectively. The results are satisfying considering a maximum uncertainty of 1% with the REFPROF 9.1.

$$\frac{\rho}{\rho_{ref}} = \left(\frac{P_0}{P_{ref}}\right)\left(\frac{T_{ref}}{T}\right),\ \frac{\mu}{\mu_{ref}} = \left(\frac{T}{T_{ref}}\right)^{0.67},\ \frac{C_p}{C_{p,ref}} = \left(\frac{T}{T_{ref}}\right)^{0.095},\ \frac{\kappa}{\kappa_{ref}} = \left(\frac{T}{T_{ref}}\right)^{0.805} \tag{3.1}$$

3.2.2 Numerical Method

The governing equations (Eqns. 2.1-2.3) are discretized with the open source finite-volume code OpenFOAM V2.4 [Ope15]. An introduction of this numerical solver is given in chapter 2. The pipe geometry and boundary conditions are identical as in section 2.2.

The cylindrical pipe model is constructed with a structured hexahedral mesh. The resolution is equivalent to approximately $115 \times 120 \times 240$ (radial r,

circumferential θ and axial z direction) for the inflow domain and $115\times120\times1440$ for the heated domain, when converted from Cartesian to cylindrical coordinates. Compared with Bae *et al.* ($69\times129\times769$) and Satake *et al.* ($64\times128\times768$), nearly double amount of grid points are located in the radial and axial directions. The mesh is uniformly spaced in the axial direction and is refined near the wall in the radial direction with a stretching ratio of 10 (defined as the ratio of cell size at the pipe center and cell size at the wall). It corresponds to a dimensionless resolution of 0.17 (wall) $< \Delta y^+ <$ 1.7 (center), $(R\Delta\Theta)^+ \approx 10.3$ and $\Delta z^+ = 8.2$ in wall units, i.e., $y^+ = yU_{\tau,0}/\nu_0$, based on inlet Reynolds number $\mathrm{Re}_0 = 6020$. The corresponding dimensionless resolution at Re_0=4240 can be found in Table 3.1. It is worth mentioning that the bulk Reynolds number Re_b decreases in the downstream direction, so the local dimensionless mesh resolution becomes higher than at the inlet. The Prandtl number of air flow (Pr≈0.71) indicates a slightly bigger thermal scale ($\eta_\theta = \eta/\sqrt{1/\mathrm{Pr}}$) than the Kolmogorov scale (η). In the post-processing, a mesh coordinate transformation from Cartesian coordinates to cylindrical coordinates is necessary. The flow statistics are obtained through averaging in time and space (circumferential direction). For the initial transient, ten flow through times are needed and are followed by ten flow through times for statistical sampling.

3.2.3 Simulation Conditions

In the current study, three cases (Run618, Run635 and Run445) from the experiments of Shehata and McEligot [SM95] are approximated. A pure forced-convection case Run445F is also included, where the body force term in Eqn. 2.2 is suppressed. The corresponding boundary conditions are summarized in Table 3.1. Run618 and Run635 have an identical inlet Reynolds number of Re_0=6020, while the lower Re_0=4240 is used in Run445 and Run445F. Compared with the experiments, Re_0 has slight differences of 0.2%, 0.08% and 0% in Run618, Run635 and Run445, respectively. In the experiments, T_0 is slightly different (297.15 ± 1K) between the three cases. Here, the inlet temperature is simplified to identical $T_0 = 297.15$ K in all

Case	Re_0	$U_{z,0}$ (m/s)	q_w (kW/m^2)	Δy_1^+	$(\Delta y^+)_{max}$	$R\Delta\theta^+$	Δz^+
Run618	6020	3.73	2.21	0.17	1.7	10.3	8.2
Run635	6020	3.73	4.31	0.17	1.7	10.3	8.2
Run445	4240	2.63	3.98	0.14	1.4	7.8	6.3
Run445F	4240	2.63	3.98	0.14	1.4	7.8	6.3

Table 3.1: Simulation conditions, identical inlet conditions $T_0 = 297.15$ K, $P_0 = 0.0927$ MPa, and the pipe diameter is $D = 0.0274$ m

cases. The inlet pressure $P_0 = 0.0927$ MPa in the current DNS is adjusted close to $P_0 = 0.09266$ in experiments in contrast to the simplifications of $P_0 = 0.09$ MPa in [SKSM00] or $P_0 = 0.1$ MPa in [BYCM06]. In experimental environment, wall heat flux is imposed by electrical power and varies in the axial direction [SM95]. The constant wall heat flux q_w used in the current DNS is calculated from $q_w = q^+ \rho_0 U_0 C_{p,0} T_0$ based on inlet value, where q^+ is 0.0018, 0.0035 and 0.0045 from the last two digits in the names. It is found that slightly increasing the wall heat flux modifies the effects of varying wall heat flux and achieves a better match with the wall temperature profiles, especially in cases Run445 and Run445F. Therefore, an extra 4.4% for the heat flux (q^+=0.0047 instead of 0.0045) is employed in both cases. A similar treatment can be found in [BYCM06].

3.2.4 Inflow Turbulence

In the experiments, approximately fully developed turbulent flow at a uniform temperature [SM98] enters the heated pipe section, as shown in Fig. 3.1(a). Since detailed turbulence intensity data are not available from the experiments, DNS predictions from Eggels *et al.* [EUW+94] at Re=5300 are used (Fig. 3.1(b)). The results for Run618 and Run635 are presented here because their Reynolds number (Re_0=6020) is close to Eggels *et al.*. The mean streamwise velocity $U_z^+ = U_z/U_\tau$, $y^+ = yU_\tau/\nu$ where $U_\tau = \sqrt{\tau_w/\rho}$ is plotted in Fig. 3.1(a). And the turbulence intensities for the three directions $U_{rms}^+ = U_{rms}/U_\tau$ are shown in Fig. 3.1(b). The results are in excellent

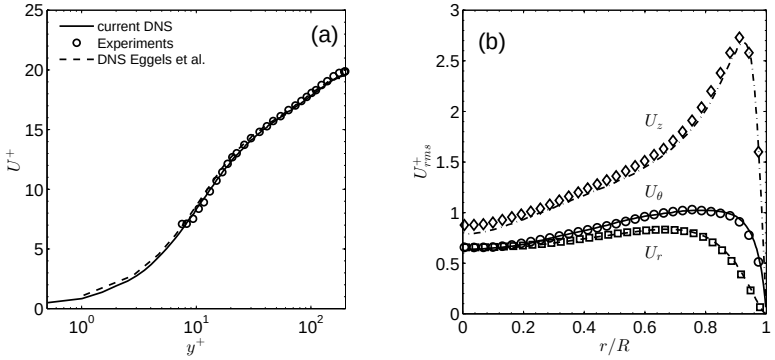

Figure 3.1: Inflow turbulence validation, (a): mean streamwise velocity, current DNS at $\mathrm{Re}_0 = 6020$, experimental data at $\mathrm{Re}_0 = 6020$ [SM95] and DNS data from Eggels *et al.* [EUW+94] at Re=5300, (b): dimensionless velocity fluctuation U^+_{rms} in r, θ and z direction, lines: current DNS; symbols: DNS data from Eggels *et al.*

agreement with the reference data.

3.3 Results and Discussion

3.3.1 Bulk Properties

Fig. 3.2(a) summarizes the predictions of wall temperature T_w in all four cases. The heat transfer results produced by the current DNS agree generally well with the experimental data, where an experimental uncertainty of $1-2\%$ in temperature profiles must be considered. As shown later in Fig. 3.3(b), the highest buoyancy parameter $\mathrm{Gr}/\mathrm{Re}^2_\mathrm{b}$ is found in case Run445 and it shows its peak value $\mathrm{Gr}/{\mathrm{Re}_\mathrm{b}}^2 = 0.55$ near the inlet as shown . But between case Run445 and its forced-convection reference Run645F, no significant difference in wall temperature profile $T_w\{z\}$ is observed. It means that the buoyancy effects on heat transfer behavior are relatively weak in this case. A tendency of underestimation of T_w is observed in cases Run635 and Run445,

as in the DNS predictions of Bae *et al.* [BYCM06]. Bae *et al.* explained these differences as consequences of upstream thermal conduction in the pipe forming the nominally unheated entry region in the experiment. In Fig. 3.2(b), validations of Nusselt number predictions Nu=hD/κ_b are given, where h is the convective heat transfer coefficient $h = q_w/(T_w - T_b)$ and κ_b is thermal conductivity evaluated with bulk temperature T_b. Nu shows a decreasing tendency in downstream direction of all cases, typically for thermal entries. The lowest Nusselt number is found in Run445/Run445F. The temperature-dependent properties of air lead to a decrease of bulk Reynolds number $\mathrm{Re_b}$ in the streamwise direction, as shown in Fig. 3.2(c). Compared with Run618, a larger decrease is observed in case Run635 due to higher wall heat flux q_w. Slight differences of $\mathrm{Re_b}$ from the experiments are observed and the difference generally increases in the streamwise direction. At $z = 25D$, Run618, Run635 and Run445 show differences of 0.4%, 2.8%, 2.1%, respectively, with $\mathrm{Re_b}$ in the experiment. The increasing discrepancies of Run635 and Run445 in the downstream direction suggest that the wall heat fluxes in the experiments increase slightly in the downstream direction rather than staying constant. In the experiment of Run635, the wall heat flux at $z = 25D$ is about 6% higher than that at $z = 3D$ [SM95]. Similarly, T_w in Fig. 3.2(a) also shows growing discrepancies in downstream direction for Run635 and Run445. A better agreement can be expected by imposing the actual varying wall heat flux instead of the constant wall heat flux.

The predicted skin friction coefficient distributions $C_f = 2\tau_w/(\rho_b U_b^2)$ based on wall shear stress τ_w and local bulk parameters ρ_b and U_b are summarized in Fig. 3.2(d). The Blasius correlation for turbulent flow $C_f = 0.079Re^{-0.25}$ is marked with symbols. At the inlet, the predicted $C_{f,0} = 0.00900$ from Run618 and Run635 matches the Blasius estimated $C_f = 0.079Re^{-0.25} = 0.00897$ with 0.3% difference. In Run445, the present prediction $C_{f,0} = 0.0100$ in DNS shows a slight difference from the Blasius correlation $C_f = 0.079Re^{-0.25} = 0.0098$ of 2%. In Run618 and Run635, C_f tends to increase after the inlet and then decreases slightly. In Run445, the decreasing tendency is similar but less obvious than Run635. Unlike the agreement for T_w, C_f is generally lower in Run445F than Run445. This increase and decrease of C_f is comparable

the so called quasi-laminarization process in accelerated turbulent boundary layers (TBL) reported by Araya *et al*. [ACH16].

In Fig. 3.3(a), the acceleration parameter $K_v = \frac{\nu_b}{U_b^2}\frac{dU_b}{dz}$ is plotted. K_v decreases slightly in the streamwise direction in Run445 and Run445F , and it stays almost constant in Run618 and Run635. The highest $K_v \approx 4 \times 10^{-6}$ is found in Run445 and Run445F due to the high heat flux and flow mass flux, while that of Run618 is the lowest with a nearly constant $K_v \approx 1.2 \times 10^{-6}$. In Run635, K_v shows a value of $K_v \approx 2.2 \times 10^{-6}$. McEligot and Jackson recommended an approximate critical value of K_v in [MJ04]. The critical K_v suggested by different authors is in the range of 2-3$\times 10^{-6}$. The critical K_v observed in the current DNS, where flow relaminarization occurs is $K_v \approx 2.2 \times 10^{-6}$ in Run635. This observation is consistent with the existing literature. Accordingly, flow relaminarization by thermal acceleration should be expected in the strongly heated cases.

The parameter Gr/Re^2, where $Gr = gD^4 q_w/(\nu_b^2 \kappa_b T_b)$ is the Grashof number, indicates the effect of buoyancy; It is showed in Fig. 3.3(b). The maximum value of $Gr/Re^2 = 0.55$ is observed at the inlet of Run445. This magnitude suggests that buoyancy effects may be noticeable. The Local bulk Stanton number $St_b = h/(\rho_b U_b C_{p,b})$ is plotted as a function of local bulk Reynolds number Re_b (and therefore of axial location) in Fig. 3.3(c). After the inlet region, St_b appears to diverge from turbulent correlation and approach the laminar correlation in Run635 and Run445, even though Re_b is above 3000.

3.3.2 Mean Flow Statistics

In the turbulent flow statistics below, we define the mean quantities with Reynolds- and Favre averaging, where $\bar{\phi}$ is the Reynolds average of any quantity and $\widetilde{\phi} = \frac{\overline{\rho\phi}}{\bar{\rho}}$ is the mass-weighted (Favre) average. The corresponding fluctuations are denoted with $\phi' = \phi - \bar{\phi}$ and $\phi'' = \phi - \widetilde{\phi}$, respectively. The normalized Reynolds-averaged velocity and temperature profiles of Run618, Run635 and Run445 are validated by comparison to the measurements at several positions in the downstream direction, as shown in Fig. 3.4. The experimental results are marked with symbols and the numerical profiles

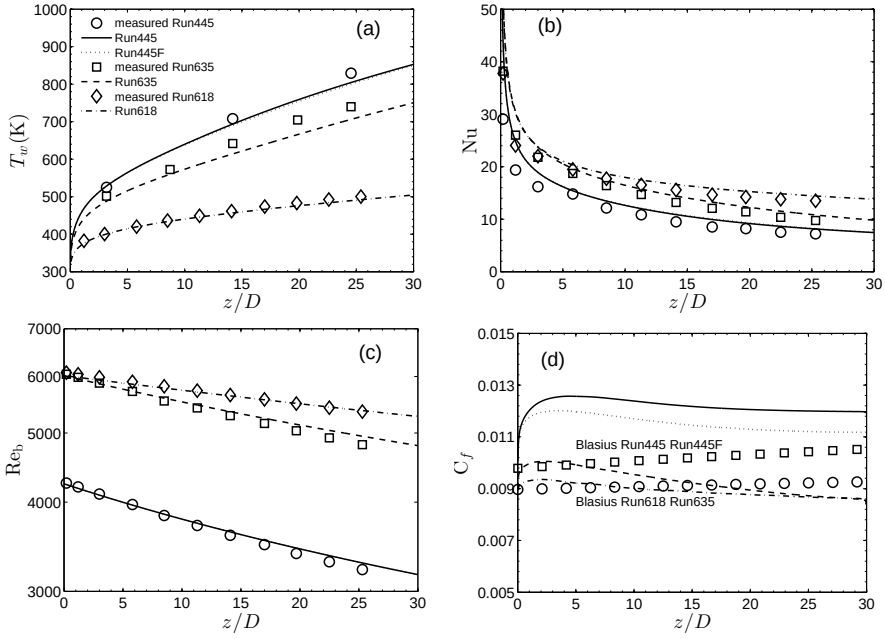

Figure 3.2: Streamwise development of integral quantities from present DNS and experiments of Shehata and McEligot [SM95], (a): wall temperature, (b): Nusselt number Nu, (c): bulk Reynolds number Re_b and (d): friction factor C_f

are plotted in lines. Both the velocity and temperature fields agree with the measured data. This agreement indicates that the current numerical results are reasonably reliable for further study.

Shehata and McEligot [SM98] plotted the velocity and temperature profiles from their experimental results in conventional wall units. As in Eqns. 3.2 and 3.3 below, these wall coordinates are defined in terms of fluid properties evaluated at the local wall temperature T_w. The present results for Run445 are plotted using this definition in Fig. 3.5(a) and Fig. 3.5(b). As a reference, the laminar profile ($U^+_{Lam} = y^+(1-1/2U)$) together with a fully developed turbulent profile ($U^+ = y^+$ and $U^+ = 2.5\ln y^+ + 5.5$)

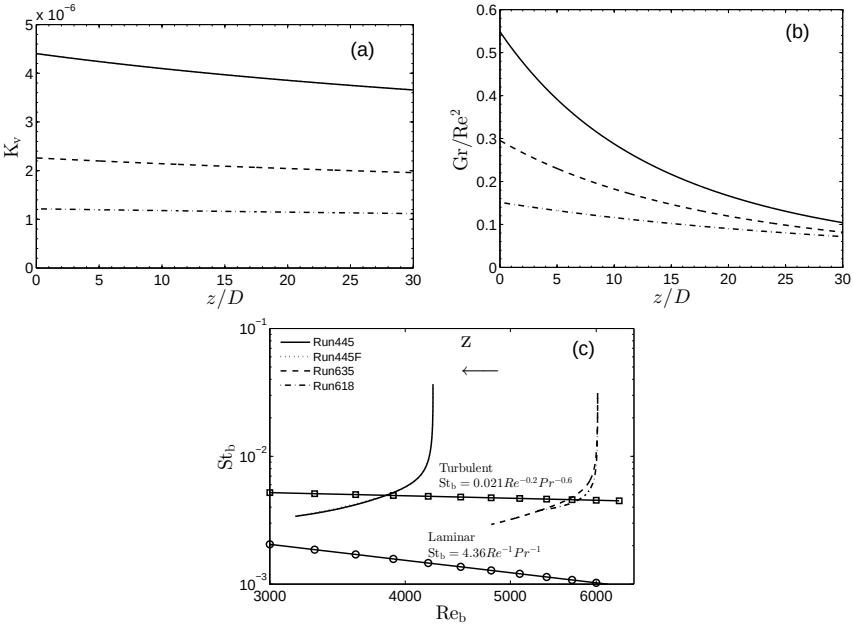

Figure 3.3: Streamwise development of integral quantities from present DNS, (a): K_v, (b): Gr/Re^2 and (c): St_b

are given and are marked with symbols in Fig. 3.5(a). Similarly, $\theta^+_{Lam} = \mathrm{Pr}y^+(1+0.5y-y^2+0.25y^3)$ is considered as a reference θ^+ profile for the laminar field, and $\theta = \mathrm{Pr}y^+$ ($y^+ < 11$) with $\theta^+ = 2.78\ln(y^+)+2.09$ ($y^+ > 11$) is used as a reference for the turbulent field. In the usual laminar sublayer ($y^+ < 11$), U^+ at all positions ($z = 3D, 14D$ and $25D$) follows $U^+ = y^+$ generally and θ^+ follows $\theta^+ = \mathrm{Pr}y^+$. Beyond the laminar sublayer, U^+ follows neither the turbulent nor the laminar profile, counter to the expectation of flow relaminarization in this case. On the other hand, θ^+ approaches the laminar profile $\theta^+_{Lam} = \mathrm{Pr}y^+(1+0.5y-y^2+0.25y^3)$ at $z = 14D$ and $z = 25D$. Similar results were reported by Shehata and McEligot [SM98].

$$U^+ = U/U_\tau,\ y^+ = yU_\tau/\nu_w,\ U_\tau = \sqrt{\tau_w/\rho_w} \tag{3.2}$$

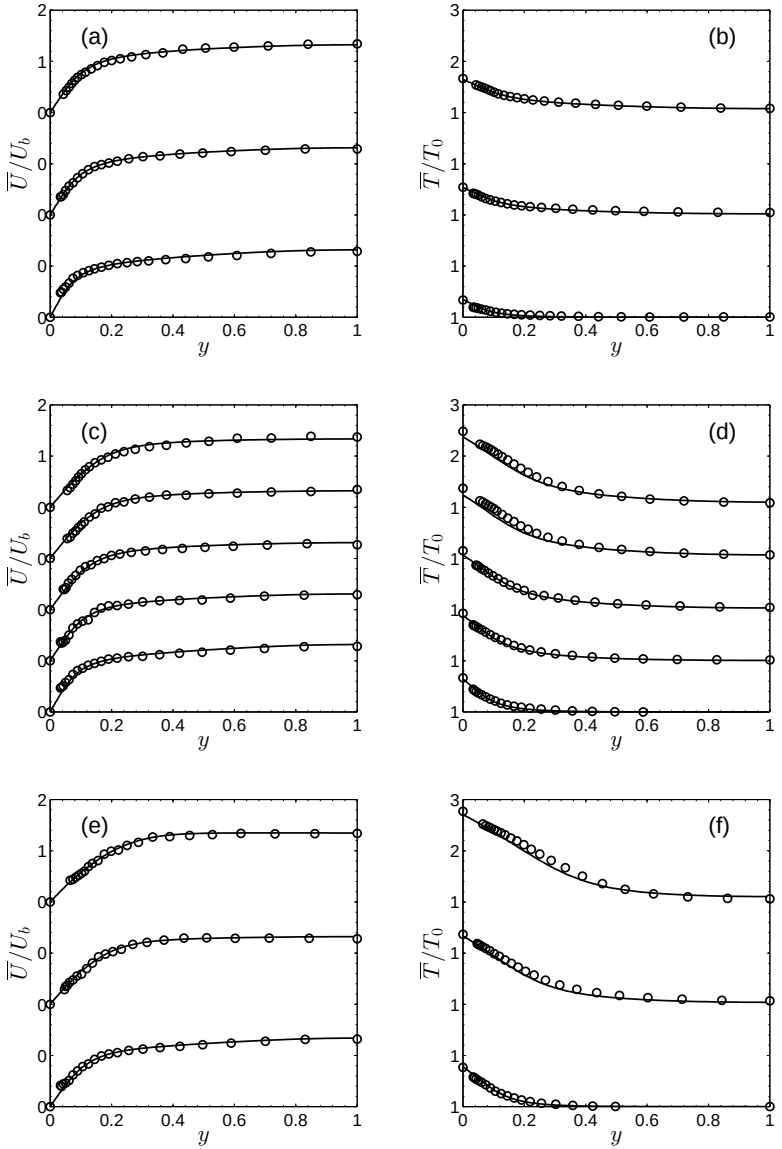

Figure 3.4: Mean velocity and temperature profiles of Run 618 (a and b), Run635 (c and d), Run445 (e and f), normalized by local U_b and inlet T_0, from bottom to top are $z = 3$, 14 and $25D$ (Run618 and Run445) and, $z = 3$, 9, 14, 20 and $25D$ (Run635)

$$\theta^+ = (T_w - T)/T_\tau,\ T_\tau = q_w/(\rho_w C_{p,w} U_\tau) \tag{3.3}$$

In their DNS, Bae *et al.* [BYCM06] tried to use Van Driest transformed velocity $U_{VD} = \sqrt{\rho/\rho_w}U$, $U^+_{VD} = U_{VD}/U_\tau$ to replace the first definition in Eqn. 3.2, while U_τ and y^+ remain the same. The temperature field θ^+ is the same as the definition in Eqn. 3.3. The Van Driest density-weighted transformation is known to collapse velocity profiles of compressible boundary layers to incompressible law of the wall [HCB95]. But a dissimilarity of the mean velocity U^+_{VD} and temperature θ^+ profiles is still observed by Bae *et al.* [BYCM06], specially in Run445. They suggested that the difficulty is connected with the large variation of density due to heating.

The comparisons above lead to the question: is it appropriate to use identical wall values ρ_w and ν_w over the entire wall-normal direction as in Eqns. 3.2 and 3.3, or one should employ local variables. For compressible channel flow, Huang, Coleman and Bradshaw [HCB95] introduced a variable y^* (defined as $y^* = yU_\tau/\nu$, which based on τ_w, local density ρ and local viscosity ν) instead of y^+. The complete definitions are as in Eqns. 3.4 and 3.5 below. In these definitions, the local ρ, ν, C_p are applied instead of the wall value ρ_w, ν_w, $C_{p,w}$. This semi-local wall coordinate was found to be more advantageous than use of either wall properties or averaged properties from wall to bulk temperatures [HCB95]. Lee *et al.* [LSHZ13] used this modified wall coordinate in their DNS of turbulent boundary layers with temperature-dependent viscosities and showed good agreement with the law of the wall. Patel *et al.* [PPBP15] also used this method in their DNS with variable density and viscosity flow. With this new scale, the flow shows quasi-similarity with constant property turbulent flows at the same $Re^*_\tau = \sqrt{(\rho/\rho_w)}/(\mu/\mu_w)Re_{\tau,w}$ (i.e. a modified turbulent Reynolds number with this semi-local wall coordinate). Therefore, in the current work, we investigate the use of this definition of semi-local wall coordinate

as followings:

$$U_{VD}^{+} = U_{VD}/U_{\tau},\ y^{*} = yU_{\tau}/\nu,\ U_{\tau} = \sqrt{\tau_{w}/\rho} \tag{3.4}$$

$$\theta^{*} = (T_{w} - T)/T_{\tau},\ T_{\tau} = q_{w}/(\rho C_{p} U_{\tau}) \tag{3.5}$$

Here, the local ρ, ν, C_p are dependent on local T (Reynolds averaged temperature in y direction) in the wall-normal direction and τ_w is known as a wall value. With this semi-local wall coordinate, the velocity U_{VD}^{+} and temperature θ^{*} profiles of Run445 are plotted in Fig. 3.5(c) and Fig. 3.5(d). Compared with Fig. 3.5(a) which employed the conventional wall unit definition, an obvious tendency of flow relaminarization is observed in the velocity field U^{*}. Both velocity and temperature profile show a shift from turbulent to laminar profiles in the downstream direction (Fig. 3.5(c) and Fig. 3.5(d)). This behavior is significantly different than in Fig. 3.5(a) and Fig. 3.5(b). Also, a thicker laminar sublayer is observed in terms of decreasing log regions in both fields progressing downstream. In Fig. 3.6, the same semi-local wall coordinate is applied in case Run618 and Run635 as shown . Both U_{VD}^{+} and θ^{*} show stronger relaminarization tendency in Run635 than Run618. This result is consistent with the previous description of the two cases as 'turbulent' and 'subturbulent' by Shehata and McEligot [SM95] based on Nusselt number behavior in the downstream direction.

The validity of constant $\mathrm{Re_b}$ or $\mathrm{Re_\tau} = U_{\tau}R/\nu_{b}$ in wall normal direction is affected by flow property variation. With the semi-local wall coordinate in Eqn. 3.4 and 3.5, a new Re_{τ}^{*} is defined as in Eqn. 3.6, representing a local turbulent Reynolds number. With constant properties at inlet, $\mathrm{Re}_{\tau,0}^{*}$ is the same as $\mathrm{Re}_{\tau,0}$.

$$\mathrm{Re}_{\tau}^{*} = \frac{U_{\tau}R}{\nu} = \frac{\sqrt{(\rho/\rho_{w})}}{(\mu/\mu_{w})}\mathrm{Re}_{\tau,\mathrm{w}} \tag{3.6}$$

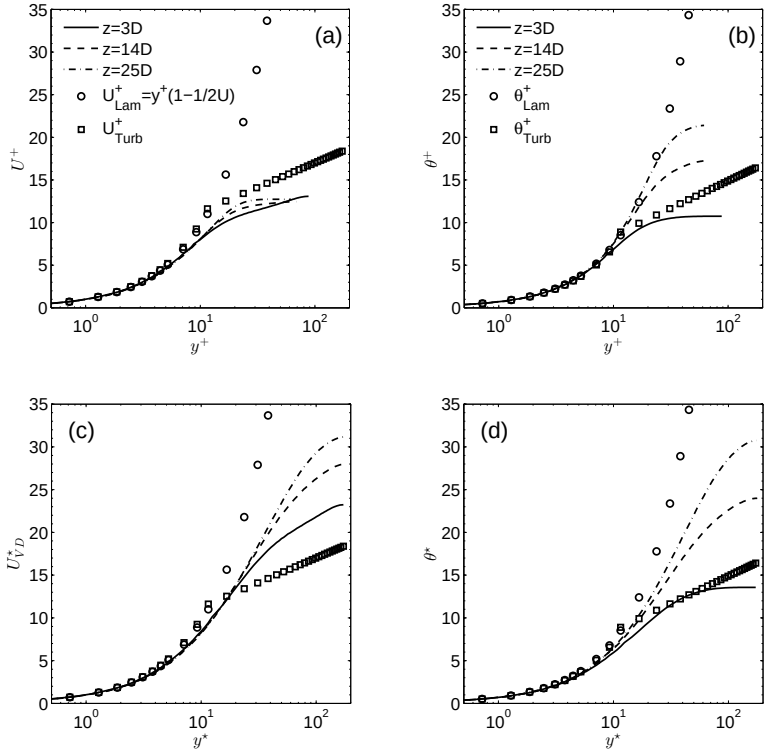

Figure 3.5: Velocity and temperature profiles for case Run445 with two different wall unit definitions, (a): U^+ as a function of y^+; (b): θ^+ as a function of y^+, (c): U^*_{VD} as a function of y^*, (d): θ^* as a function of y^*

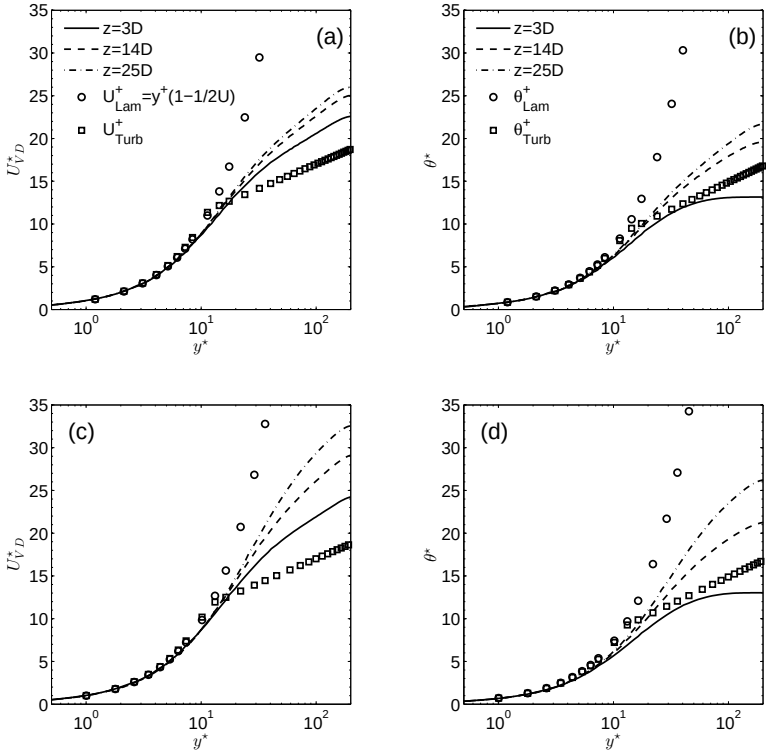

Figure 3.6: Velocity U^*_{VD} and temperature profiles θ^* in semi-local wall unit y^* with $\theta^+_{Lam} = \mathrm{Pr}y^+(1 + 0.5y - y^2 + 0.25y^3)$, case Run618 (a) and (b) and Run635 (c) and (d)

The distributions of Re^*_τ in Run618, Run635, Run445 and Run445F in the wall normal direction are shown in Fig. 3.7. A varying Re^*_τ is observed in all situations. Near the wall, Re^*_τ is lower than $\mathrm{Re}_{\tau,0}$. In Run635, Run445 and Run445F, Re^*_τ is greater than $\mathrm{Re}_{\tau,0}$ at the pipe center. These two observations indicate that near-wall layer is involved in the flow relaminarization but the outer layer becomes actually more turbulent (i.e. corresponds to a higher Re_τ flow). It may be concluded that this apparent turbulence mod-

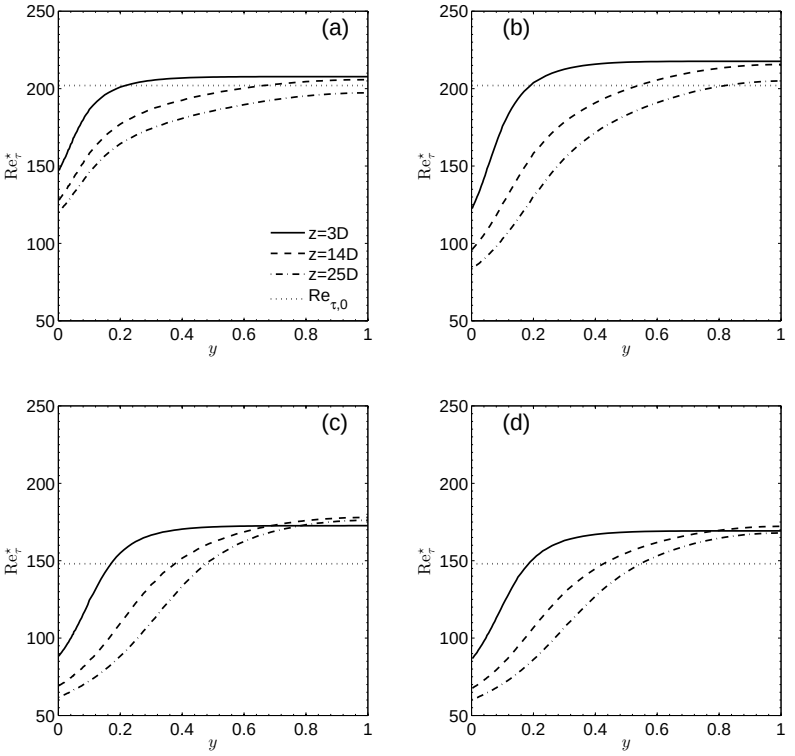

Figure 3.7: Distribution of turbulent Reynolds number in semi-local wall units Re^*_τ together with $Re_{\tau,0}$, (a): Run618 (b) Run635, (c) Run445 and (d) Run445F

ification in the near-wall layer has a significant significant relation to the flow relaminarization. The development of Re^*_τ is comparable in Run445 and Run445F.

3.3.3 Turbulence Statistics

Fig. 3.8 summarizes the turbulent kinetic energy (TKE) per unit volume $1/2\overline{\rho U_i' U_i'}$ normalized by $\tau_{w,0}$. In Run618 (Fig. 3.8(a)), a slight reduction

of TKE is observed in the downstream direction. This tendency is more pronounced in the other three cases, indicating a process of flow relaminarization. The process of flow relaminarization shows some qualitative similarity in these cases. The peak value near the wall is reduced at $z = 3D$, and it is followed by a decrease in the pipe center at $z = 14D$ and $25D$. The lowest TKE at $z = 25D$ is found in Run445, suggesting the strongest flow relaminarization. Run445F shows slightly higher turbulent kinetic energy than Run445 at all three positions with the same mass flux and wall heat flux.

The Reynolds shear stress $\overline{\rho U_r'' U_z''}$ normalized by $\tau_{w,0}$ is shown in Fig. 3.9. Significant decreases are observed in Run635, Run445 and Run445F, representing flow relaminarization in the form of reduced turbulent momentum transport. In Run635, the peak value at $z = 25D$ decreases to about 1/3 of the original value at $z = 0D$. In Run445, it is only about 1/10 of the original value at the same position. Besides, $\overline{\rho U_r'' U_z''}$ shows a sign change in the range of $0.6 < y < 1$ at $z = 25D$. Compared with case Run445, Run445F shows higher values at $z = 14D$ and $z = 25D$. In Run445F, the sign change of Reynolds shear stress is absent.

In Fig. 3.10, the three anisotropies $-b_{rr}$, $-b_{\theta\theta}$ and b_{zz} of the Reynolds stress tensor in laminarizing Run445 are analyzed. The Reynolds stress anisotropy tensor is defined as in Eqn. 3.7, where $\overline{\rho U_i'' U_j''}$ is the Reynolds stress tensor, TKE is turbulent kinetic energy $1/2\overline{\rho U_i'' U_i''}$ and δ_{ij} is the Kronecker delta.

$$b_{ij} = \frac{\overline{\rho U_i'' U_j''}}{2TKE} - \frac{1}{3}\delta_{ij} \tag{3.7}$$

The turbulent flow shows a significant two-layer character. Near the wall ($y_0^+ < 40 - 50$), both axial anisotropy b_{zz} and circumferential anisotropy $-b_{\theta\theta}$ increase in the flow direction and both of them have a flat profile at $z = 14D$ and $25D$. The wall normal component $-b_{rr}$ is relatively unaffected under $y_0^+ < 10$. The strong anisotropic turbulence near the wall is extended

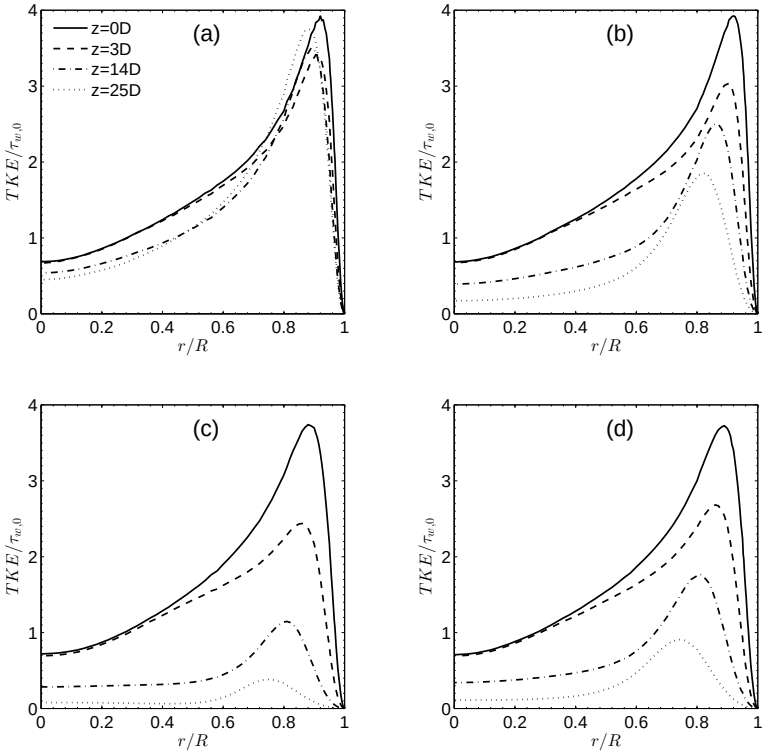

Figure 3.8: Development of turbulent kinetic energy (TKE) $1/2\overline{\rho U_i' U_i'}$ per unit volume normalized by $\tau_{w,0}$, (a): Run 618, (b): Run635, (c): Run445 and (d) Run445F

from about $y_0^+ = 10$ to about $y_0^+ = 50$. Another significant change is the extension of the anisotrop-turbulence layer. This change is consistent with those found in the velocity and temperature profiles in Fig. 3.5. Beyond the wall layer ($y_0^+ > 50$), all three components decrease sharply and nearly intersect with each other in the pipe center line; This near equality indicates a nearly isotropic turbulence in the pipe center.

Fig. 3.11 shows the rates of production of turbulent kinetic energy from

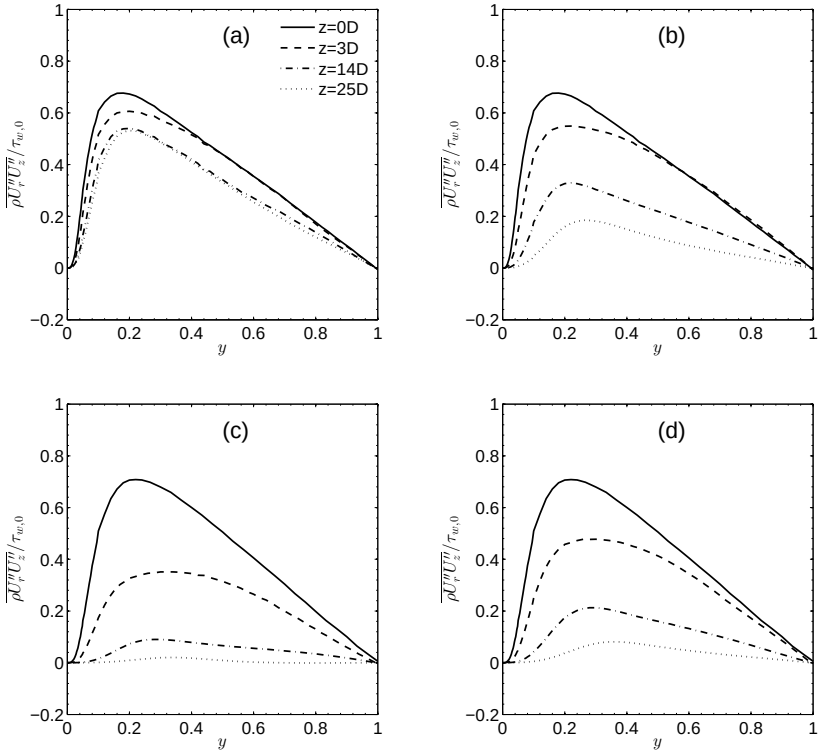

Figure 3.9: Evolution of Reynolds shear stress $\overline{\rho U_r'' U_z''}$ normalized by $\tau_{w,0}$, (a): Run618, (b): Run635, (c): Run445 and (d): Run445F

shear (Pk) $-\overline{\rho U_i'' U_j''}(\partial \widetilde{U}_i/\partial x_j)$ and the buoyancy production (BP) $g\overline{\rho' U_z'}$ in the left and right columns, respectively. Pk and BP play essential roles in the transport equation of TKE as below.

$$\frac{D(TKE)}{Dt} = -\overline{\rho U_i'' U_j''}(\partial \widetilde{U}_i/\partial x_j) + \cdots \mp g\overline{\rho' U'} \tag{3.8}$$

In Run635 and Run445, Pk shows rapid decreases in streamwise direction.

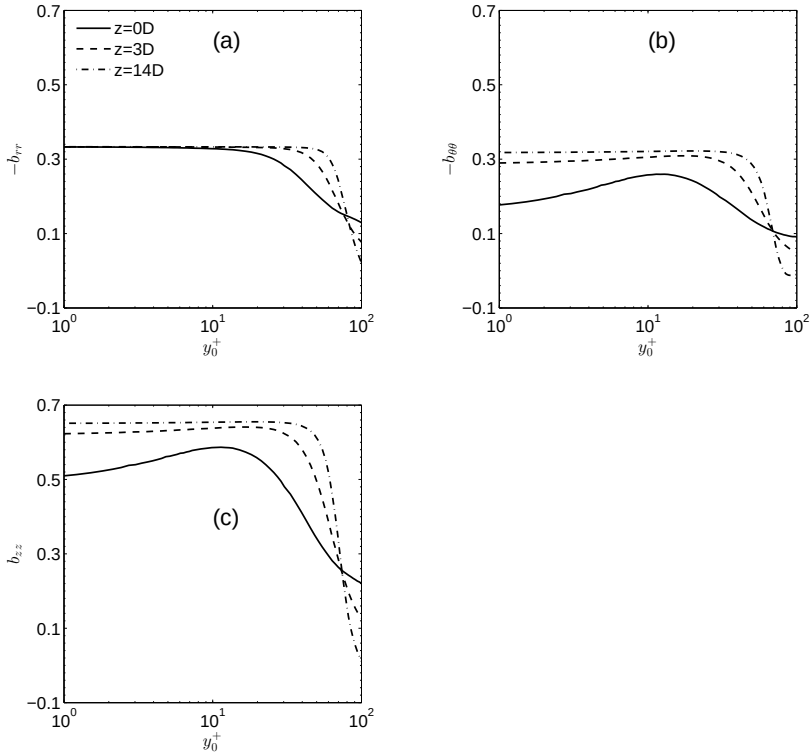

Figure 3.10: Distributions of anisotropies $-b_{rr}$, $-b_{\theta\theta}$, and b_{zz} of Reynolds stress tensor as a function of y_0^+ in Run445

These decreases explain the explanation of low level of turbulent kinetic energy in Fig. 3.7. Compared to shear production, the scale of buoyancy production is small, with the largest ratio BP/Pk observed in Run445. At $z = 25D$ of Run445, both Pk and BP are significantly reduced in contrast to Run618 and Run635.

Fig. 3.12 summarizes normalized axial and wall-normal turbulent heat flux $\overline{\rho U_z'' h''}$ and $\overline{\rho U_r'' h''}$ in the left and right columns, respectively. Typically, the magnitude of $\overline{\rho U_z'' h''}$ is much larger than that of $\overline{\rho U_r'' h''}$. In Run618,

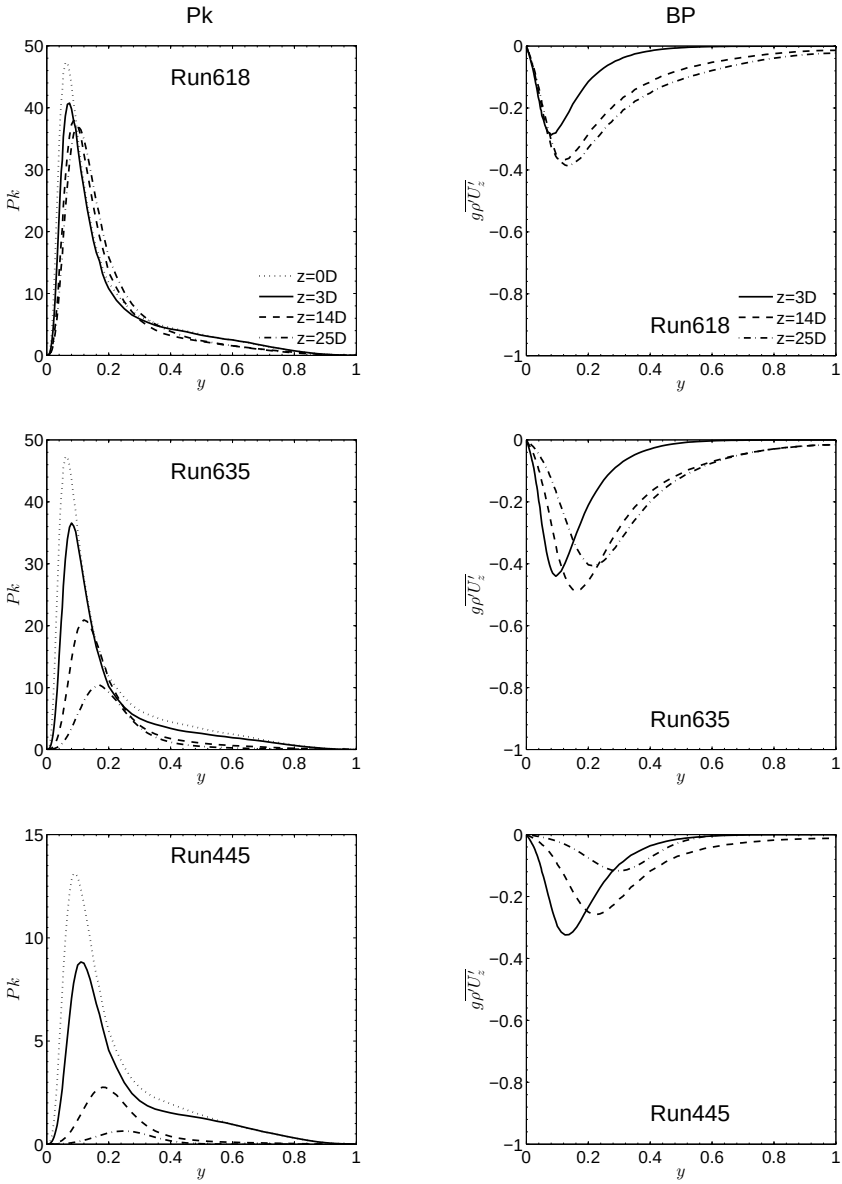

Figure 3.11: Production of turbulent kinetic energy $-\overline{\rho U_i'' U_j''}(\partial \widetilde{U}_i/\partial x_j)$ (kg/m s^3) and buoyancy production $g\overline{\rho' U_z'}$ (kg/m s^3) of case Run618 (a and b), Run635 (c and d) and Run445 (e and f)

both $\overline{\rho U_z'' h''}$ and $\overline{\rho U_r'' h''}$ increase monotonically in the flow direction. In Run635, this rising tendency weakens at $z = 14D$ and then the peak flux decreases at $z = 25D$. In Run445, both components decrease strongly after $z = 14D$ and the peak value shifts towards the pipe center line.

Fig. 3.13 describes the instantaneous velocity fluctuations in the axial direction $U_z''/U_{z,0}$ (a and b) for laminarizing Run445. Two sections of pipe, $z = 0-5D$ and $z = 25-30D$, are selected to show the thermal entry and apparent quasi-laminar flow downstream, respectively. In the grayscale, dark-grey areas indicate regions of low-speed streaks, light-grey areas indicate the location of high-speed streaks. The velocity fluctuations in the quasi-laminar section ($z = 25-30D$) are much smaller in magnitude than at $z = 0-5D$. Therefore, the greyscale is narrowed for an appropriate visualization of velocity structures. In the section $z = 25-30D$ (Fig. 3.13(b)), the intensities of energetic large scale streaks near the wall are evidently weakened but their scales are extended to form very long streaks at the same time. These very long streaks separate the inner layer and outer layer of the flow. These streaks in the near wall area demonstrate the strong anisotropy in Fig. 3.10. Also, the long streaks become clearly thicker in the quasi-laminar flow.

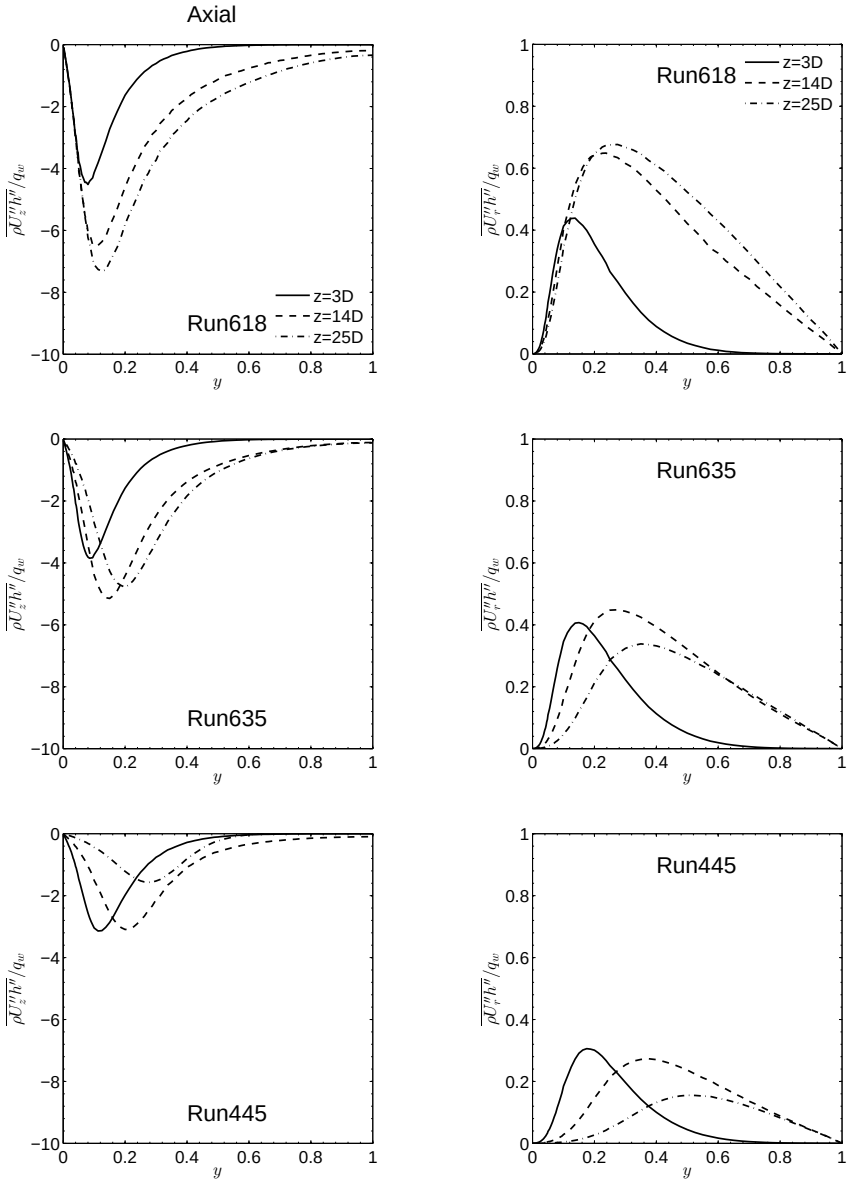

Figure 3.12: Turbulent heat fluxes $\overline{\rho U_z'' h''}$ and $\overline{\rho U_r'' h''}$ of Run618, Run635 and Run445, normalized by q_w

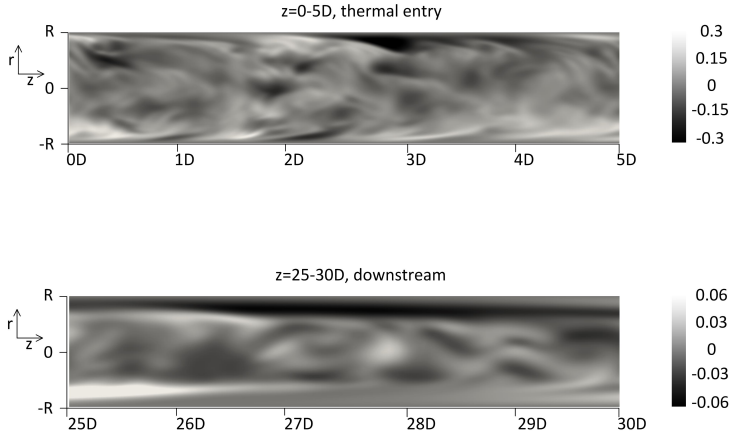

Figure 3.13: Examples of instantaneous fluid velocity fluctuations $U_z''/U_{z,0}$ of Run445, upper for thermal entry, lower for quasi-laminar flow downstream.

3.4 Summary

In the present study, well-resolved DNS is developed to investigate strongly heated air flow through a pipe ($L = 30D$). Compared with former DNS work, significantly more grid points are employed in the radial and axial directions to capture the detailed flow in both directions. The conditions are chosen to represent the experiment by Shehata and McEligot [SM95] closely, differing slightly from other DNS studies. Results from the present DNS are in close agreement with measured data from the experiments. A slight discrepancy is the result of imposing a constant wall heat flux instead of the varying wall heat flux of the experiment. We have discussed various flow and turbulence statistics. The observations may be summarized as follows:

1. The turbulent pipe flow is relaminarized in the downstream direction when a strong wall heat flux is applied, as in Run445. The apparent laminarization is confirmed by decreased Nusselt number Nu, laminarized velocity (U_{VD}^{+})/temperature profiles (θ^{*}) and decreased turbulent kinetic energy. The cases are considered as dominant forced-convection, so the flow relaminarization is not due to buoyancy effects. This aspect is demonstrated by comparing various statistics between Run445 and Run445F.

2. Unlike conventional wall coordinates as used in previous studies, a new semi-local wall coordinate is used to treat the local property variations in the transformation. With this definition, the apparent flow relaminarization is observed in both velocity and temperature profiles in contrast to earlier studies. Similarities between the profiles can be seen, enabling us to observe the changes of both fields in the process of laminarization.

3. When the flow is relaminarized, the turbulence intensity is suppressed, consistent with reduced production rates of turbulent kinetic energy. Compared with this TKE production, the buoyancy production is significantly smaller. The quasi-laminar flow shows a two-layer character, which has not been shown before. Very long streaks are observed near the wall and they seem to separate the pipe flow into two layers. The near-wall layer becomes thicker and the turbulence in this layer shows increased anisotropy in the streamwise and circumferential directions. Outside the near-wall layer, the

flow turbulence tends towards isotropy.

Chapter 4

Heat Transfer of Supercritical CO_2 in a Vertical Pipe

In this chapter, supercritical CO_2 in a heated vertical pipe will be investigated using DNS. The content in this chapter is a further step of the published results [CL16a]. The Reynolds number at inlet is constant at $Re_0 = 5400$. At a constant wall heat flux, the wall temperature rises across the pseudo-critical temperature, where the thermo-physical properties undergo significant changes with temperature. Various flow conditions are considered within our systematic study. In order to investigate the buoyancy effect on the flow turbulence, a comparison of upward and downward flow is performed. The convective heat transfer is deteriorated and then recovered in upward flow. The average velocity and temperature profiles are found to deviate the law of the wall in both cases. In the turbulence statistics, the Reynolds shear stress in upward flow experiences a change from positive- to negative values through zero. The statistics show, that the production rate of

kinetic energy in the upward flow case decreases and the turbulent flow is relaminarized. On the other hand, buoyancy production plays an important role in the transport equation of turbulent kinetic energy.

4.1 Computational Details

4.1.1 Numerical Procedure

The cylindrical pipe is constructed with structured hexahedral mesh. The grid resolution is equivalent to approximately $168 \times 172 \times 400$ (radial r, circumferential θ near the wall and axial z direction) for the inflow domain and $168 \times 172 \times 2400$ for the heated domain, when converted from Cartesian to Cylindrical coordinates. The flow statistics are obtained through averaging in time and the homogeneous direction (θ). The grid mesh is uniform spaced in the axial direction, and refined near the wall in the radial direction with a stretching ratio of about 10. Dimensionless resolution in wall units is demonstrated in Table 4.1. And T_b is defined as following:

$$T_b = f(h_b),\ h_b = h_0 + \frac{Q}{G},\ Q = q_w \pi D z,\ G = \frac{1}{4}\rho_b U_b \pi D^2 \tag{4.1}$$

where h_b, Q, G, z are bulk enthalpy, total wall heat flux, bulk mass flux and downstream position, respectively. At the inlet, dimensionless resolution reads as 0.11 (wall) $< \Delta y^+ < 1.1$ (center), $(R\Delta\Theta)^+ \approx 6.5$, $\Delta z^+ = 4.6$ based on inlet Reynolds number $\mathrm{Re}_0 = 5400$. And dimensionless time step uses the definition of $\Delta t^+ = \Delta t / t^+$, where $t^+ = D/U_\tau$. Flow bulk temperature T_b will rise in downstream direction with the input of wall heat flux. Accordingly, bulk Reynolds number $\mathrm{Re_b} = 4\mathrm{G}/(\mu_\mathrm{b}\pi\mathrm{D})$ will increase.

The turbulence intensities U^+_{rms} at inlet are validated with DNS from Wu and Moin [WM08], presented in Fig. . The quantities agree very well with the reference DNS.

Table 4.1: Dimensionless grid resolution at inlet and outlet of the pipe

position	Case	$\mathrm{Re_b}$	$\mathrm{Re_\tau}$	Δy^+_{min}	Δy^+_{max}	$R\Delta\Theta^+$	Δz^+	Δt^+
inlet	all	5400	360	0.11	1.1	6.5	4.6	1.1×10^{-4}
outlet	H22U	8260	500	0.15	1.5	8.9	6.3	1.4×10^{-4}
outlet	rest	6640	424	0.13	1.3	7.6	5.3	1.2×10^{-4}

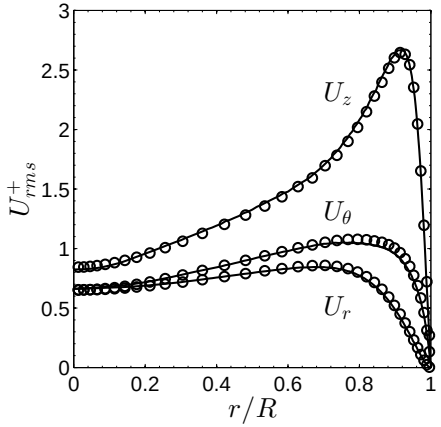

Figure 4.1: lines: Turbulence intensity U^+_{rms} at inlet; symbols: reference DNS from Wu and Moin [WM08]

4.1.2 Simulation Conditions

A summary of simulation conditions in the presented DNS cases is given in Table 4.2. The first digit in the case name represents the pipe diameter, the second indicates the wall heat flux, which is followed by the letter represents the flow direction, e.g. U for upward, D for downward and F for for forced convection. Pipe diameter is defined as $D = 1$ mm or 2 mm. Inlet Reynolds number is identical in all cases, which is $\mathrm{Re_0}$=5400. Inlet pressure $P_0 = 8$ MPa is above the critical pressure $P_c = 7.38$ MPa. Inlet temperature $T_0 = 301.15$ K is defined to be slightly lower than pseudo-critical temperature $T_{pc} = 307.85$ K. Different wall heat flux are given to exam the effect to the heat transfer.

Table 4.2: Simulation conditions, $P_0 = 8$ MPa, $\mathrm{Re}_0 = 5400$

Case	Type	Direction	D (mm)	T_0 (K)	G_0 (kg/m^2 s)	q_w (W/m^2)
V11F	FC	-	1	301.15	333	61.74
V11U	MC	UP	1	301.15	333	61.74
V21F	FC	-	2	301.15	165.5	30.87
V21U	MC	UP	2	301.15	165.5	30.87
V21D	MC	DOWN	2	301.15	165.5	30.87
V22U	MC	UP	2	301.15	165.5	61.74
V22D	MC	DOWN	2	301.15	165.5	61.74

4.2 Results and Discussion

4.2.1 Bulk Properties

The rising bulk temperature T_b is plotted in Fig. 4.2(a). It is calculated with Eqn. 4.1. T_b in cases except V22U and V22D rises nearly linearly. As consequences of strong heat flux, V22U and V22D show sharper increases of T_b. The non-linear tendency can be explained with the high C_p close to the pseudo-critical point. At the outlet, T_b approaches T_{pc} without exceeding it. This change of T_b indicates a flow acceleration U_b/U_0 in the downstream direction, as shown in Fig. 4.2(b). U_b/U_0 is calculated with $U_b = 4G/(\rho_b \pi D^2)$, derivated from Eqn. 4.1. Similarly, bulk Reynolds number Re_b is expected to become higher as a result of decreasing viscosity μ_b in axial direction (Fig. 4.2(c)).

Fig. 4.3 shows the mean wall temperature T_w in the axial direction. For the cleanness, the results are summarized in three groups separately. In cases of $D = 1$ mm (Fig. 4.3(a)), the current DNS matches with Bae *et al.* [BYC05] Satisfactorily. T_w in V1U exceeds that of V1F as consequences of buoyancy. The agreement in downward flow V21D with $D = 2$ mm (Fig. 4.3(b)) is excellent, while a qualitative agreement is found in V21U and V22U. In upward flow cases V21U and V22U, a deteriorated heat transfer is captured, followed by a heat transfer recovery.

Evolution of Nusselt number Nu_b and skin friction coefficient C_f in the

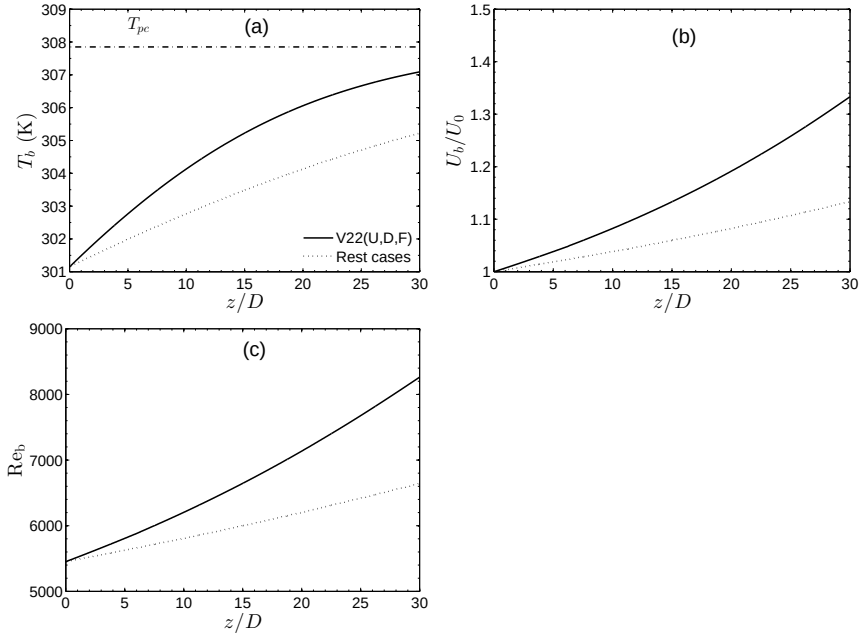

Figure 4.2: Development of bulk temperature T_b (a), bulk velocity U_b/U_0 (b) and bulk Reynolds number $\mathrm{Re_b}$ (c)

axial direction are depicted in Fig. 4.4(a) and Fig. 4.4(b), respectively. At the inlet, $C_f = 0.00894$ matches Blasius correlation $C_f = 0.00897$ with 0.4% difference. Interestingly, forced-convection cases V1F and V2F are found to be strongly similar in both $\mathrm{Nu_b}$ and C_f. Buoyancy leads to the diversity in mixed-convection cases. Under the same conditions, downward flows show an enhanced convective heat transfer (higher $\mathrm{Nu_b}$) compared with upward flows. In the region of thermal entry, a significant low peak is observed in both downward flows V21D and V22D. The reason of that remains unclear. The increasing heat flux results in less significant change for skin friction coefficient C_f. Similarities are observed in both upward flow cases (V21U and V22U) and downward flow cases (V21D and V22D). In the forced-convection cases V1F and V2F, C_f nearly coincide with each other.

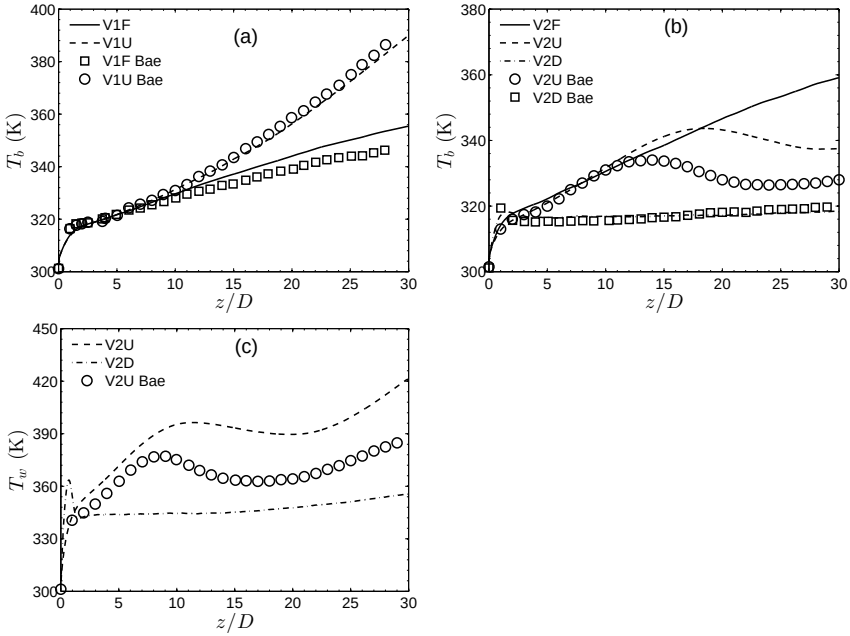

Figure 4.3: Mean wall temperature T_w in the axial direction, results from Bae *et al.* [BYC05] marked with symbols

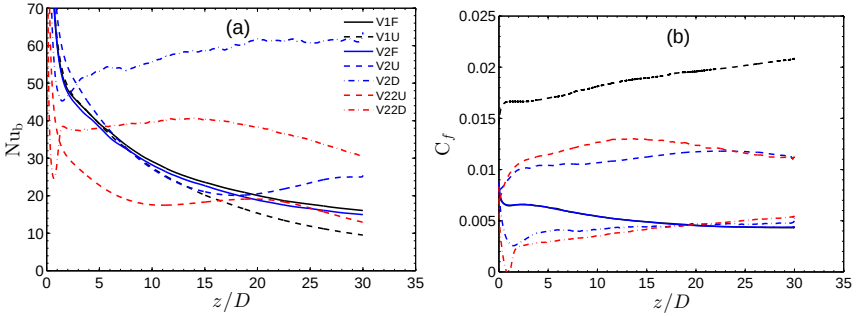

Figure 4.4: Evolution of Nusselt number $\mathrm{Nu_b}$ and skin friction coefficient C_f in the axial direction

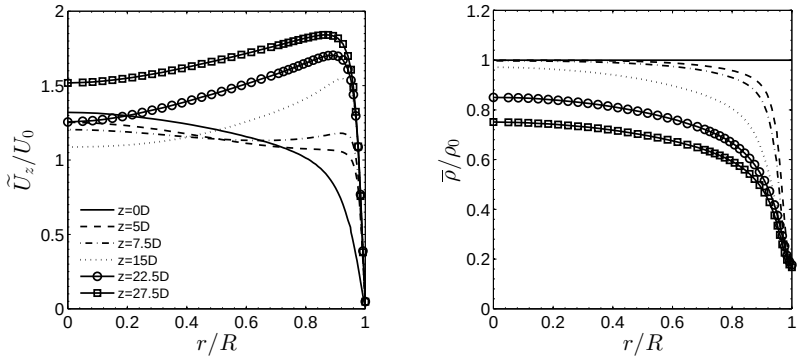

Figure 4.5: mean axial velocity U_z/U_0 and mean density ρ/ρ_0

4.2.2 Mean Flow Statistics

Favre-Average velocity profile U_z/U_0 and Reynolds-average density profile ρ/ρ_0 are depicted in Fig. 4.5(a) and Fig. 4.5(b). The wall heat flux results in strong decreasing of flow density close the wall in the position of $z = 5D$ and $z = 10D$ (Fig. 4.5(b)). Therefore, flow acceleration is observed close to the wall with deceleration in the pipe center. After $z = 7.5D$, the flow profile turns to be a very significant M-shape. In $z = 22.5D$ and $z = 27.5D$, flow at the pipe center begins shows a significant drop of density, which leads to an acceleration of flow at this position.

Using the semi-local wall coordinate as introduced in section 3.3.2, the mean velocity U^+_{VD} is displayed in Fig. 4.7(a). In the laminar sub-layer ($y^* < 12$), U^+_{VD} agrees with each other at different positions. Outside the laminar sub-layer, U^+_{VD} starts to diverge from the original profile and shows a significant M-shape after $z = 15D$. In Fig. 4.7(b), the local mass flux $\overline{\rho U_z}$ considering the local density is given. Compared with local velocity profiles U_z, local mass fluxes $\overline{\rho U_z}$ shows a more identical tendency at different downstream positions. The observed slight M-shape after $z = 15D$ is consistent with the U_z n Fig. 4.5(a) and U^+_{VD} Fig. 4.7(a).

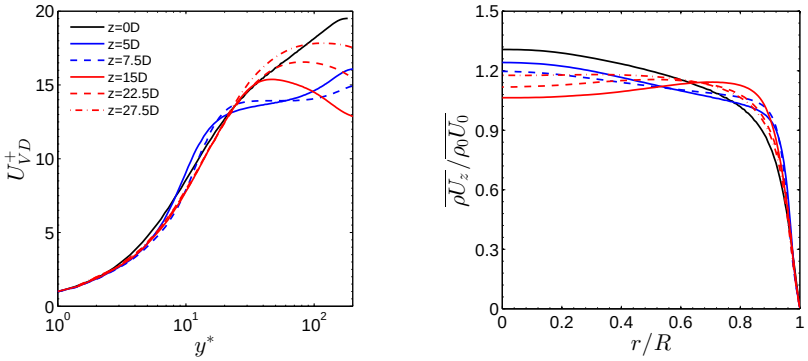

Figure 4.6: Van Driest transformed mean velocity in wall unit U^+_{VD} and local mass flux $\overline{\rho U_z}/\rho_0 U_0$

4.2.3 Turbulence Statistics

Turbulent kinetic energy (TKE) $1/2\overline{\rho U_i'' U_i''}/\tau_{w,0}$ and velocity fluctuation in three directions are shown in Fig. 4.7(a). Peak value of TKE disappears in $z = 5D$ and $z = 7.5D$, which indicates an attenuated turbulence at both positions. In $z = 15D$, TKE is recovered with a similar maximum as the original value. In further downstream direction $z = 22.5D$ and $z = 27.5D$, TKE shows a distinctive distribution with high kinetic energy at the range of $0 < r/R < 0.8$, which is distinguished with the isothermal turbulence field. A further analysis of the velocity fluctuation in three directions is found in Fig. 4.7(b), (c) and (d). When the flow shows relaminarization character in $z = 5D$ and $z = 7.5D$, the most significant reduction is found in $\overline{\rho U_z'' U_z''}$. When the turbulence is recovered in $z = 27.5D$, the peak value of $\overline{\rho U_z'' U_z''}$ is similar as the isothermal turbulence. $\overline{\rho U_r'' U_r''}$and $\overline{\rho U_\theta'' U_\theta''}$ exceed the original value enormously.

When the flow is relaminarized ($z = 5D$ and $z = 7.5D$), Reynolds shear stress $\overline{\rho U_r'' U_z''}$ (Fig. 4.8) loses its peak value at about $r/R = 0.85$. In further downstream direction, a sign change is observed in the majority of radial direction except the near-wall region (about $r/R > 0.9$).

Unlike the flow turbulence statistics, similar distribution in temperature

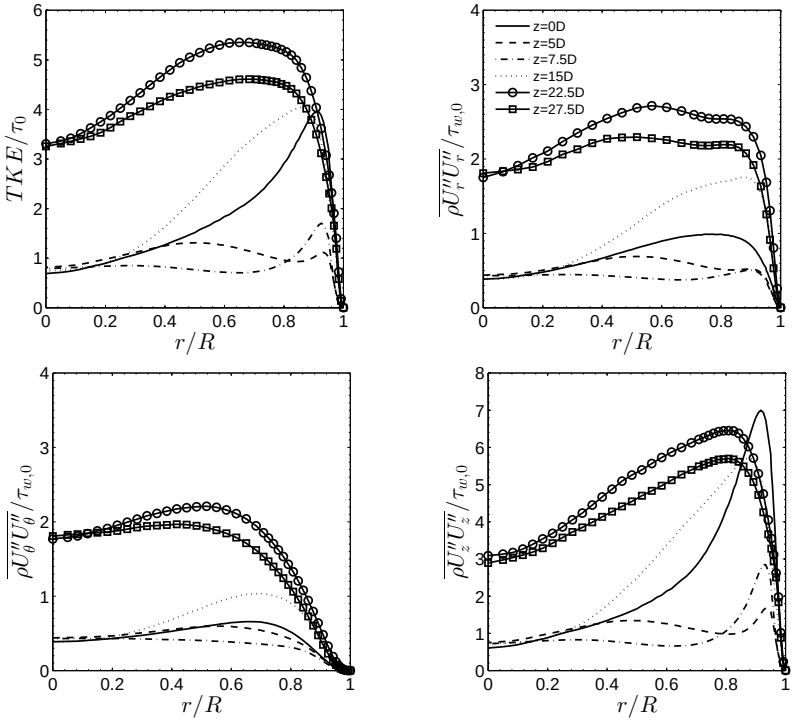

Figure 4.7: Turbulent kinetic energy (TKE) $1/2\overline{\rho U_i'' U_i''}/\tau_{w,0}$ and velocity fluctuation in three directions $\overline{\rho U_r'' U_r''}/\tau_{w,0}$, $\overline{\rho U_\theta'' U_\theta''}/\tau_{w,0}$ and $\overline{\rho U_z'' U_z''}/\tau_{w,0}$

fluctuation $\sqrt{\overline{T'^2}}/\overline{T}$ in Fig. 4.9(a) is observed in different downstream positions. In $z = 22.5D$ and $z = 27.5D$, $\sqrt{\overline{T'^2}}/\overline{T}$ exceeds that in $z = 5D$ and $z = 7.5D$ at $y < 0.2$. It shows the maximum at about $y = 0.03$. As a result of the nonlinearity from the thermo-physical properties, the density fluctuation does not coincide with the temperature fluctuation. The density fluctuation $\sqrt{\overline{\rho'^2}}/\overline{\rho}$ in Fig. 4.9(b) shows slight dissimilarity between relaminarized and transitional flow. In $z = 5D$ and $z = 7.5D$, a steeper and higher peak of $\sqrt{\overline{\rho'^2}}/\overline{\rho}$ is identified.

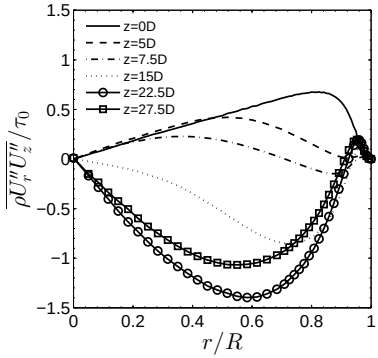

Figure 4.8: Reynolds shear stress $\overline{\rho U_r'' U_z''}/\tau_{w,0}$

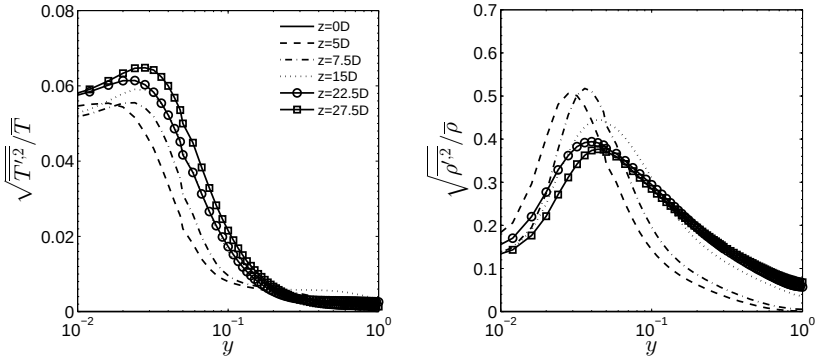

Figure 4.9: Temperature fluctuation $\sqrt{\overline{T'^2}}/\overline{T}$ and density fluctuation $\sqrt{\overline{\rho'^2}}/\overline{\rho}$

Fig. 4.10(a) indicates the attenuated turbulent heat flux in the radial direction $-\overline{\rho U_r'' h''}$ in $z = 5D$ and $z = 7.5D$. A significant recovery of that is observed in the recovered turbulent flow in $0 < r/R < 0.9$.

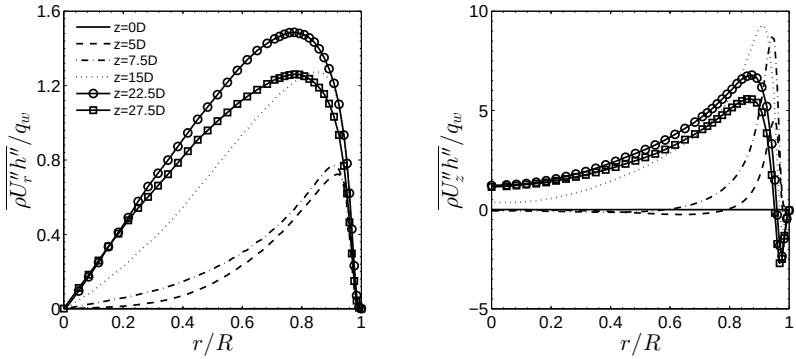

Figure 4.10: Turbulent heat flux $\overline{\rho U_r'' h''}/q_w$ and $\overline{\rho U_z'' h''}/q_w$

4.2.4 Energy Spectrum

In this section, analysis of temporal power spectra density (PSD) is presented. Fig. 4.11 shows the PSD of turbulent kinetic energy (TKE) at $r/R = 0.5$, $r/R = 0.9$ and $r/R = 0.97$ in axial direction, which corresponds to $y_0^+ = y\sqrt{\tau_{w,0}/\rho_0}/\nu_0 = 5$, 18 and 90 based on the inlet properties. TKE is normalized with wall shear stress at the inlet $\tau_{w,0}$, while frequency is normalized with $1/t_\tau = U_\tau/R$. At $r/R = 0.5$, PSD shows a progressive decay at entire frequency range when the flow is relaminarized ($z = 0D \rightarrow z = 5D \rightarrow z = 7.5D$). At $r/R = 0.9$, PSD shows a similar decay as that of $r/R = 0.5$ at low frequency (high wave length) but an enhancement at high frequency range. The PSD in $z = 7.5D$ exceeds that in $z = 5D$, which is in contrast to the observation at $r/R = 0.5$. It indicates that the flow transition occurs in the buffer layer firstly. Besides, the PSD in $z = 15D$ shows a lower distribution than $z = 22.5D$ and $z = 27.5D$ at $r/R = 0.5$ and $r/R = 0.95$. However, it is found to be close to that of $z = 22.5D$ and $z = 27.5D$ at $r/R = 0.9$. This is another proof that flow transition at buffer layer is prior to the laminar sublayer and outer layer.

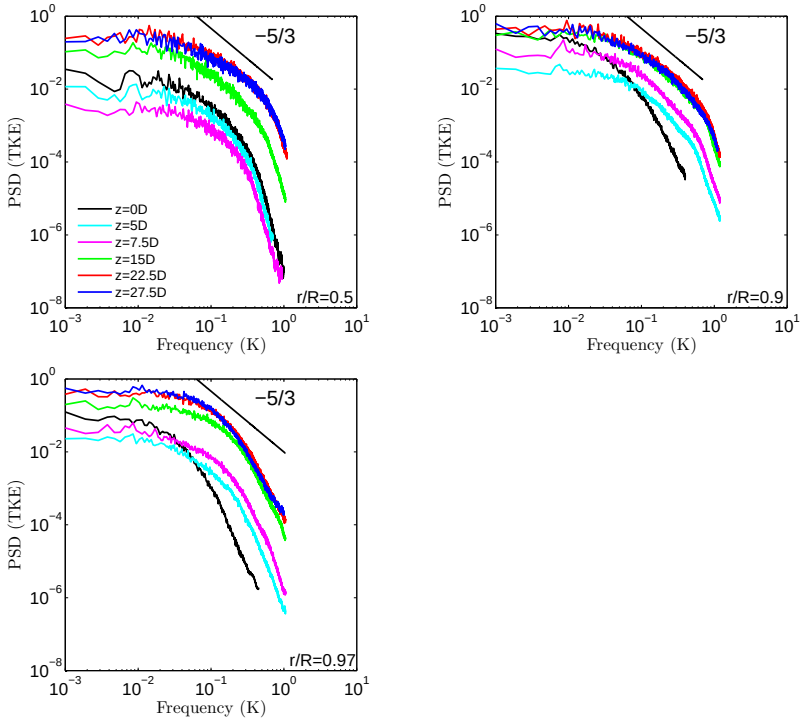

Figure 4.11: Temporal power spectral density (PSD) at $r/R = 0.5$ (a), $r/R = 0.9$ (b) and $r/R = 0.97$ (c)

4.2.5 Gallery

Numerous flow fields are visualized in the current section. Fig. 4.13 shows the development of turbulent streaks $U_z''/\widetilde{U}_z$ in V22U, at $r/R = 0.5$, $r/R = 0.75$, $r/R = 0.9$, $r/R = 0.97$, where $\widetilde{U}_z = f(r,z)$ is the local mean velocity. Based on the isothermal properties, these radial positions can represent different layers of the pipe flow, including the the outer layer ($y^+_{ref} = 91.8$), buffer layer ($y^+_{ref} = 18.4$ and $y^+_{ref} = 45.9$) and laminar sublayer ($y^+_{ref} = 5.5$). In the color scale, warm colors and cold colors indicate high-speed streaks and low-speed streaks, respectively. In the isothermal flows (z=-5D-0D),

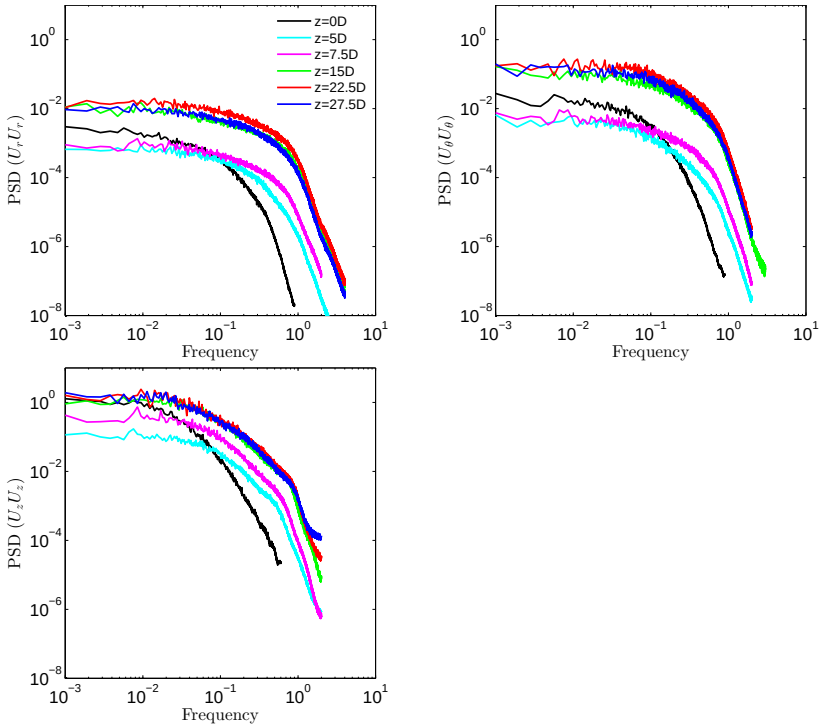

Figure 4.12: Temporal power spectral density (PSD) of $U_r'U_r'$, $U_\theta'U_\theta'$ and $U_z'U_z'$ at $r/R = 0.9$

large-scale ($3D$) structures are identified near the wall at $r/R = 0.9$ and $r/R = 0.97$, which are usually called as turbulent streaks. Just after the inlet ($z = 0D - 5D$) at $r/R = 0.9$, these streaks are quickly broken up into smaller structures and their strength are attenuated. This tendency is less significant in the pipe center ($r/R = 0.5$ and $r/R = 0.75$). These reduced velocity fluctuations are quantified in Fig. 4.7(d). The decomposition of long waves into shorter waves is also proved in the energy spectrum in Fig. 4.12(c). After about $z = 5D$, high-speed streaks (red) are progressively produced at $r/R = 0.9$, exceeding the low-speed streaks (light blue) in magnitude. A delayed production of these high-speed streaks are found at

$r/R = 0.5$ and $r/R = 0.75$. After about $z = 15D$, the high-speed streaks are progressively developed into finer scattered structures at $r/R = 0.9$. On the other hand, the magnitude of the low-speed streaks shows an increasing tendency at $r/R = 0.75$, $r/R = 0.9$ and $r/R = 0.97$. In the isothermal flow, long, thin high-speed and low-speed streaks show up alternatively in the spanwise direction ($r/R = 0.9$). After $z = 20D$, this character only remains at $r/R = 0.97$. In other positions, high-speed streaks and low-speed streaks are concentrated respectively. Besides, the velocity structures show some similarity at $r/R = 0.5$, $r/R = 0.75$ and $r/R = 0.9$, which is not the case in the isothermal flow.

Fig. 4.14 shows the instantaneous velocity field U_z/U_0 of V22U with the radial position as the Y-axis. In the downstream direction, significant flow acceleration is observed near the wall where low-speed flow is filled in the isothermal flow. The low-speed flow is only observed in a very thin layer close to the wall.

In Fig. 4.15, enthalpy fluctuation $he''/\widetilde{he}$ and density fluctuation $\rho''/\overline{\rho}$ of the same case (V22U) at $r/R = 0.9$ and $r/R = 0.97$ are presented. Between $z = 0D - 5D$, a strong enthalpy fluctuation is observed at $r/R = 0.97$ instead of $r/R = 0.9$, in contrast to the further downstream direction after $z = 5D$. As a result of positive heat flux, the strength of high-enthalpy flow ($he'' > 0$ in warm color) exceeds that of low-enthalpy flow ($he'' > 0$ in cold color) after $z = 5D$. In the density fluctuation $\rho''/\overline{\rho}$ at $r/R = 0.97$, low-density flow $\rho'' < 0$ occupies a larger area in the pipe but the high-density flow $\rho'' > 0$ shows a larger magnitude as a result of non-linear fluid property.

The development of turbulent streaks $U_z''/\widetilde{U}_z$ in V21U and V21D is presented in Fig. 4.16 and Fig. 4.17 respectively. In contrast to upward flows, the low-speed streaks persist in the downstream direction from V21D. High-speed and low-speed streaks are nearly uniformly distributed in different radial positions of the pipe.

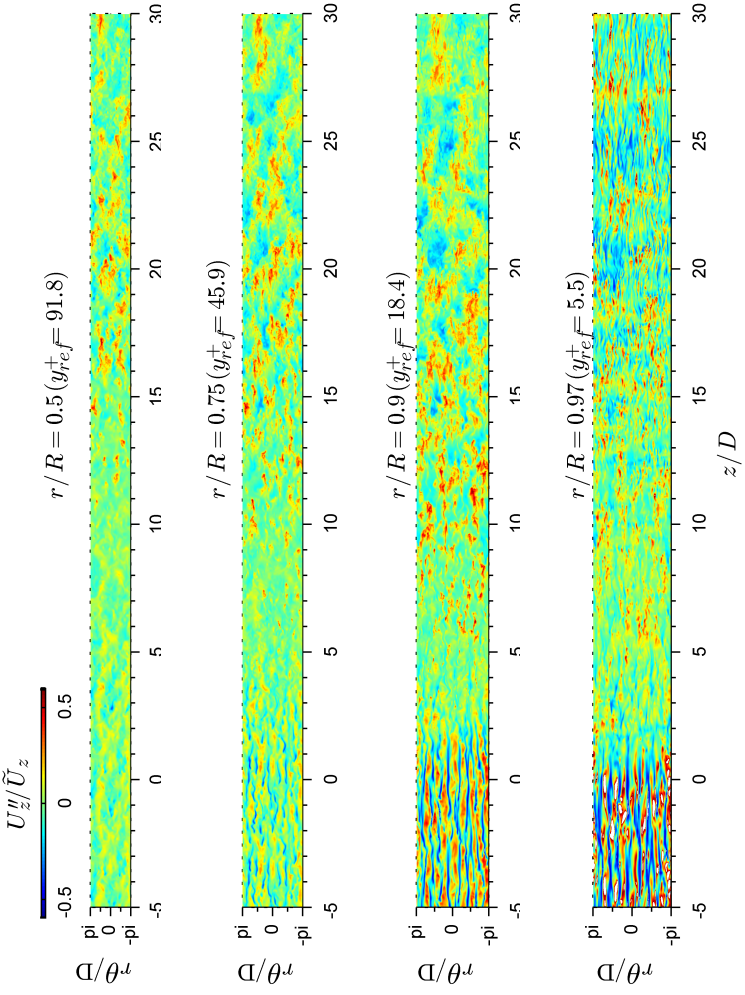

Figure 4.13: Turbulent streaks $U_z''/\widetilde{U}_z$ of case V22U, at $r/R = 0.5$, $r/R = 0.75$, $r/R = 0.9$, $r/R = 0.97$

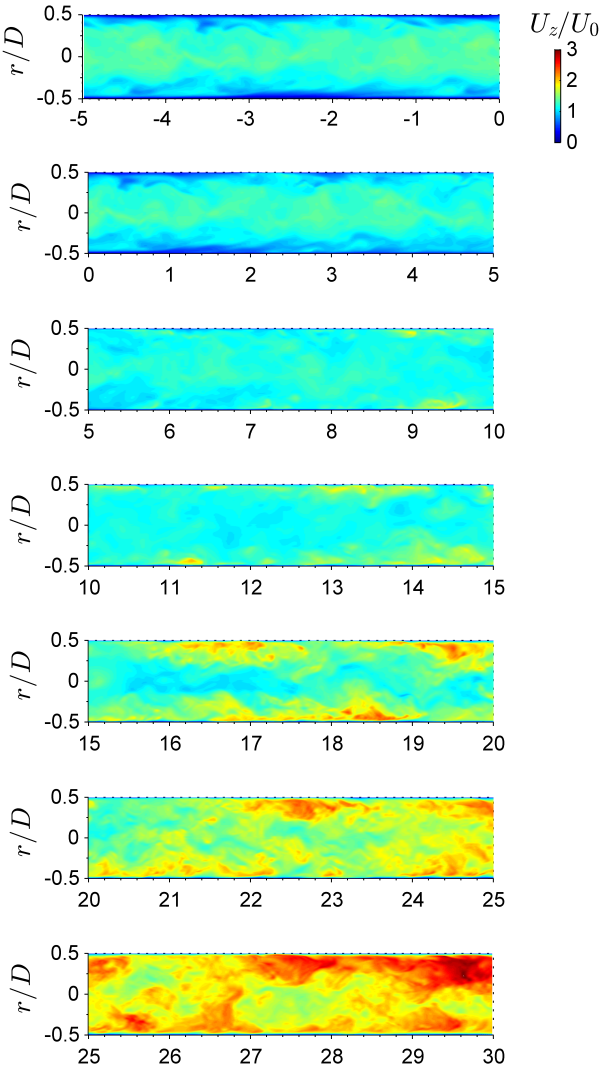

Figure 4.14: Instantaneous velocity field U_z/U_0 of case V22U

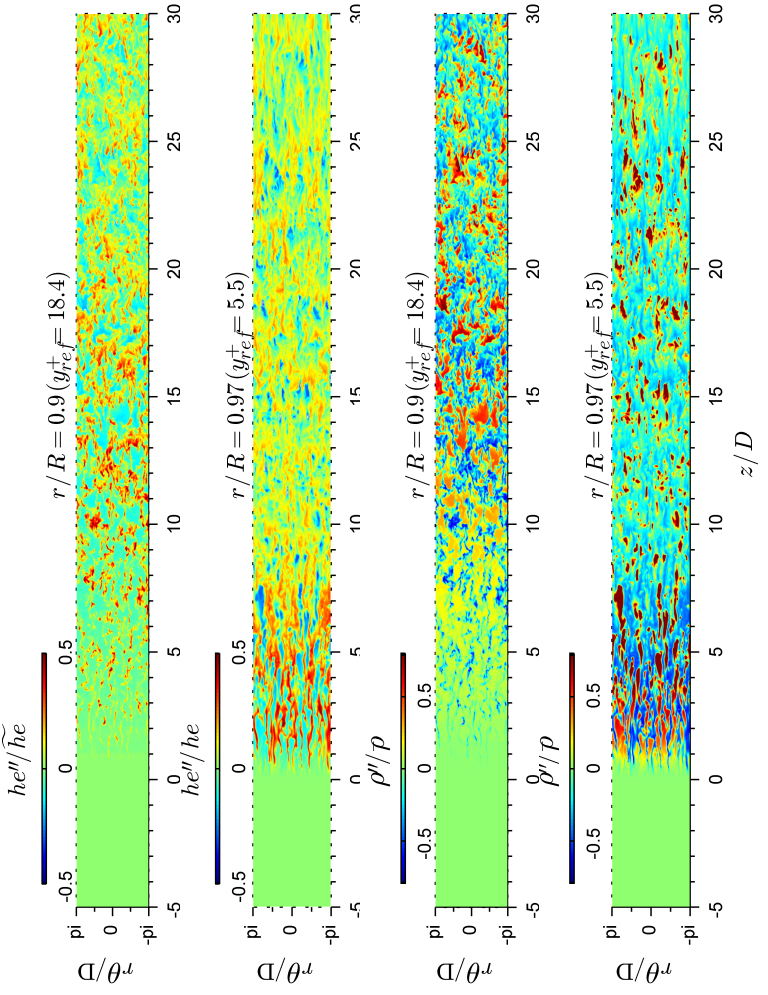

Figure 4.15: Enthalpy fluctuation $he''/\widetilde{he}$ and density fluctuation $\rho''/\overline{\rho}$ of case V22U at $r/R = 0.9$ and $r/R = 0.97$

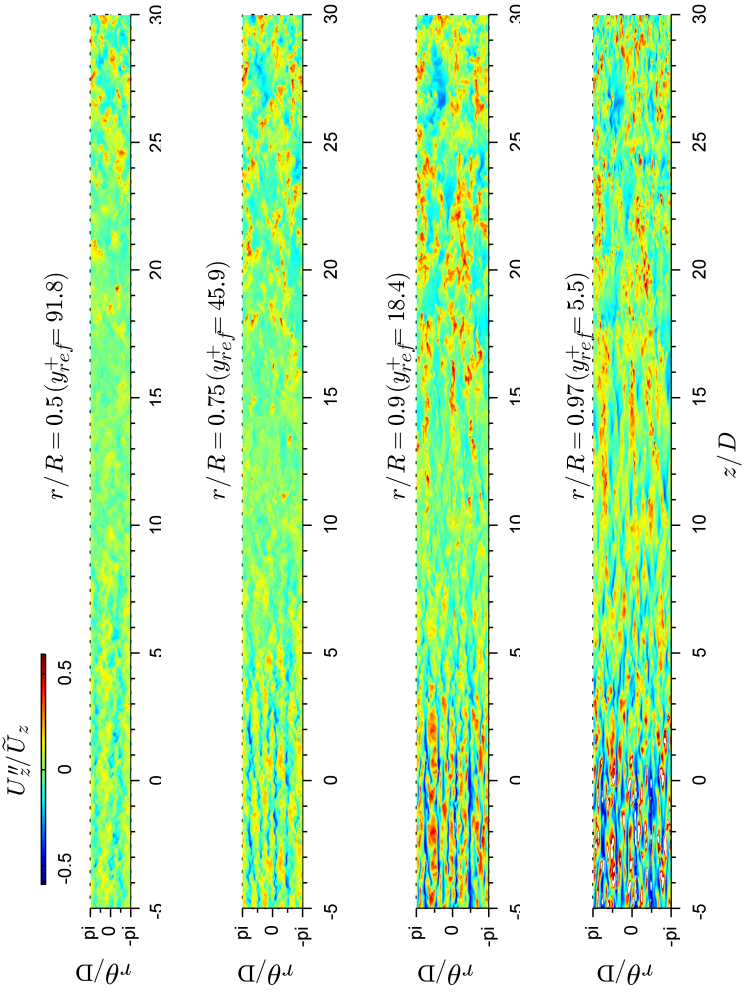

Figure 4.16: Turbulent streaks $U_z''/\widetilde{U}_z$ of case V21U, at $r/R = 0.5$, $r/R = 0.75$, $r/R = 0.9$, $r/R = 0.97$

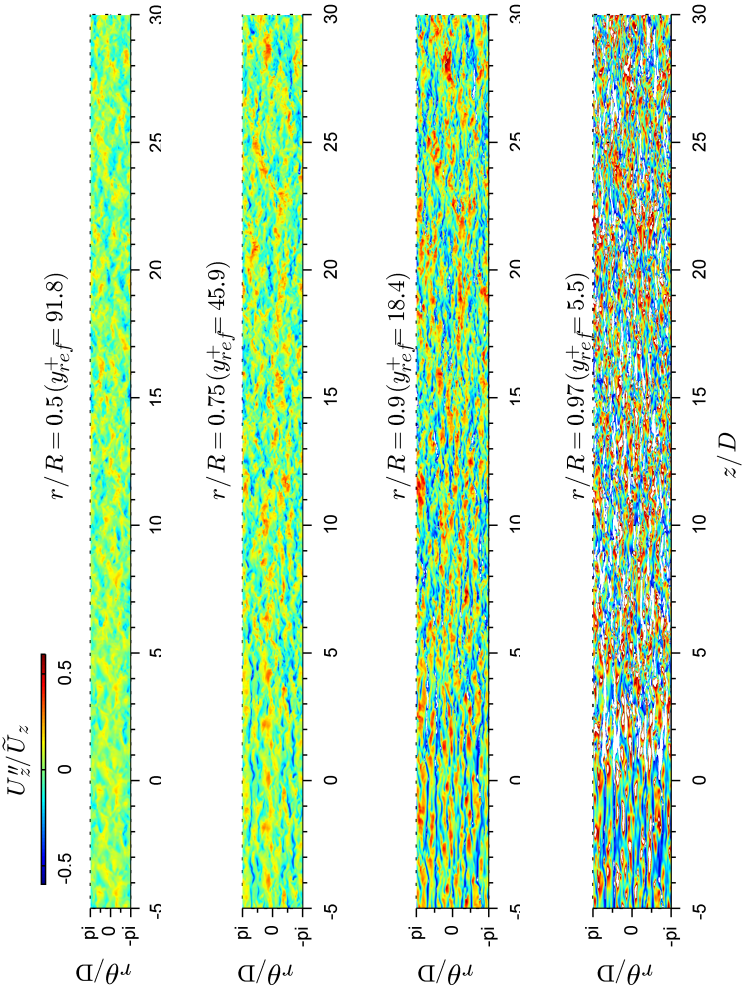

Figure 4.17: Turbulent streaks $U_z''/\widetilde{U}_z$ of case V21D, at $r/R = 0.5$, $r/R = 0.75$, $r/R = 0.9$, $r/R = 0.97$

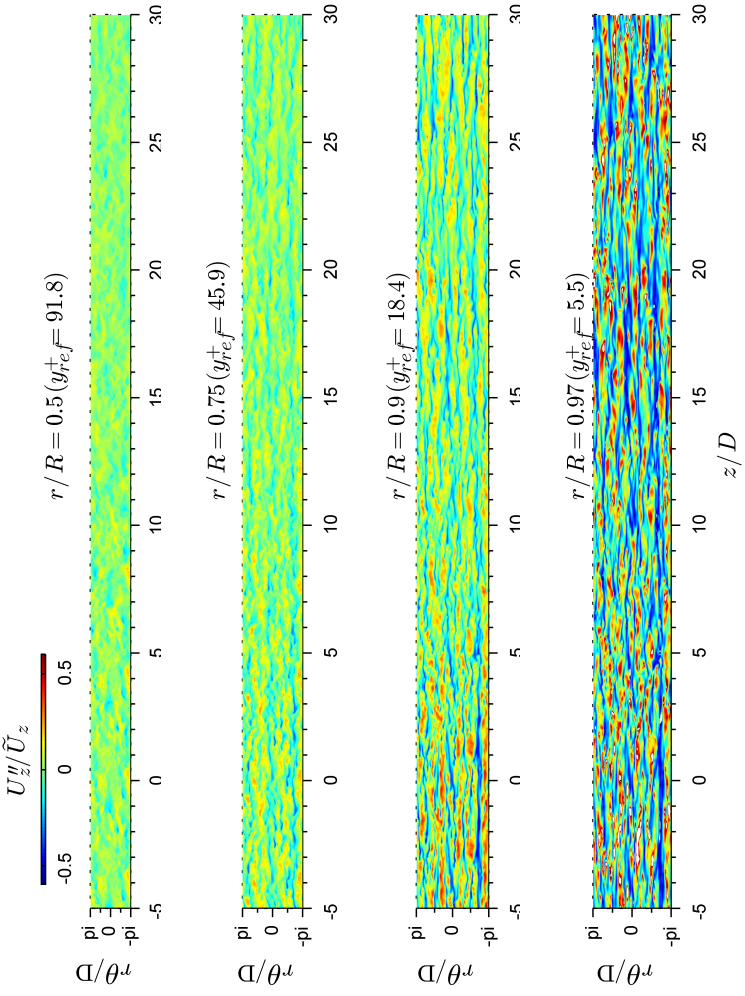

Figure 4.18: Turbulent streaks $U_z''/\widetilde{U}_z$ of case V11F, at $r/R = 0.5$, $r/R = 0.75$, $r/R = 0.9$, $r/R = 0.97$

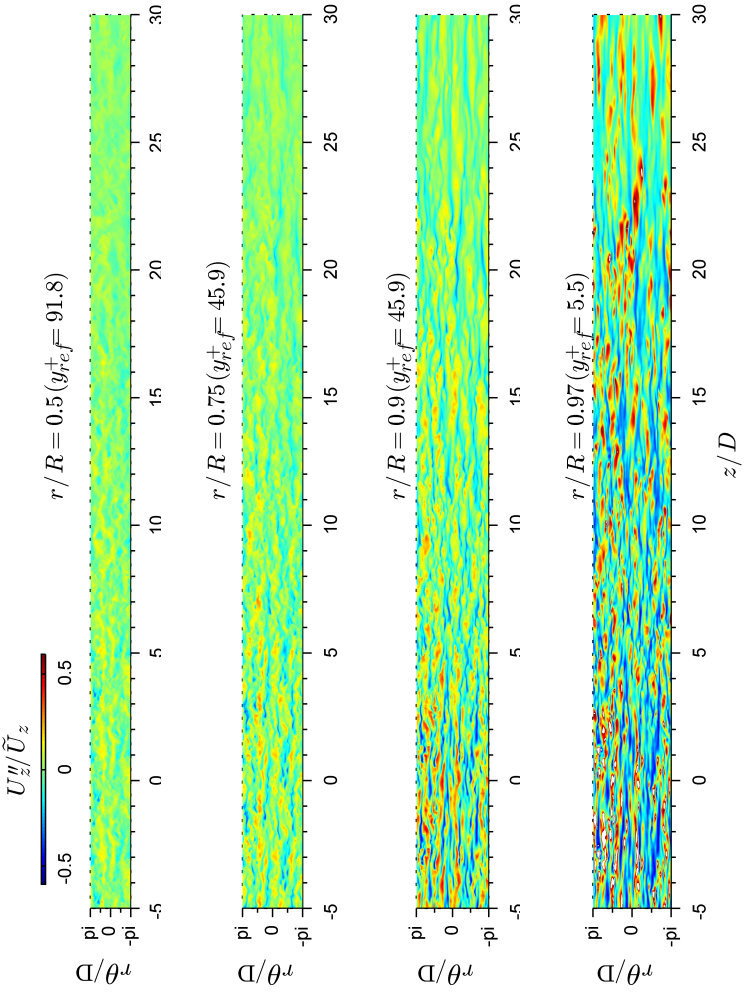

Figure 4.19: Turbulent streaks $U_z''/\widetilde{U}_z$ of case V11U, at $r/R = 0.5$, $r/R = 0.75$, $r/R = 0.9$, $r/R = 0.97$

Chapter 5

Flow Stratification of Supercritical CO_2 in a Heated Horizontal Pipe

In this chapter, heat transfer to supercritical CO_2 in a horizontal pipe is investigated using Direct Numerical Simulation (DNS). The content in this chapter is also included in [CLM16]. A well resolved DNS eliminates the uncertainty brought by turbulence modeling. The small pipe diameter (D =1 mm, 2 mm) with A moderately low inlet Reynolds number ($\mathrm{Re}_0 = 5400$) can be compared to the channel flow in a compact heat exchanger, e.g. a printed circuit heat exchanger (PCHE). In our simulation, the inflow temperature T_0 is set to be lower than the pseudo-critical temperature T_{pc}. The thermophysical properties change rapidly when the fluid temperature rises across T_{pc} under heating conditions. In the present DNS, the wall temperature T_w is found to be variable in the circumferential direction. The magnitude of T_w is higher at top than at the bottom surface. As a result of buoyancy, flow stratification with low density in the upper region of pipe is developed by a

secondary flow, which results from the wall heating. The streamwise velocity field $\widetilde{U}_z$ is also modified by the flow stratification. Low-velocity flow near the circumferential wall is heated firstly and transported to the top region by the secondary flow. High-velocity bulk fluid is concentrated at the bottom as a result of high density. The modification of the velocity field affects the shear production of turbulence near the top surface. Therefore, the turbulent kinetic energy and the radial turbulent heat flux are strongly suppressed in this region. The attenuated convective heat transfer enhances the flow stratification.

5.1 Introduction

Compared with the research of the vertical pipe, horizontal pipe flow draws less attention. The horizontal pipe with heated supercritical CO_2 has also broad industrial applications, such as the printed circuit heat exchanger (PCHE) [KLAC12,MSF+09]. A PCHE is attractive as a highly efficient heat exchanger with a compact size. In a common placement of PCHE, supercritical CO_2 flows through the cold channel horizontally and is heated by the hot channel. Adebiy and Hall [AH76] conducted an experimental investigation of heat transfer to supercritical pressure CO_2 in a horizontal pipe. It was observed that heat transfer at the bottom of the pipe is enhanced and at the top is reduced by buoyancy. Bazargan [BF09] introduced the effect of buoyancy on heat transfer to supercritical water flow in a horizontal tube experimentally. Liao *et al*. [LZ02] in their work focused on measuring the heat transfer coefficients from supercritical CO_2 flowing in horizontal Mini/Micro channels. It was found that the buoyancy effect is still significant in the pipe of diameter D from 0.5 mm to 2.16 mm. The correlation used in large tubes was proved to be invalid in these horizontal Mini/Micro channels. Lei *et al*. [LLYC12,LLZZ13] investigated the effect of buoyancy on heat transfer deterioration of supercritical water in horizontal tubes using RNG $k-\epsilon$ turbulence model. Strong non-uniformity in the circumferential distribution of the tube's inner wall temperature is found in the study. Further analysis showed that rapid change in fluid properties results in complex secondary flows. Cao *et al*. [CRL11] investigated laminar convective heat transfer of supercritical CO_2 in horizontal miniature tube under cooling condition numerically. They found that the results can benefit in the design and optimization of the PCHE with supercritical CO_2.

Based on the previous experience [CKY07,YOI+07,Yoo13], dealing with steep property variation and related complicated flow phenomenon is beyond the ability of RANS. Even if a certain turbulence model has shown some satisfying results in a few cases, its superiority may not be achieved in other cases. On the other hand, only a few experimental studies delivered detailed hydraulic resistance, mean and turbulent velocity, and temperature fields.

The technical difficulties and high cost required for developing such techniques have practically limited the progress of experimental works according to Yoo [Yoo13]. Jackson [Jac13] suggested using high-fidelity DNS or LES to investigate the heat transfer of supercritical fluid and provide a reliable data base for modeling validation and improvement, which has been proved to be feasible in He *et al*. [HKJ08]. Based on the DNS data, Laurien [Lau16] and Pandey [PL16] validated and optimized simple affordable two-layer turbulence model for predicting the heat transfer characters. According to the authors knowledge, no DNS about the supercritical fluid flow in a horizontal pipe has been published, which can offer an insight look of accurate flow mechanism without turbulence modeling. Through the current study, it is expected that the flow pattern of heated supercritical fluid in a horizontal pipe can be displayed and analyzed by DNS. Various simulation conditions will be reported. The pipe geometry is taken as D =1 mm and 2 mm, which is in the range of common PCHE channels. The influence of buoyancy to the heat transfer and flow turbulence of supercritical fluid is going to be our major consideration.

5.2 Computational Details

5.2.1 Numerical Method

Fig. 5.1 shows the pipe geometry and boundary conditions. At the inlet, an inflow generator of the length $L_1 = 5D$ with an isothermal wall is adopted to generate approximately fully developed inflow turbulence. A recycling/rescaling procedure [LWS98] is applied in this domain, which does not require a priori knowledge of turbulent flow profiles. For accelerating the turbulence development, the velocity field is initialized with the perturbation method introduced by Schoppa and Hussain [SH00]. In the second section of the pipe $L_2 = 30D$, constant wall heat flux q_w is applied. The boundary condition of velocity field at the outlet is the convective boundary condition $\frac{\partial \phi}{\partial t} + U_c \frac{\partial (\phi)}{\partial x} = 0$, where ϕ can be any any dependent variable, e.g. the velocity U.

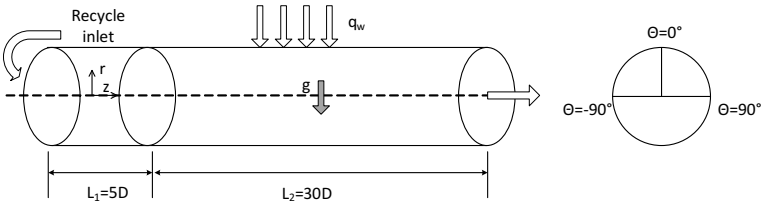

Figure 5.1: Flow domain and boundary conditions

The cylindrical pipe is discretized with a structured hexahedral mesh. The mesh resolution is identical in all cases. The resolution is equivalent to approximately $168 \times 172 \times 400$ (radial r, circumferential θ and axial z direction) for the inflow domain and $168 \times 172 \times 2400$ for the heated domain, when converted from Cartesian to Cylindrical coordinates. The grid mesh is uniformly spaced in the axial direction, and refined near the wall in the radial direction with a stretching ratio of 10, which corresponds to a dimensionless resolution of $0.11\,\text{(wall)} < \Delta y^+ < 1.1\,\text{(center)}, (R\Delta\Theta)^+ \approx 6.5, \Delta z^+ = 4.6$ in wall units, i.e., $y^+ = yU_{\tau,0}/\nu_0$, where friction velocity $U_{\tau,0} = \sqrt{\tau_{w,0}/\rho}$ based the on inlet Reynolds number $\text{Re}_0 = 5400$. The dimensionless resolution in space and time is summarized in Table 5.1, where $\Delta t^+ = \Delta t/t^+$, $t^+ = D/U_\tau$. Compared with the DNS study of Bae *et al.* [BYC05] at the same simulation conditions except the vertical placement of the pipe, the current DNS shows significant improvement of resolution in all three directions and time considering the same second order accuracy in both studies. Cumulatively, the total mesh number in the heated domain is about 10 times as that of Bae *et al.* [BYC05]. At the outlet of pipe, a rise of the Reynolds number should be considered in the mesh resolution, as in Table 5.1. The dimensionless mesh resolution here is still higher than the reference work at the inlet, especially in radial and streamwise direction. Therefore, it is expected that the current mesh is fine enough for handling these simulation conditions. In the post processing, the mesh coordinate transformation from Cartesian coordinate to Cylindrical coordinate is necessary. The flow statistics are obtained through averaging in time. Five flow through time

Position	Re_b	Re_τ	Δy^+_{min}	Δy^+_{max}	$R\Delta\Theta^+$	Δz^+	Δt^+
inlet	5400	360	0.11	1.1	6.5	4.6	1.1×10^{-4}
inlet ([BYC05])	5400	360	0.18	5.4	9.1	14.6	9.8×10^{-4}
outlet (SC260)	8260	500	0.15	1.5	8.9	6.3	1.4×10^{-4}
outlet	6640	424	0.13	1.3	7.6	5.3	1.2×10^{-4}

Table 5.1: Dimensionless mesh resolution at inlet and outlet of the pipe

case	Type	D (mm)	q_w (kW/m^2)	q^+ 10^4	T_0 (K)	$U_{z,0}$ (m/s)
SC160	Mixed	1	61.74	1.44	301.15	0.452
SC230	Mixed	2	30.87	1.44	301.15	0.225
SC230F	Forced (g=0)	2	30.87	1.44	301.15	0.225
SC260	Mixed	2	61.74	2.88	301.15	0.225

Table 5.2: Simulation conditions, identical inlet conditions $Re_0 = 5400$, $P_0 = 8$ MPa

corresponding to 300 times of the turbulence characteristic time ($t = D/U_0$) are performed for the flow development. 10 flow through time is used for generating the turbulence statistics. A total of 15 flow through times is necessary for one single DNS, which is still affordable.

5.2.2 Simulation Conditions

Simulation conditions are given in Table 5.2. Under the condition of the same inlet $Re_0 = 5400$, pipe diameter D and wall heat flux q_w are varied. The pipe diameter is considered to be an important parameter due to buoyancy effects. The first digit in the case name indicates the pipe diameter and the second together with the third one denotes the heat flux. An ending with F represents the forced convection case. The dimensionless heat flux q^+ is defined as $q^+ = q_w/(\rho_0 U_0 C_{p,0} T_0)$. In the forced convection case SC230F, buoyancy is totally absent by omitting the gravity term ($g = 0$) in Eqn.2.2.

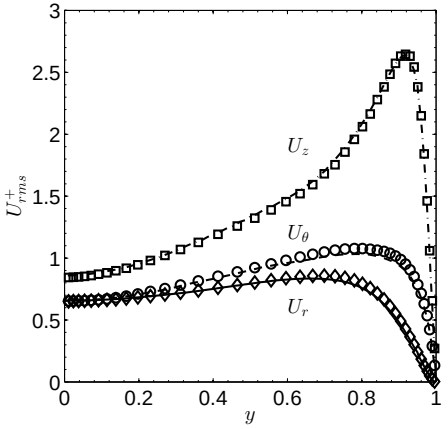

Figure 5.2: Inflow turbulence validation, dimensionless velocity fluctuation U^+_{rms} in r, θ and z direction, lines: current DNS at Re_0=5400, symbols: DNS data from Wu and Moin [WM08] at Re=5300

5.2.3 Inflow Turbulence

The resolution applied in the present DNS exceeds the previously performed reference DNS of Eggels *et al.* [EUW+94]. There, the quality of the inflow turbulence is validated with a better resolved reference DNS data by Wu and Moin [WM08]. This DNS is obtained using a second-order finite difference method. Grid points of $256 \times 512 \times 512$ (r, θ and z direction) are spaced in the $L = 7.5D$ long pipe at Re=5300. The root-mean-square velocity in dimensionless form $U^+ = U/U_\tau$ of three directions is shown in Fig. 5.2. The best agreement is observed in axial direction z, because current dimensionless resolution $z^+ = 4.5$ is similar and even slightly better than the reference work $z^+ = 5.3$. In circumferential direction θ, a small difference is observed due to the lack of grid resolution ($\theta^+ = 6.5$ compared with $\theta^+ = 2.2$ in Wu and Moin [WM08]).

5.3 Results and Discussion

5.3.1 Bulk Properties

Fig. 5.3(a) summarizes the development of the wall temperature T_w on the top- and bottom surfaces of the pipe. T_w is homogeneously distributed in circumferential direction in the forced-convection case SC230F. But buoyancy leads to a non-uniform distribution of wall temperature in circumferential direction. In SC160, SC230 and SC260, T_w is significantly higher on the top surface than on the bottom surface. On the top surface, T_w shows a monotonically rising tendency in all three cases, where the highest T_w distribution is found in SC260 due to high q_w. At the end of the pipe $z = 30D$, the temperature difference ΔT_w between top- and bottom surface is 365.2K (SC260), 234.2K (SC230) and 136.1K (SC160). The distribution of T_w in circumferential direction θ is illustrated in Fig. 5.3. T_w distributes axis-symmetrically in all three cases. In SC160, the peak of T_w is found at $\theta = 0°$ as the other two cases. It is more significant from SC230 and SC260 that T_w shows a very rapid change at $\theta = \pm(30 \sim 50)°$ depending on cases and location. In downstream direction, the location of a high temperature gradient moves away from the top surface ($\theta = 0°$), which means an expansion of the high temperature area.

The streamwise distribution of the local Nusselt number Nu= $\frac{hD}{\kappa_b}$ of top- and bottom surfaces is given in Fig. 5.3(b), where h is a convective heat transfer coefficient $h = \frac{q_w}{T_w - T_b}$ and κ_b is the thermal conductivity evaluated with the local bulk temperature T_b. Here, the Nusselt number (Nu) on the bottom surface is significantly higher than on the top surface in all buoyancy-relevant cases. This indicates a significant difference in convective heat transfer on both sides of the wall surface. In SC230 and SC260, the distribution of Nu on the top surface is close to each other after about $z = 10D$, although SC260 is applied with the wall heat flux two times as that for SC230. But as for the bottom surface, Nu from SC230 is significantly higher than from SC260, which indicates that the largest ΔNu=$\mathrm{Nu_{bottom}}$-$\mathrm{Nu_{top}}$ is found in SC230. The smallest ΔNu is found in SC160, which implies that

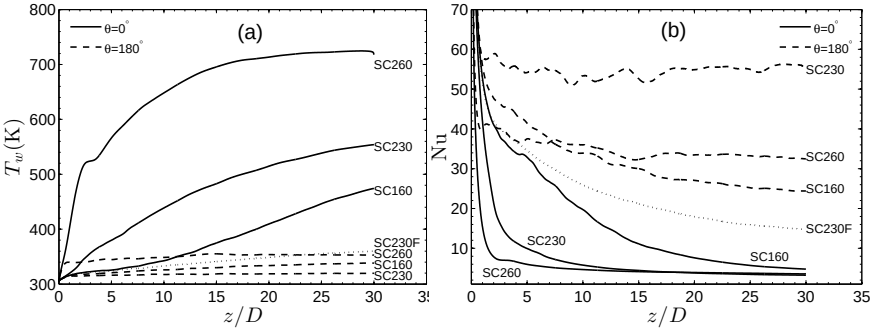

Figure 5.3: Development of T_w (a) and Nu (b) in the downstream direction

buoyancy has less influence to heat transfer for a pipe with smaller radius ($D = 1$ mm against $D = 2$ mm).

Fig. 5.5(a) shows the evaluation of $\mathrm{Re_b}$ along the pipe, which is defined as:

$$\mathrm{Re_b} = \frac{U_b D}{\nu_b} = \frac{GD}{\mu_b}, \mu_b = f(T_b) \tag{5.1}$$

where G (kg/m^2 s) is the mass flow flux density and μ_b is the dynamic viscosity evaluated at the local bulk temperature. With the input of wall heat flux, the bulk temperature rises in the downstream direction, which leads to a decrease in μ_b. Therefore, the bulk Reynolds number $\mathrm{Re_b}$ rises. SC260 indicates a faster increase in $\mathrm{Re_b}$ as a result of high q_w. All other cases show almost the same development. At the outlet of the pipe ($z = 30D$), $\mathrm{Re_b}$=8300 is reached in SC260, and $\mathrm{Re_b}$=6600 in all other cases.

The skin friction coefficient $C_f = 2\tau_w/(\rho_b U_b^2)$ distribution based upon the local wall shear stress τ_w, local ρ_b and U_b is summarized in Fig. 5.4(b). At the inlet, $C_{f,0} = 0.00896$ matches the Blasius estimation $C_f = 0.079\mathrm{Re}^{-0.25} = 0.00897$ with 0.15% difference. In the downstream direction, C_f on the bottom of the pipe is higher than on the top surface in SC160 and SC230. On

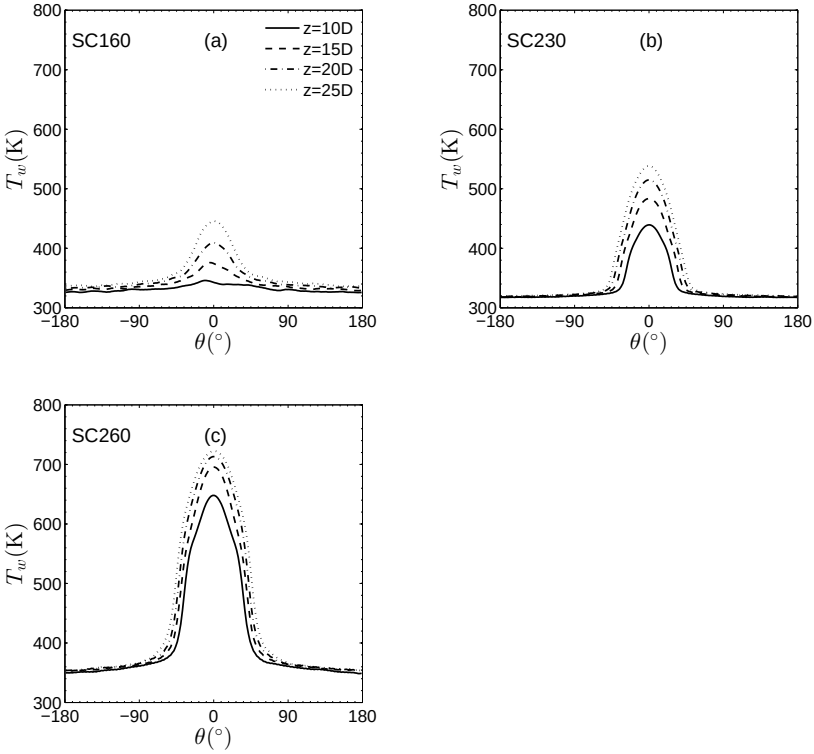

Figure 5.4: Distribution of T_w in circumferential direction θ, (a): SC160, (b): SC230 and (c): SC260

the bottom surface, C_f in SC230 and SC260 shows similar development. But on the top surface, SC260 shows an increasing tendency after about $z = 3D$, which is not clearly observed in SC230. Fig. 5.6 shows the distribution of C_f in circumferential direction θ. Unlike T_w in Fig. 5.4, a monotonical tendency in the half circumference is not observed in C_f. At $z = 25D$ of SC160, C_f shows a nearly flat distribution at about $-20° < \theta < 20°$ near the top surface. Observing from bottom- to top surface ($\theta = \pm 180°$) in SC230 and SC260, C_f begins to decrease to the minimum and then rises up again. This minimum

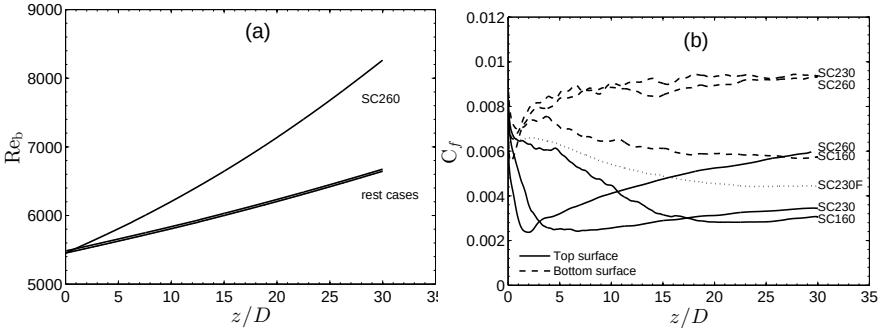

Figure 5.5: Evaluation of Re_b (a) and C_f (b) in the downstream direction

is observed at about $\theta = \pm(20^\circ \sim 40)^\circ$.

The Richardson number Ri is applied for quantification of stratified flow due to buoyancy. The evaluation of the Richardson number,

$$\mathrm{Ri} = \frac{\mathrm{Gr}}{\mathrm{Re}^2},\ \mathrm{Gr} = \frac{\rho_b - \rho_w}{\rho_b}\frac{gD^3}{\nu_b^2} \tag{5.2}$$

It is shown in Fig. 5.7 and indicates the relation between natural and forced convection. Cases with $\mathrm{Ri} > 0.1$ are expected to be buoyancy relevant. SC230 and SC260 exceed this value on both surfaces in the downstream direction, and SC160 shows about one order of magnitude lower value of $\mathrm{Gr}/\mathrm{Re}^2$ as a result of smaller pipe diameter. Adebiy and Hall [AH76] has used the criterion proposed by Jackson for the absence of buoyancy effects in horizontal flow, defined as follow

$$\frac{\mathrm{Gr}}{\mathrm{Re}^2}(\frac{\rho_b}{\rho_w})(\frac{z}{D})^2 < 10, \text{ for buoyancy irrelevant cases} \tag{5.3}$$

SC230 and SC260 show a value about 2000 on the top surface and about 500 on the bottom surface. In SC160, this value becomes about 200 on the top surface and 90 on the bottom surface. It means buoyancy must be considered in these cases, especially in SC230 and SC260.

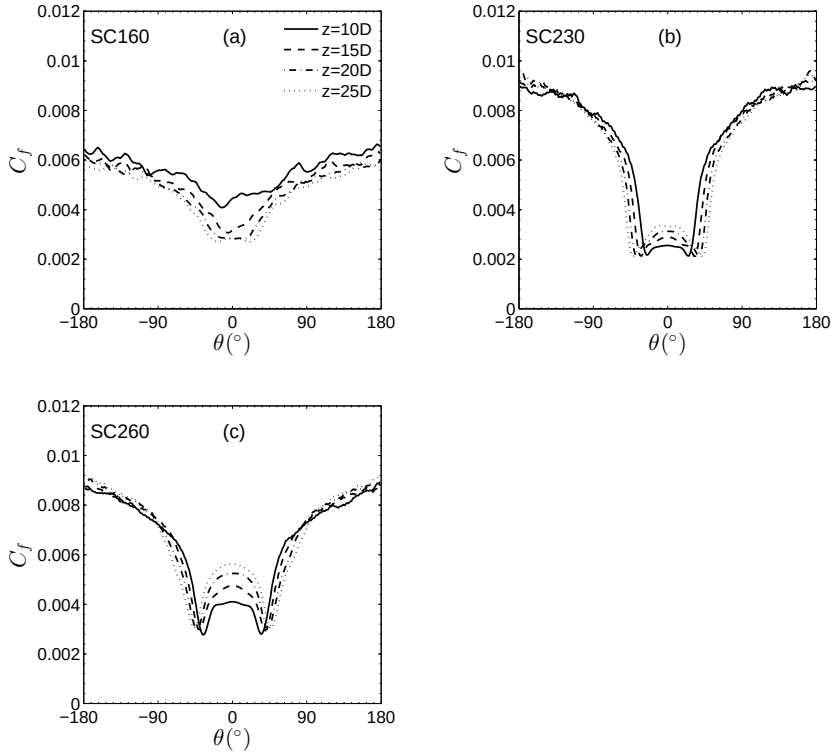

Figure 5.6: Distribution of C_f in circumferential direction θ, (a): SC160, (b): SC230 and (c): SC260

5.3.2 Average Flow Field

In the turbulence statistics below, the mean quantities are defined with Reynolds- and Favre averaging, where $\bar{\phi}$ is the Reynolds average of any quantity and $\widetilde{\phi} = \frac{\overline{\rho\phi}}{\overline{\rho}}$ is the mass-weighted (Favre) average. The corresponding fluctuations are denoted with $\phi' = \phi - \bar{\phi}$ and $\phi'' = \phi - \widetilde{\phi}$.

Figs. 5.8 - 5.10 demonstrate the development of various average flow profiles in the downstream direction of SC160, SC230 and SC260. From top to bottom, velocity $\widetilde{U}_z/U_{z,0}$, temperature $\overline{T}$ (K), density $\overline{\rho}/\rho_0$, thermal

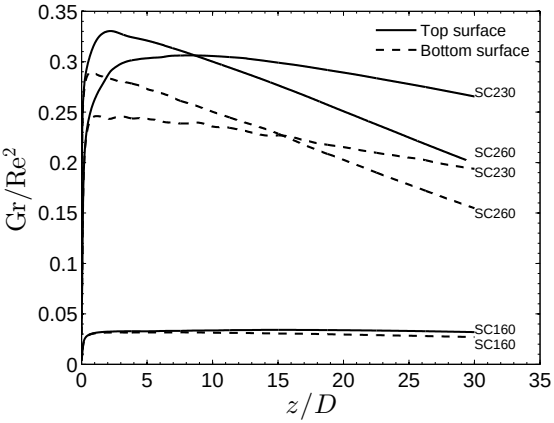

Figure 5.7: Evaluation of $\mathrm{Gr}/\mathrm{Re}^2$ in the downstream direction on top- and bottom surfaces

capacity $\overline{C}_p/C_{p,0}$ are presented. In the following subsections, each case will be discussed separately.

Case SC160 (Fig. 5.8) is characterized with less flow stratification as a consequence of the smaller pipe diameter $D = 1$mm. The bulk velocity profile $\widetilde{U}_z/U_{z,0}$ shows a tendency of accelerating from $z = 5D$ to $z = 25D$, because fluid density is reduced when bulk temperature T_b rises. A nearly homogeneous velocity profile in circumferential direction is observed, which means buoyancy effect is not significant on velocity field. Slight deformation of the velocity profile is found near the top wall at $z = 20D$ and $25D$, which is quantified in Fig. 5.11. At $\theta = 0°$, $\widetilde{U}_z$ is observed as the lowest on the whole domain $0 < r/R < 1$. From the top surface $\theta = 0°$ to the bottom surface $\theta = 180°$, $\widetilde{U}_z$ shows an increasing tendency.

In the second row, the average flow temperature $\overline{T}$ (K) is shown. $\overline{T}$ rises firstly near the wall due to wall heat flux. Then, a thin layer of high-temperature fluid is developed near the top wall. The rest of the fluid is still cold, which means that a stratification of flow temperature is developed in the pipe. The temperature difference between the top and bottom wall surfaces reaches about 136 K at $z = 25D$. This stratification can be also

observed in the density field $\overline{\rho}/\rho_0$ in the third row. When the flow temperature rises beyond pseudo-critical point, the density drops down sharply. As a result of buoyancy, low-density flow progressively gathers near the top surface and high-density flow is concentrated at the bottom. For supercritical CO_2, peak value of thermal capacity $\overline{C}_p/C_{p,0}$ is observed in a narrow temperature window of pseudo-critical temperature. Therefore, it can be used to determine the location of flow with pseudo-critical temperature. In the downstream direction, a horizontal layer of high $\overline{C}_p$ is gradually formed. It separates the high-temperature flow on the top from the cold flow on the bottom.

Compared with SC160, the stronger buoyancy effect in SC230 leads to a deformation of the average velocity profile as shown in the first row of Fig. 5.9. At $z = 10D$, high-velocity fluid with low density begins to accumulate in the bottom section and low-velocity fluid with low density occupies the upper part of pipe cross section. High-velocity flow takes a crescent shape at this position. At $z = 15D$ and $20D$, a small area of high velocity flow is developed close to the top wall surface and it connects with the major part of high-velocity flow at $z = 25D$. The high-velocity flow is found to have an anchor shape at this position. The quantitative analysis of velocity field at $z = 25D$ is as shown in Fig. 5.11(b). At $\theta = 0°$, a velocity peak is observed at about $r/R = 0.75$, which corresponds to high-velocity region near the top wall. Compared with that, the velocity profile at $\theta = 45°$ shows a low value from $r/R = 0.4$ to $r/R = 0.9$, which is also visualized in Fig. 5.9. This can be explained by transport by a secondary flow. Low-velocity flow close to the circumferential wall flows upwards due to low density and drops down at about $\theta = 45°$. Therefore, a low velocity region is developed here.

The stratification of the temperature field is similar to that observed in SC160. The hot flow gathers near the top surface and it shows a significant temperature difference against the cold flow on the bottom. Compared with SC160, this hot layer becomes thicker. This change of the temperature field is also reflected in the density field in the third row. Due to buoyancy, high-temperature CO_2 with low density concentrates on the upper side of cross section. With the input of wall heat flux, low density layer is growing

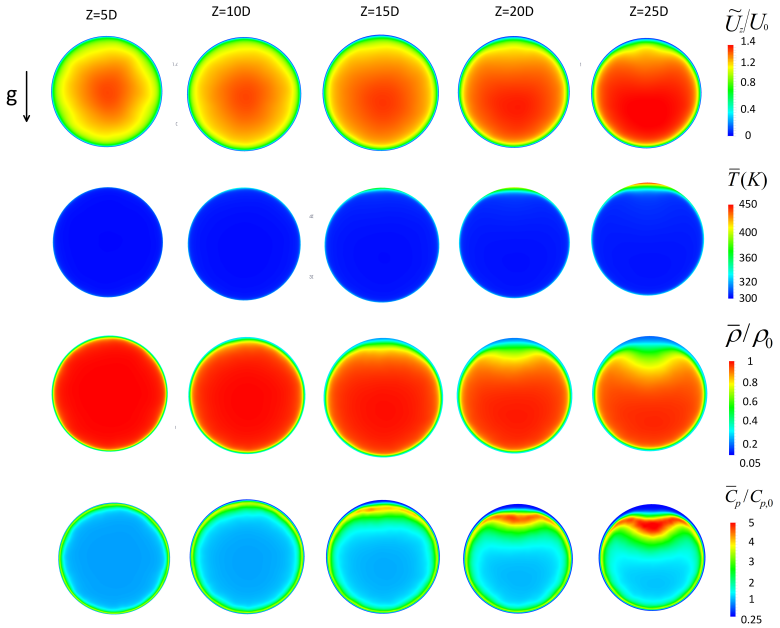

Figure 5.8: Development of flow field and thermal field of SC160 in the downstream direction, velocity $\widetilde{U}_z/U_{z,0}$, temperature $\overline{T}$ (K), density $\overline{\rho}/\rho_0$, thermal capacity $\overline{C}_p/C_{p,0}$

in the downstream direction.

SC260 is based on SC230 with double heat flux q_w applied on the wall. A significant difference from SC230 existing in the velocity field $\widetilde{U}_z/U_{z,0}$ is the strong acceleration of high-velocity region near the top wall, especially in $z = 20D$ and $25D$. It makes the flow in that region significantly faster than in the bulk region. This flow acceleration is also identified in Fig. 5.11(c). At $\theta = 0°$, a velocity peak is observed at about $r/R = 0.7$, which is less significant in SC230 (Fig. 5.11(b)). At the other three positions

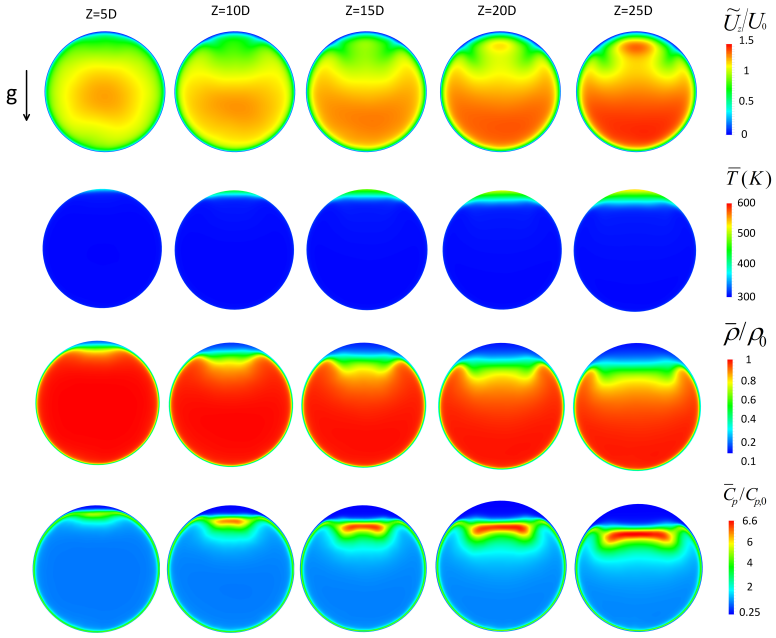

Figure 5.9: Flow field of SC230 in the downstream direction, velocity $\widetilde{U}_z/U_{z,0}$, temperature $\overline{T}$ (K), density $\overline{\rho}/\rho_0$, special thermal capacity $\overline{C}_p/C_{p,0}$

$\theta = 45°$, 90°, 180°, the distribution of profiles show some similarity to that in Fig. 5.11(b). But $\widetilde{U}_z$ is generally higher in SC260 as a result of high q_w.

In the density field (third row of Fig. 5.10), more low-density flow is found in SC260 than SC230. The high $\overline{C}_p$ layer moved further toward bottom surface, which means expansion of the flow region that exceeds the pseudo-critical temperature.

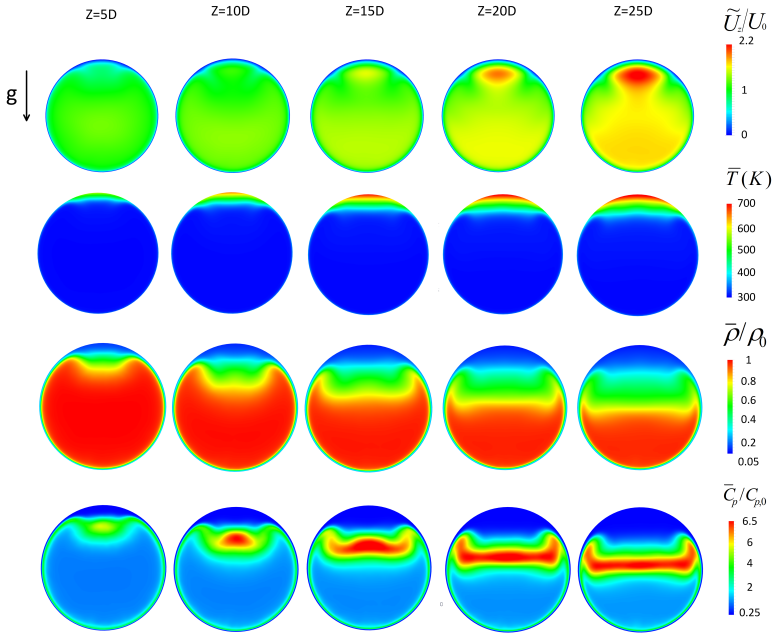

Figure 5.10: Flow field of SC260 in the downstream direction, velocity $\widetilde{U}_z/U_{z,0}$, temperature $\overline{T}$ (K), density $\overline{\rho}/\rho_0$, thermal capacity $\overline{C}_p/C_{p,0}$

5.3.3 Secondary Flow

The vector plots of the 2-D average velocity fields over the cross section are given in Fig. 5.12 and 5.13. The lines are colored with the normalized density value $\overline{\rho}/\rho_0$. The visualization shows that buoyancy brought in by enormous density differences leads to the formation of the secondary flow. Following the path of velocity in all four figures in SC230 (Fig. 5.12), it is observed that flow near the circumferential wall (marked in blue) is

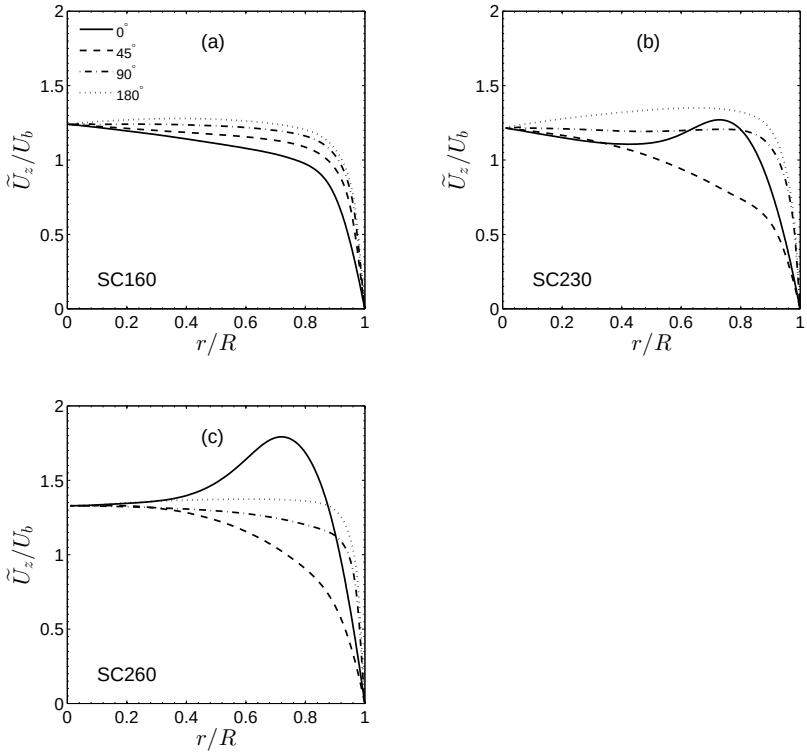

Figure 5.11: velocity profile $\widetilde{U}_z/U_b$ at $z = 25D$, (a): SC160, (b): SC230, (c): SC260, legend is identical as shown in (a)

heated by the wall heat flux q_w initially, which leads to a significant drop in density. As a result of buoyancy, this low-density flow near the wall, flows upward along the wall surface and meet near the top surface. Then it falls down in the gravitational direction along the centerline. The centers of the cortex pair are located nearly axis-symmetrically on the lateral sides. At these four streamwise positions, the positions of vortex center are slightly different. Comparing the figures horizontally ($z = 10D$ to $z = 15D$, $z = 20D$ to $z = 25D$), vortex center moves downwards. In the downstream direction,

the stratified layer with low-density flow is growing progressively, but the center of each vortex of the secondary flow is filled with high-density fluid (colored in red) while located just slightly below a layer between high- and low density flow, which is colored in yellow in the figure.

In SC260 (Fig. 5.13), high heat flux leads to a faster growing low-density layer. At $z = 25D$, about half of the cross section is occupied by low-density flow (marked with blue and green). Similar to SC230, vortex centers at all four positions are always found in the flow with high density. The movement of vortex centers in the gravitational direction is more significant in the downstream direction.

The strength of secondary flow is quantified with average velocity profile $\widetilde{U}_r/U_b$ and $\widetilde{U}_\theta/U_b$ as in Fig. 5.15. At $\theta = 45°$, $\widetilde{U}_r$ shows a maximal strength of about 6% of the local bulk velocity U_b. The non-zero part of $\widetilde{U}_r$ at $\theta = 180°$ indicates the secondary flow in the gravity direction, as shown Fig. 5.12 and Fig. 5.13. At $\theta = 90°$, $\widetilde{U}_\theta$ indicates a strength of 13% in SC230 and 19% in SC260.

5.3.4 Turbulence Statistics

Fig. 5.15 illustrates the evolution of the turbulent kinetic energy $TKE = \frac{1}{2}\overline{\rho U_i'' U_i''}$, which indicates the intensity of the velocity fluctuation in the downstream direction. The TKE shows a decreasing tendency in all three cases. Because of the same inlet Reynolds number $\mathrm{Re}_0 = 5400$, they are expected to give a similar distribution of TKE in the inlet section. After a length of five diameters in downstream direction, the TKE shows the fastest decrease in SC260. Besides, the TKE is no more homogeneous in circumferential direction in SC260. Near the top surface, a region of low TKE appears, which is less obvious in SC230 at this position. In SC230, the ring of high TKE starts to deform at about $z = 10D$. It is broken by the low-TKE region near the top surface and bent towards the pipe center at the breakpoints. Similar distribution of the high-TKE ring is observed in its downstream direction at $z = 15D$, $20D$ and $25D$. In SC160, the reduction of TKE is also observed near the top surface starting at about $z = 15D$. The TKE

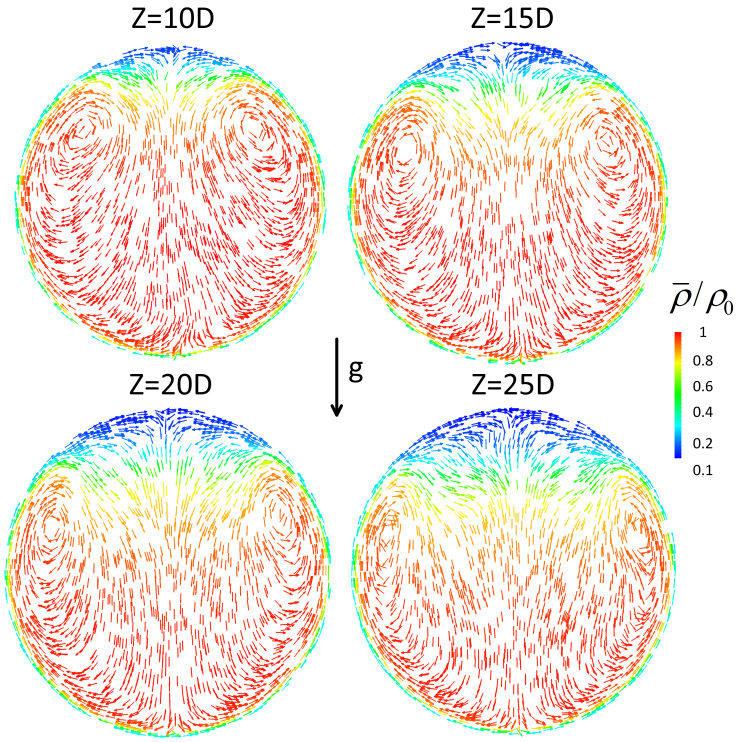

Figure 5.12: Vector plot of the 2-D average velocity field of SC230 at flow downstream positions

distribution in SC260 is qualitatively similar to SC230, but it is noticeable that starting from $z = 20D$ near the top wall surface, a region of high TKE begins to build up, which cannot be clearly identified in SC230.

A quantitative analysis of the TKE at $z = 25D$ in various circumferential directions is shown in Fig. 5.16. The profile from isothermal flow at $z = 0D$ is given with the symboled line as a reference. At $z = 25D$, the TKE at all circumferential directions in these cases is reduced compared with that of isothermal flow. In the direction of $\theta = 0°$, the relative peak of the TKE near the wall disappears in SC160 and SC230. In SC260, TKE shows a character

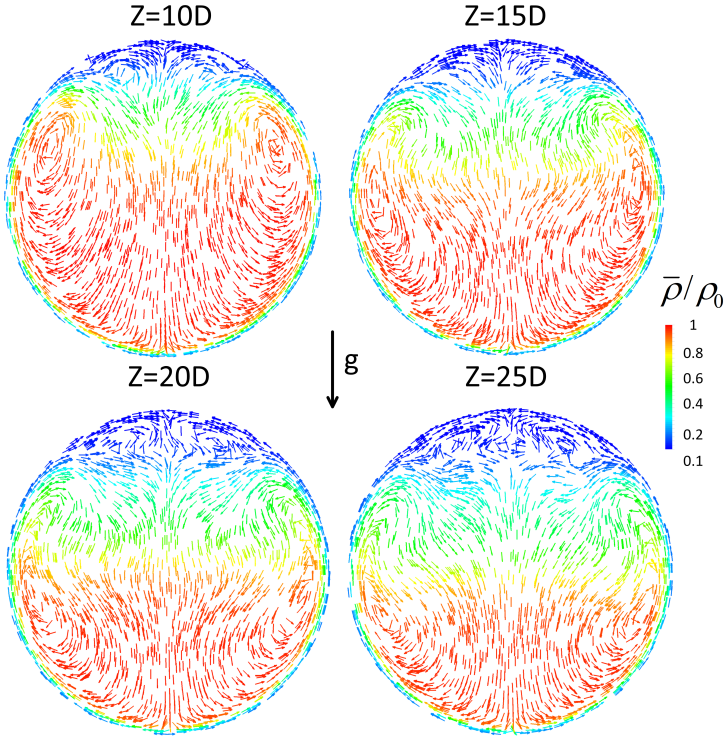

Figure 5.13: Vector plot of the 2-D average velocity field of SC260 at flow downstream positions

of two peaks instead of a single peak in this direction. The peak near the wall ($0.8 < r/R < 0.9$) corresponds to a recovery of TKE in the right figure of the third row in Fig. 5.15. It is also the position, where a strong velocity gradient brought by flow acceleration was observed in Fig. 5.11. In SC230 and SC260, a broad peak away from the wall ($0.6 < r/R < 0.8$) is found in the direction $\theta = 45°$, which is absent in SC160.

In Fig. 5.17, a decomposition of TKE into velocity fluctuations in three directions $\overline{\rho U_r'' U_r''}$, $\overline{\rho U_\theta'' U_\theta''}$ and $\overline{\rho U_z'' U_z''}$ is presented. In SC230, $\overline{\rho U_r'' U_r''}$ is significantly attenuated in $\theta = 0°$, while the peak value in $\theta = 180°$ is

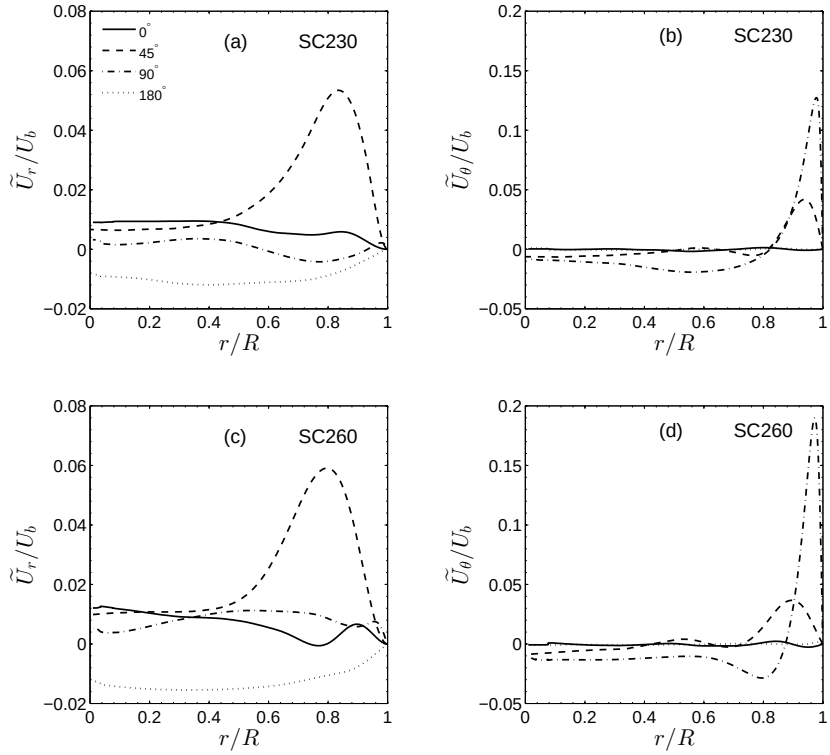

Figure 5.14: velocity profile $\widetilde{U}_r/U_b$ and $\widetilde{U}_\theta/U_b$ at $z = 25D$, legend is identical as shown in (a)

also decreased. In SC260, $\overline{\rho U_r'' U_r''}$ shows a rising peak in $\theta = 0°$ at about $r/R = 0.3$, which is located between the lateral vortex centers as seen in Fig. 5.19. At $\theta = 45°$, the secondary flow leads to a radial transport as illustrated in Fig. 5.18 and Fig. 5.19. This comes with a significantly larger radial velocity fluctuation $\overline{\rho U_r'' U_r''}$ at about $r/R = 0.6$. The attenuated $\overline{\rho U_\theta'' U_\theta''}$ in $\theta = 0°$ (Fig. 5.17(c)) suggests a low turbulent mixing in the circumferential direction. In the case SC260, a two-peak character in $\theta = 0°$ is observed in both $\overline{\rho U_\theta'' U_\theta''}$ (Fig. 5.17(d)) and $\overline{\rho U_z'' U_z''}$ (Fig. 5.17(f)). The

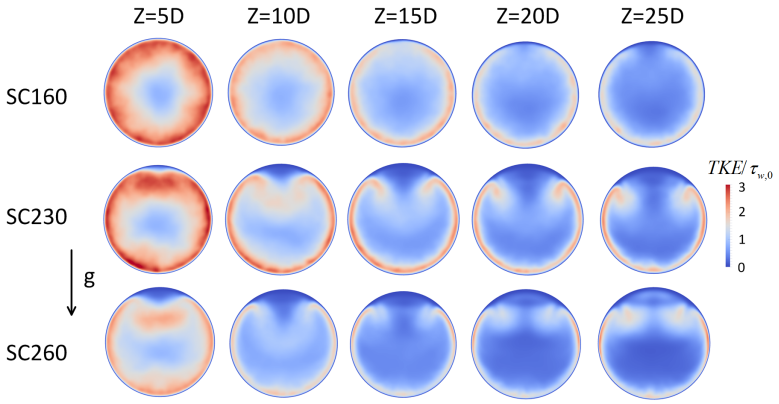

Figure 5.15: Evaluation of normalized turbulent kinetic energy $TKE/\tau_{w,0}$ in the downstream direction

peak value around $r/R = 0.4$ in all three components $\overline{\rho U_r'' U_r''}$, $\overline{\rho U_\theta'' U_\theta''}$ and $\overline{\rho U_z'' U_z''}$ indicates a significant interaction between both vortex centers, as demonstrated in Fig. 5.19, which has not been found in SC230.

Fig. 5.18 shows velocity vector plots of SC230 at $z = 25D$, colored by the TKE and its components in three directions $\overline{U_r''^2}$, $\overline{U_\theta''^2}$, $\overline{U_z''^2}$ respectively. The thin layer of flow closest to the wall (colored with dark blue) locates in the laminar sublayer and has the lowest TKE. It is transported to the top surface by secondary flow in circumferential direction. Also, it is collected near the top wall surface and builds up an area which shows lowest velocity fluctuation

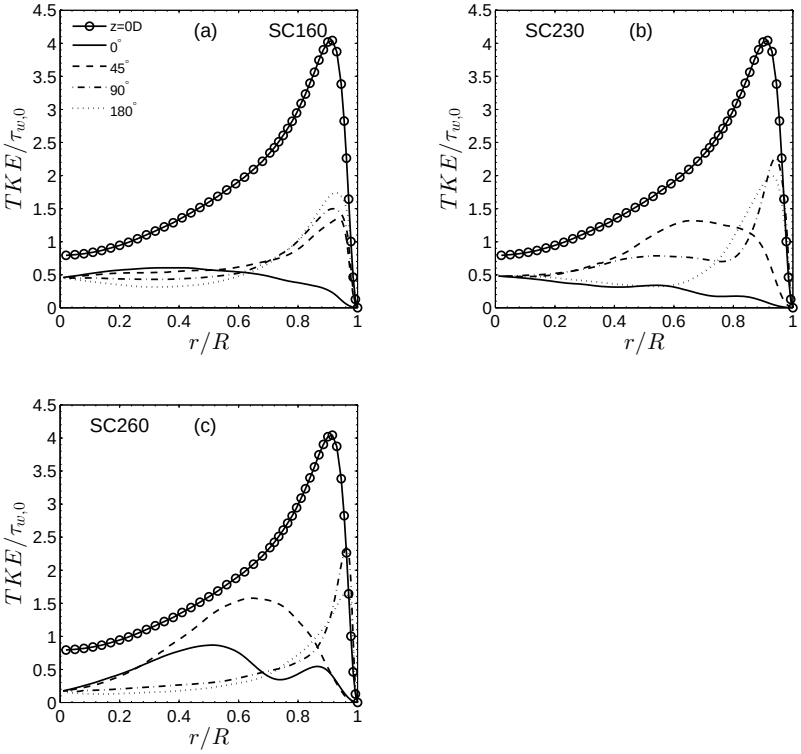

Figure 5.16: $TKE/\tau_{w,0}$ at $z = 25D$ of SC160 (a), SC230 (b) and SC260 (c), legend is identical as shown in (a)

in all three directions. Flow around the vortex centers of the secondary flow shows a relatively high TKE. The highest TKE is found between the wall and vortex centers laterally. The peak value of $\overline{U_r''^2}$ is observed in the flow near the vortex center at the side facing the axis of symmetry, where the secondary flow is bent towards the pipe center. The peak of $\overline{U_\theta''^2}$ also locates near the vortex centers but on the side facing to the wall. As the dominant component of the TKE, the distribution of $\overline{U_z''^2}$ shows strong similarity with that of TKE. In SC260 (Fig. 5.19), the peak value (colored with red) of TKE

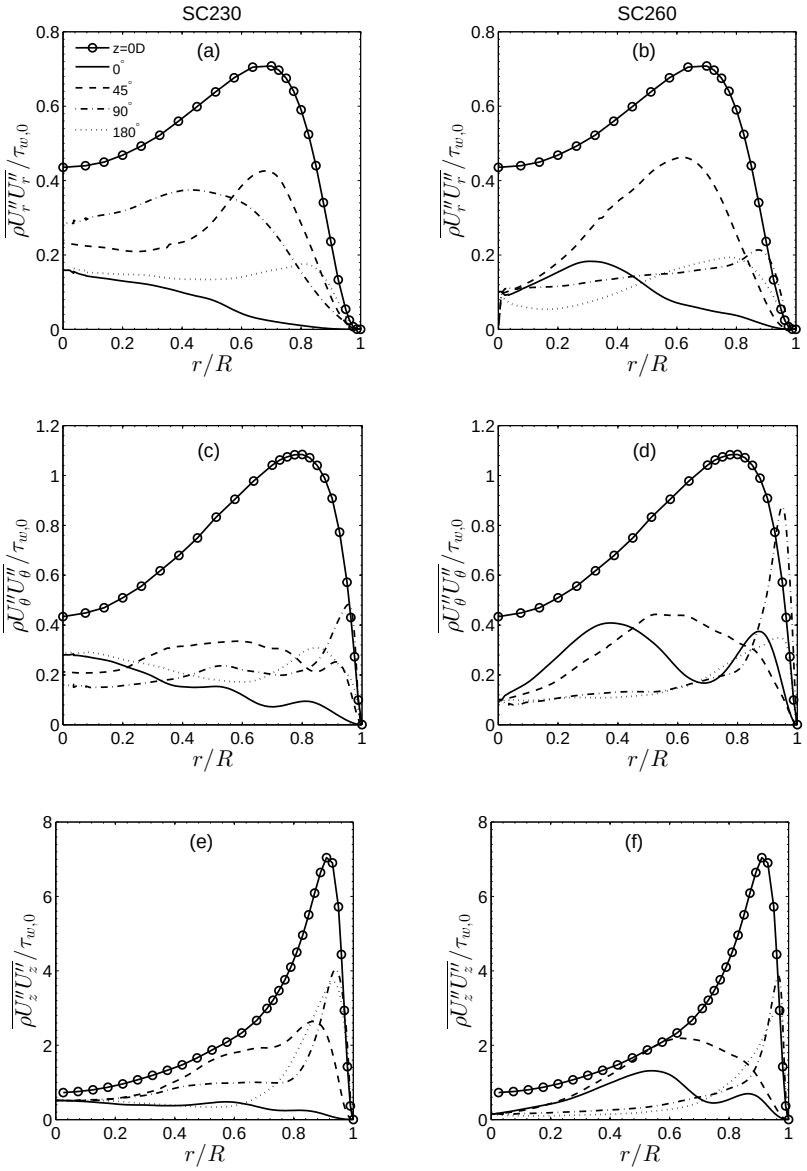

Figure 5.17: Velocity fluctuation $\overline{\rho U_r' U_r''}$, $\overline{\rho U_\theta' U_\theta''}$ and $\overline{\rho U_z' U_z''}$ at $z = 25D$ of SC230, and SC260, legend is identical as shown in (a)

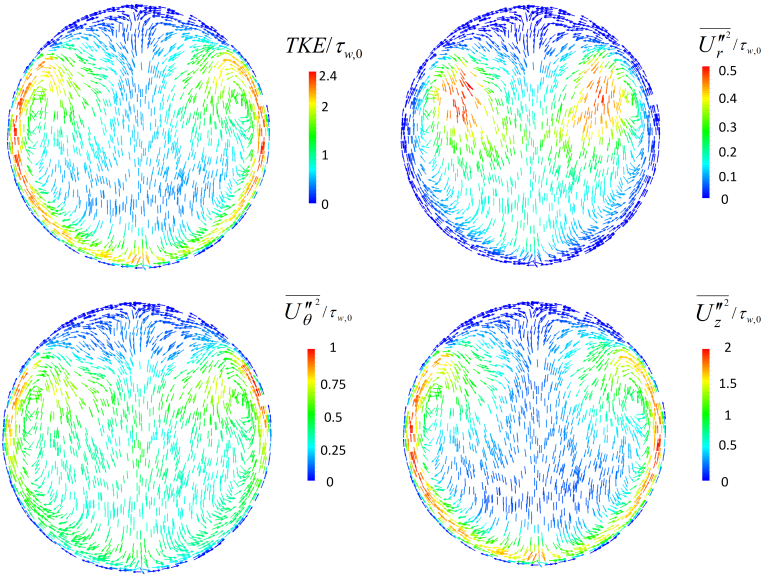

Figure 5.18: 2D velocity vector with flow statistics of SC230 at $z = 25D$

and its three components are found at a similar location as SC230.

A further quantification of turbulence statistics is the Reynolds shear stress $\overline{\rho U_r'' U_z''}$ at $z = 25D$, as shown in Fig. 5.20. In both cases, $\overline{\rho U_r'' U_z''}$ is strongly depressed in $\theta = 0°$ but shows a obvious peak value in $\theta = 45°$. A higher peak of $\overline{\rho U_r'' U_z''}$ in SC260 as compared to SC230 indicates a stronger turbulence mixing brought by the secondary flow at this position.

The modification of turbulence intensity plays also an important role for the convective heat transfer. Fig. 5.17 shows the turbulent heat flux in radial direction $\overline{\rho U_r'' h''}$ at $z = 25D$. In $\theta = 0°$ direction, the peak value of $\overline{\rho U_r'' h''}$ disappears in SC230, which indicates a weakened transport of heat flux from

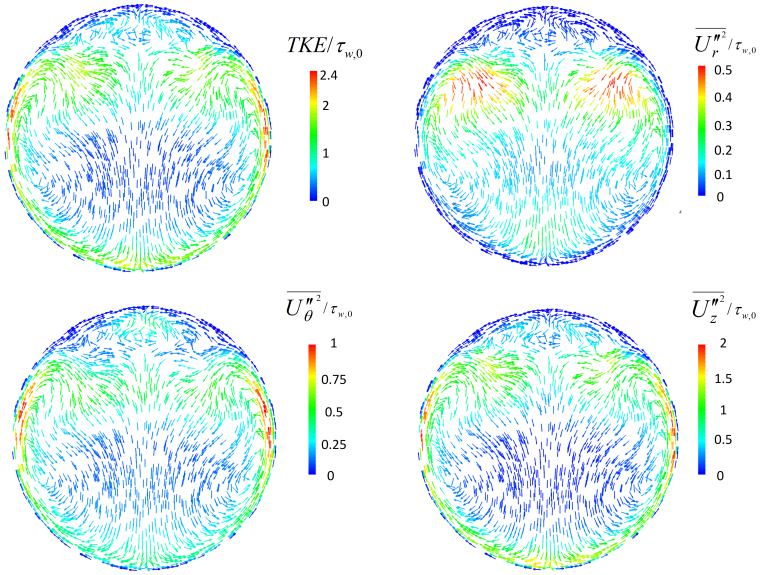

Figure 5.19: 2D velocity vector with flow statistics of SC260 at $z = 25D$

wall to the pipe center. In SC260, $\overline{\rho U_r'' h''}$ in $\theta = 0°$ is higher than that in SC230 and shows a similar two-peak distribution as the TKE in Fig. 5.16, which suggests a improved turbulent heat transfer in this case.

Production rate of turbulent kinetic energy Pk at different circumferential position on $z = 25D$ is shown in Fig. 5.22, where Pk is defined as $Pk = -\overline{\rho U_i'' U_j''} \frac{\widetilde{U}_i}{x_j}$. The isothermal flow at $z = 0D$ is marked with symbol as a reference. In SC230, Pk almost vanishes in $\theta = 0°$, which explains the significantly reduced TKE at this position in Fig. 5.16. The profile in $\theta = 45°$ shows a sign change near $r/R = 0.8$, which is the result of sign change of Reynolds shear stress $\overline{\rho U_r'' U_z''}$ in Fig. 5.20. Pk in $\theta = 90°$ is with a reduced

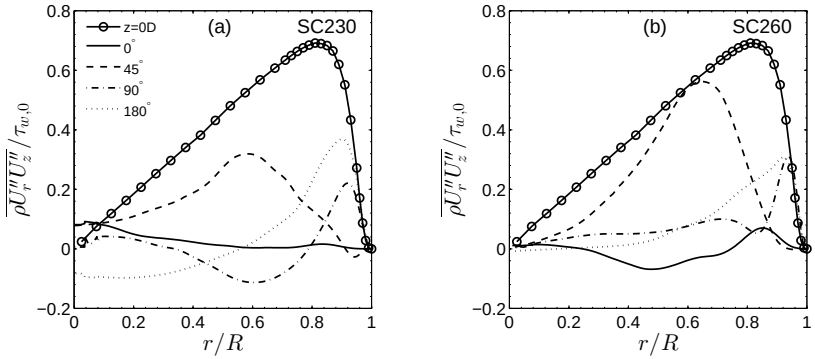

Figure 5.20: Reynolds shear stress $\overline{\rho U_r'' U_z''}/\tau_{w,0}$ at $z = 25D$, legend is identical as shown in (a)

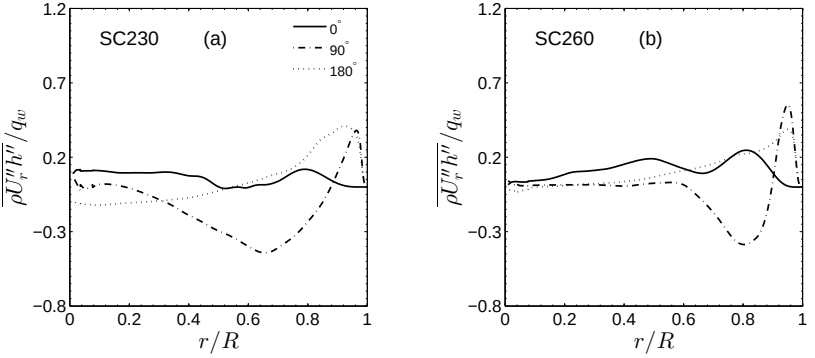

Figure 5.21: Turbulent heat flux $\overline{\rho U_r'' h''}/q_w$ at $z = 25D$, legend is identical as shown in (a)

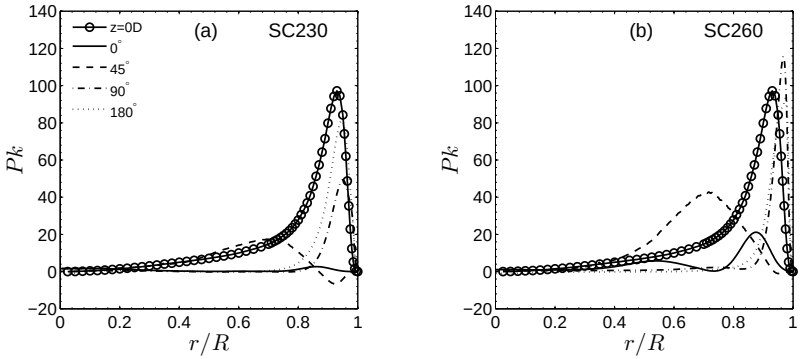

Figure 5.22: Circumferential distribution of Pk (Kg/m^3 s) at $z = 25D$ of SC230 (a), and SC260 (b), legend is identical as shown in (a)

peak value, while Pk at 180° holds its peak as the isothermal flow. For the pipe bulk area $0 < r/R < 0.9$, P_k is significantly reduced in $\theta = 0°$, 90°, and 180°. In SC260, P_k shows a slight double peak character in $\theta = 0°$, which shows similarity as the Reynolds shear stress $\overline{\rho U_r'' U_z''}$ in Fig. 5.20)(b). In $\theta = 45°$, Pk shifts its peak to $r/R = 0.7$ under the influence of secondary flow. In $\theta = 90°$ and 180°, narrow peak with a maximum close to the original value is observed in the figure.

The gravity force contributes explicitly to the turbulence with its buoyancy production term $BPk = g\overline{\rho' U_i'}$, as depicted in Fig. 5.23. Compared to shear production for turbulence Pk, BPk is an order of magnitude lower. It points out that the direct contribution from buoyancy to turbulence is small. In $\theta = 0°$, BPk shows a flat distribution close to zero. The peak of BPk in $\theta = 90°$ corresponds to the secondary flow along the pipe wall. In $\theta = 45°$, a sign change of BPk is observed, which is quite similar as Pk in the same position.

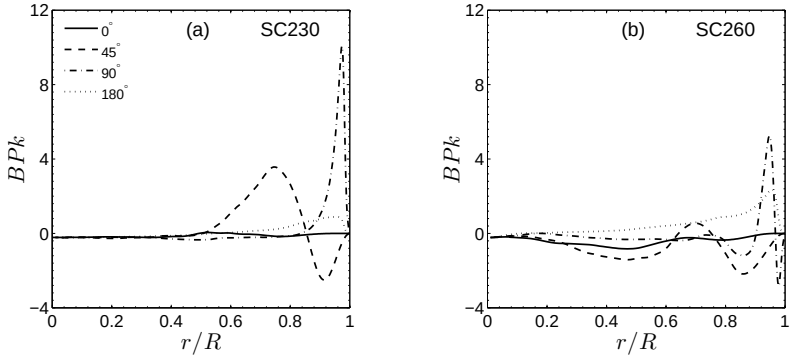

Figure 5.23: Circumferential distribution of BPk (Kg/m^3 s) at $z = 25D$ of SC230 (a), and SC260 (b), legend is identical as shown in (a)

5.4 Summary

In the present paper, heat transfer to supercritical CO_2 in a horizontal pipe has been investigated using Direct Numerical Simulation (DNS) for the first time. A well-resolved DNS eliminates the uncertainty brought by turbulence modeling and gives the opportunity to discover the stratification in turbulent flow field directly. Such small pipe diameter (D =1 mm, 2mm) and moderately low inlet Reynolds number ($Re_0 = 5400$) are applied as the flow channels in the compact heat exchangers (PCHE). In our simulations, inlet flow temperature T_0 is chosen slightly lower than the pseudo-critical temperature T_{pc}. The following interesting points are concluded from the current research:

1. The Wall temperature T_w is found to be strongly variable in the circumferential direction. T_w is significantly higher on the top surface than on the bottom surface. A strong buoyancy effect is found in the pipe with larger diameter (SC230 and SC260). Buoyancy also leads to an inhomogeneously distributed skin friction coefficient C_f in the circumferential direction.

2. As a result of buoyancy, flow stratification occurs in the pipe flow. A secondary flow is built up due to density differences and transports the heated

flow to the top surface. Therefore, high-temperature flow with low density is accumulated in this region, which explains the high wall temperature on the top wall.

3. The streamwise velocity field $\widetilde{U}_z$ is also modified by the flow stratification. Low-velocity flow close to the circumferential wall is heated initially and transported to the top by the secondary flow. High-velocity bulk flow settles at the bottom as a result of high density. In SC230 and SC260, an anchor-shape high-velocity profile is observed as a result of the motion of low-velocity flow $\widetilde{U}_z$ near the wall.

4. This modification of average velocity field has an influence to the flow turbulence in case SC230. Reduced velocity gradient near the top wall prevents the turbulence production by shear. As a result, turbulent kinetic energy is strongly suppressed which is so in the field of radial turbulent heat flux in this direction $\theta = 0°$. It indicates an attenuated convective heat transfer in this direction and enhances the flow stratification.

Chapter 6

Conclusion

Using supercritical fluid in a power cycle is widely considered as an advanced solution for energy conversion. The knowledge about heat transfer with supercritical fluid is still insufficient until now and it owns great potential of research from the prospective of fluid mechanics. Numerous interesting phenomena have been observed but lack of further study, including deteriorated heat transfer, relaminarization, transition and flow acceleration. Using DNS enables us to discover these mysteries accurately. In the present study, an efficient numerical solver for DNS is developed based on the open-source CFD package OpenFOAM. This solver is implemented to handle the heated incompressible flow with strong property variation.

For code validation, a series of cases of air flow in the pipe at $Re_0 = 4240$ and 6000 is simulated at first. The conditions are chosen to represent the experiment by Shehata and McEligot [SM95] closely, differing slightly from other DNS studies. Results from the present DNS are in close agreement with measured data from the experiments. A slight discrepancy is the result of imposing a constant wall heat flux instead of the varying wall heat flux of the experiment. The turbulent pipe flow is relaminarized in the downstream direction when a strong wall heat flux is applied, as in Run445. The apparent

laminarization is confirmed by decreased Nusselt number Nu, laminarized velocity (U_{VD}^{+})/temperature profiles (θ^{*}) and decreased turbulent kinetic energy. The cases are considered as dominant forced-convection, so the flow relaminarization is not due to buoyancy effects. This aspect is demonstrated by comparing various statistics between Run445 and Run445F. Unlike conventional wall coordinates as used in previous studies, a new semi-local wall coordinate is used to treat the local property variations in the transformation. With this definition, the apparent flow relaminarization is observed in both velocity and temperature profiles in contrast to earlier studies. Similarities between the profiles can be seen, enabling us to observe the changes of both fields in the process of laminarization. When the flow is relaminarized, the turbulence intensity is suppressed, consistent with reduced production rates of turbulent kinetic energy. Compared with this TKE production, the buoyancy production is significantly smaller. The quasi-laminar flow shows a two-layer character, which has not been shown before. Very long streaks are observed near the wall and they seem to separate the pipe flow into two layers. The near-wall layer becomes thicker and the turbulence in this layer shows increased anisotropy in the streamwise and circumferential directions. Outside the near-wall layer, the flow turbulence tends towards isotropy.

In the next part of the thesis, DNS of supercritical CO_2 flow in vertical pipes is presented. The inlet Reynolds number is fixed at $Re_0 = 5400$ to fill the dimensionless resolution requirement. The inlet flow temperature T_0 is chosen slightly lower than the pseudo-critical temperature T_{pc}. Cases under various simulation conditions are considered. Statistics of a strongly heated upward flow V22U shows the development of flow relaminarization and followed by a transition. The spectral analysis shows attenuated long waves and enhanced short waves in the relaminarized flow. Various flow field are included for a qualitative analysis of turbulence field. The turbulence structures are significantly modified in the streamwise direction. And they distinguish with each other in forced-convection, upward and downward flows.

The DNS study of heated supercritical CO_2 in a horizontal pipe is for the first time according to the author's knowledge. Such small pipe diameter

(D =1 mm, 2mm) and moderately low inlet Reynolds number ($\mathrm{Re}_0 = 5400$) are applied as the flow channels in the compact heat exchangers (PCHE). The Wall temperature T_w is found to be strongly variable in the circumferential direction. T_w is significantly higher on the top surface than on the bottom surface. A strong buoyancy effect is found in the pipe with larger diameter (SC230 and SC260). Buoyancy also leads to an inhomogeneously distributed skin friction coefficient C_f in the circumferential direction. As a result of buoyancy, flow stratification occurs in the pipe flow. A secondary flow is built up due to density differences and transports the heated flow to the top surface. Therefore, high-temperature flow with low density is accumulated in this region, which explains the high wall temperature on the top wall. The streamwise velocity field $\widetilde{U}_z$ is also modified by the flow stratification. Low-velocity flow close to the circumferential wall is heated initially and transported to the top by the secondary flow. High-velocity bulk flow settles at the bottom as a result of high density. In SC230 and SC260, an anchor-shape high-velocity profile is observed as a result of the motion of low-velocity flow $\widetilde{U}_z$ near the wall. This modification of average velocity field has an influence to the flow turbulence in case SC230. Reduced velocity gradient near the top wall prevents the turbulence production by shear. As a result, turbulent kinetic energy is strongly suppressed which is so in the field of radial turbulent heat flux in this direction $\theta = 0°$. It indicates an attenuated convective heat transfer in this direction and enhances the flow stratification.

Bibliography

[ACH16] G. Araya, L. Castillo, and F. Hussain. "DNS of Turbulent Boundary Layers in the Quasi-Laminarization Process." In: *Progress in Wall Turbulence 2*. Ed. by M. Stanislas, J. Jimenez, and I. Marusic. Vol. 23. ERCOFTAC Series. Springer International Publishing, 2016, pp. 63–71. URL: http://dx.doi.org/10.1007/978-3-319-20388-1%5C_5 (cit. on p. 30).

[AH76] G. A. Adebiyi and W. B. Hall. "Experimental investigation of heat transfer to supercritical pressure carbon dioxide in a horizontal pipe." In: *International Journal of Heat and Mass Transfer* 19.7 (1976), pp. 715–720. URL: http://www.sciencedirect.com/science/article/pii/001793107690123X (cit. on pp. 73, 81).

[Bae16] Y. Y. Bae. "A new formulation of variable turbulent Prandtl number for heat transfer to supercritical fluids." In: *International Journal of Heat and Mass Transfer* 92 (2016), pp. 792–806 (cit. on p. 5).

[BF09] M. Bazargan and D. Fraser. "Heat transfer to supercritical water in a horizontal pipe: modeling, new empirical correlation, and comparison against experimental data." In: *Journal of Heat Transfer* 131.6 (2009), p. 061702 (cit. on p. 73).

[BK09] Y.-Y. Bae and H.-Y. Kim. "Convective heat transfer to CO_2 at a supercritical pressure flowing vertically upward in tubes and an annular channel." In: *Experimental Thermal and Fluid Science* 33.2 (2009), pp. 329–339 (cit. on pp. 4, 6).

[BYC05] J. H. Bae, J. Y. Yoo, and H. Choi. “Direct numerical simulation of turbulent supercritical flows with heat transfer.” In: *Physics of Fluids* 17.10 (2005), p. 105104 (cit. on pp. 6, 11, 13, 52, 54, 75, 76).

[BYCM06] J. H. Bae, J. Y. Yoo, H. Choi, and D. M. McEligot. “Effects of large density variation on strongly heated internal air flows.” In: *Physics of Fluids* 18.7 (2006), p. 075102 (cit. on pp. 24, 25, 27, 29, 34).

[CCB73] A. D. Carr, M. A. Connor, and H. O. Buhr. “Velocity, Temperature, and Turbulence Measurements in Air for Pipe Flow With Combined Free and Forced Convection.” In: *Journal of Heat Transfer* 95.4 (1973), pp. 445–452 (cit. on p. 23).

[CKY07] X. Cheng, B. Kuang, and Y. Yang. “Numerical analysis of heat transfer in supercritical water cooled flow channels.” In: *Nuclear Engineering and Design* 237.3 (2007), pp. 240–252 (cit. on pp. 5, 73).

[CL16a] X. Chu and E. Laurien. “Flow stratification of supercritical CO2 in a heated horizontal pipe.” In: *The Journal of Supercritical Fluids* (2016). Accepted (cit. on p. 71).

[CL16b] X. Chu and E. Laurien. “Investigation of Convective Heat Transfer to Supercritical Carbon Dioxide with Direct Numerical Simulation.” In: *High Performance Computing in Science and Engineering´ 15*. Springer, 2016, pp. 315–331 (cit. on pp. 11, 49).

[CLM16] X. Chu, E. Laurien, and D. McEligot. “Direct Numerical Simulation of Strongly Heated Air Flow in a Vertical Pipe.” In: *International Journal of Heat and Mass Transfer* (2016). Accepted (cit. on p. 21).

[CRL11] X. Cao, Z. Rao, and S. Liao. “Laminar convective heat transfer of supercritical CO_2 in horizontal miniature circular and triangular tubes.” In: *Applied Thermal Engineering* 31.14 (2011), pp. 2374–2384 (cit. on p. 73).

[DCH70] D.M. McEligot, C.W. Coon, and H.C. Perkins. “Relaminarization in tubes.” In: *International Journal of Heat and Mass Transfer* 13.2 (1970), pp. 431–433. URL: http://www.sciencedirect.com/science/article/pii/0017931070901183 (cit. on p. 23).

[DDH04] V. Dostal, M. J. Driscoll, and P. Hejzlar. “A Supercritical Carbon Dioxide Cycle for Next Generation Nuclear Reactors.” PhD thesis. Massachusetts Institute of Technology, 2004 (cit. on pp. 1, 2).

[DP05] R. B. Duffey and I. L. Pioro. “Experimental heat transfer of supercritical carbon dioxide flowing inside channels (survey).” In: *Nuclear Engineering and Design* 235.8 (2005), pp. 913–924 (cit. on pp. 1, 3).

[EUW+94] J. G. M. Eggels, F. Unger, M. H. Weiss, J. Westerwell, R. J. Adrian, R. Friedrich, and F. T. M. Nieuwstadt. “Fully developed turbulent pipe flow: a comparison between direct numerical simulation and experiment.” In: *Journal of Fluid Mechanics* 268 (1994), pp. 175–210 (cit. on pp. 27, 28, 77).

[FADH15] P. Forooghi, I. A. Abdi, M. Dahari, and K. Hooman. “Buoyancy induced heat transfer deterioration in vertical concentric and eccentric annuli.” In: *International Journal of Heat and Mass Transfer* 81 (2015), pp. 222–233 (cit. on p. 5).

[Few76] J. Fewster. “Mixed forced and free convective heat transfer to supercritical pressure fluids flowing in vertical pipes.” PhD thesis. The University of Manchester, 1976 (cit. on p. 5).

[FH13a] P. Forooghi and K. Hooman. “Effect of buoyancy on turbulent convection heat transfer in corrugated channels–A numerical study.” In: *International Journal of Heat and Mass Transfer* 64 (2013), pp. 850–862 (cit. on p. 5).

[FH13b] P. Forooghi and K. Hooman. “Numerical study of turbulent convection in inclined pipes with significant buoyancy influence.” In: *International Journal of Heat and Mass Transfer* 61 (2013), pp. 310–322 (cit. on p. 5).

[FLK16] P. F. Fischer, J. W. Lottes, and S. G. Kerkemeier. *nek5000 Web page*. 2016. URL: http://nek5000.mcs.anl.gov (cit. on p. 9).

[HCB95] P. G. Huang, G. N. Coleman, and P. Bradshaw. “Compressible turbulent channel flows: DNS results and modelling.” In: *Journal of Fluid Mechanics* 305 (1995), pp. 185–218 (cit. on p. 34).

[HJ69] W. B. Hall and J. Jackson. “Laminarization of a turbulent pipe flow by buoyancy forces.” In: *MECHANICAL ENGINEERING*. Vol. 91. 11. ASME-AMER SOC MECHANICAL ENG 345 E 47TH ST, NEW YORK, NY 10017. 1969, p. 66 (cit. on p. 3).

[HKB08] S. He, W. S. Kim, and J. H. Bae. “Assessment of performance of turbulence models in predicting supercritical pressure heat transfer in a vertical tube.” In: *International Journal of Heat and Mass Transfer* 51.19–20 (2008), pp. 4659–4675 (cit. on pp. 2, 5, 73, 74).

[HKJ08] S. He, W. S. Kim, and J. D. Jackson. “A computational study of convective heat transfer to carbon dioxide at a pressure just above the critical value.” In: *Applied Thermal Engineering* 28.13 (2008), pp. 1662–1675 (cit. on p. 5).

[Iss86] R. I. Issa. “Solution of the implicitly discretised fluid flow equations by operator-splitting.” In: *Journal of computational physics* 62.1 (1986), pp. 40–65 (cit. on p. 13).

[Jac13] J. D. Jackson. “Fluid flow and convective heat transfer to fluids at supercritical pressure.” In: *Nuclear Engineering and Design* 264 (2013), pp. 24–40 (cit. on pp. 3, 74).

[JLZL13] P.-X. Jiang, B. Liu, C.-R. Zhao, and F. Luo. “Convection heat transfer of supercritical pressure carbon dioxide in a vertical micro tube from transition to turbulent flow regime.” In: *International Journal of Heat and Mass Transfer* 56.1 (2013), pp. 741–749 (cit. on p. 4).

[JMB89] J.D. Jackson, M.A. Cotton, and B.P. Axcell. “Studies of mixed convection in vertical tubes.” In: *International Journal of Heat and Fluid Flow* 10.1 (1989), pp. 2–15. URL: http://www.sciencedirect.com/science/article/pii/0142727X89900490 (cit. on p. 23).

[JUH15] Y. Jin, M. F. Uth, and H. Herwig. “Structure of a turbulent flow through plane channels with smooth and rough walls: An analysis based on high resolution DNS results.” In: *Computers & Fluids* 107 (2015), pp. 77–88 (cit. on pp. 7, 10).

[KJL07a] J. K. Kim, H. K. Jeon, and J. S. Lee. “Wall temperature measurement and heat transfer correlation of turbulent supercritical carbon dioxide flow in vertical circular/non-circular tubes.” In: *Nuclear Engineering and Design* 237.15 (2007), pp. 1795–1802 (cit. on p. 4).

[KJL07b] J. K. Kim, H. K. Jeon, and J. S. Lee. “Wall temperature measurements with turbulent flow in heated vertical circular/non-circular channels of supercritical pressure carbon-dioxide.” In: *International Journal of Heat and Mass Transfer* 50.23-24 (2007), pp. 4908–4911 (cit. on p. 2).

[KLAC12] A. Kruizenga, H. Li, M. Anderson, and M. Corradini. “Supercritical Carbon Dioxide Heat Transfer in Horizontal Semicircular Channels.” In: *Journal of Heat Transfer* 134.8 (2012), p. 081802 (cit. on p. 73).

[KSCK14] E. Komen, A. Shams, L. Camilo, and B. Koren. “Quasi-DNS capabilities of OpenFOAM for different mesh types.” In: *Computers & Fluids* 96 (2014), pp. 87–104 (cit. on pp. 7, 10).

[LAC09] J. Licht, M. Anderson, and M. Corradini. “Heat Transfer and Fluid Flow Characteristics in Supercritical Pressure Water.” In: *Journal of Heat Transfer* 131.7 (2009), p. 072502. URL: http://dx.doi.org/10.1115/1.3090817 (cit. on pp. 2, 4).

[Lau16] E. Laurien. “Implicit Model Equation for Hydraulic Resistance and Heat Transfer including Wall Roughness.” In: *Journal of Nuclear Engineering and Radiation Science* 2.2 (2016), p. 021016 (cit. on p. 74).

[LHT+08] X. Li, K. Hashimoto, Y. Tominaga, M. Tanahashi, and T. Miyauchi. “Numerical Study of Heat Transfer Mechanism in Turbulent Supercritical CO2 Channel Flow.” In: *Journal of Thermal Science and Technology* 3.1 (2008), pp. 112–123 (cit. on p. 12).

[LJZZ10] Z.-H. Li, P.-X. Jiang, C.-R. Zhao, and Y. Zhang. “Experimental investigation of convection heat transfer of CO2 at supercritical pressures in a vertical circular tube.” In: *Experimental Thermal and Fluid Science* 34.8 (2010), pp. 1162–1171 (cit. on pp. 2, 4).

[LL11] S. Laizet and N. Li. “Incompact3d: A powerful tool to tackle turbulence problems with up to O (105) computational cores.” In: *International Journal for Numerical Methods in Fluids* 67.11 (2011), pp. 1735–1757 (cit. on p. 10).

[LLYC12] X. Lei, H. Li, S. Yu, and T. Chen. “Numerical investigation on the mixed convection and heat transfer of supercritical water in horizontal tubes in the large specific heat region.” In: *Computers & Fluids* 64 (2012), pp. 127–140 (cit. on p. 73).

[LLZZ13] X. Lei, H. Li, Y. Zhang, and W. Zhang. “Effect of Buoyancy on the Mechanism of Heat Transfer Deterioration of Supercritical Water in Horizontal Tubes.” In: *Journal of Heat Transfer* 135.7 (2013), p. 071703 (cit. on p. 73).

[LMF+11] “NIST chemistry WebBook.” In: *NIST standard reference database number 69*. Ed. by E. Lemmon, M. McLinden, D. Friend, P. Linstrom, and W. Mallard. Gaithersburg: National Institute of Standards and Technology, 2011. URL: http://webbook.nist.gov/chemistry/ (cit. on pp. 1, 3, 25).

[LSHZ13] J. Lee, Y. J. Seo, J. S. Hyung, and T. A. Zaki. “Effect of wall heating on turbulent boundary layers with temperature-dependent viscosity.” In: *Journal of Fluid Mechanics* 726 (2013), pp. 196–225 (cit. on pp. 7, 34).

[LWS98] T. S. Lund, X. Wu, and K. D. Squires. “Generation of Turbulent Inflow Data for Spatially-Developing Boundary Layer Simulations.” In: *J. Comput. Phys.* 140.2 (1998), pp. 233–258. URL: http://dx.doi.org/10.1006/jcph.1998.5882 (cit. on pp. 10, 74).

[LZ02] Liao, S. M. and T. S. Zhao. “Measurements of Heat Transfer Coefficients From Supercritical Carbon Dioxide Flowing in Horizontal Mini/Micro Channels.” In: *Journal of Heat Transfer* 124.3 (2002), pp. 413–420. URL: http://dx.doi.org/10.1115/1.1423906 (cit. on p. 73).

[MB12] M. Mohseni and M. Bazargan. “Modification of low Reynolds number k– turbulence models for applications in supercritical fluid flows.” In: *International Journal of Thermal Sciences* 51 (2012), pp. 51–62 (cit. on p. 5).

[MJ04] D. M. McEligot and J. D. Jackson. ““Deterioration” criteria for convective heat transfer in gas flow through non-circular ducts.” In: *Nuclear Engineering and Design* 232.3 (2004), pp. 327–333 (cit. on p. 30).

[MSF+09] S. Mylavarapu, X. Sun, J. Figley, N. Needler, and R. Christensen. “Investigation of High-Temperature Printed Circuit Heat Exchangers for Very High Temperature Reactors.” In: *Journal of Engineering for Gas Turbines and Power* 131.6 (2009), p. 062905. URL: http://dx.doi.org/10.1115/1.3098425 (cit. on p. 73).

[MSJM02] D. P. Mikielewicz, A. M. Shehata, J. D. Jackson, and D. M. McEligot. "Temperature, velocity and mean turbulence structure in strongly heated internal gas flows." In: *International Journal of Heat and Mass Transfer* 45.21 (2002), pp. 4333–4352 (cit. on p. 24).

[NPBP15] H. Nemati, A. Patel, B. J. Boersma, and R. Pecnik. "Mean statistics of a heated turbulent pipe flow at supercritical pressure." In: *International Journal of Heat and Mass Transfer* 83 (2015), pp. 741–752 (cit. on pp. 6, 11, 13).

[Ope15] OpenFOAM Foundation. *OpenFOAM User Guide*. 2015. URL: http://foam.sourceforge.net/docs/Guides-a4/UserGuide.pdf (cit. on pp. 7, 9, 13, 14, 25).

[PBSA15] A. Pucciarelli, I. Borroni, M. Sharabi, and W. Ambrosini. "Results of 4-equation turbulence models in the prediction of heat transfer to supercritical pressure fluids." In: *Nuclear Engineering and Design* 281 (2015), pp. 5–14 (cit. on pp. 2, 5).

[PCFR12] J. J. Pasch, T. M. Conboy, D. D. Fleming, and G. E. Rochau. *Supercritical CO2 recompression Brayton cycle: Completed assembly description*. 2012 (cit. on p. 2).

[PL16] S. Pandey and E. Laurien. "Heat transfer analysis at supercritical pressure using two layer theory." In: *The Journal of Supercritical Fluids* 109 (2016), pp. 80–86 (cit. on pp. 8, 74).

[PM75] K. R. Perkins and D. M. McEligot. "Mean temperature profiles in heated laminarizing air flows." In: *Journal of Heat Transfer* 97.4 (1975), pp. 589–593 (cit. on p. 23).

[PPBP15] A. Patel, J. W. R. Peeters, B. J. Boersma, and R. Pecnik. "Semi-local scaling and turbulence modulation in variable property turbulent channel flows." In: *Physics of Fluids* 27.9 (2015), p. 095101 (cit. on pp. 6, 34).

[PPS72] B. Petukhov, V. Protopopov, and V. Silin. "Experimental investigation of worsened heat-transfer conditions with the turbulent flow of carbon dioxide at supercritical pressure." In: *High Temperature* 10.2 (1972), pp. 304–310 (cit. on p. 3).

[RPP+16] M. Rohde, J. W. R. Peeters, A. Pucciarelli, A. Kiss, Y. F. Rao, E. N. Onder, P. Muehlbauer, A. Batta, M. Hartig, V. Chatoorgoon, R. Thiele, D. Chang, S. Tavoularis, D. Novog, D. McClure, M. Gradecka, and K. Takase. "A Blind, Numerical Benchmark Study on Supercritical Water Heat Transfer Experiments in a 7-Rod Bundle." In: *Journal of Nuclear Engineering and Radiation Science* 2.2 (2016), p. 021012. URL: http://dx.doi.org/10.1115/1.4031949 (cit. on p. 6).

[SG69] Shiralkar, B. S. and P. Griffith. "Deterioration in Heat Transfer to Fluids at Supercritical Pressure and High Heat Fluxes." In: *Journal of Heat Transfer* 91.1 (1969), pp. 27–36. URL: http://dx.doi.org/10.1115/1.3580115 (cit. on p. 3).

[SH00] W. Schoppa and F. Hussain. "Coherent structure dynamics in near-wall turbulence." In: *Fluid Dynamics Research* 26.2 (2000), pp. 119–139 (cit. on pp. 10, 74).

[SKSM00] S.-i. Satake, T. Kunugi, A. M. Shehata, and D. M. McEligot. "Direct numerical simulation for laminarization of turbulent forced gas flows in circular tubes with strong heating." In: *International Journal of Heat and Fluid Flow* 21.5 (2000), pp. 526–534 (cit. on pp. 23, 27).

[SM95] A. Shehata and D. M. McEligot. *Turbulence structure in the viscous layer of strongly heated gas flows*. Tech. rep. INEL-95/0223. 1995 (cit. on pp. 5, 21, 23–29, 31, 35, 47, 103).

[SM98] A. Shehata and D. M. McEligot. "Mean structure in the viscous layer of strongly-heated internal gas flows. Measurements." In: *International Journal of Heat and Mass Transfer* 41.24 (1998), pp. 4297–4313 (cit. on pp. 23, 24, 27, 31, 32).

[SSM+11] T. Schulenberg, J. Starflinger, P. Marsault, D. Bittermann, C. Maraczy, E. Laurien, J. L. à Nijeholt, H. Anglart, M. Andreani, M. Ruzickova, et al. "European supercritical water cooled reactor." In: *Nuclear engineering and design* 241.9 (2011), pp. 3505–3513 (cit. on p. 1).

[TB10] G. Tabor and M. Baba-Ahmadi. "Inlet conditions for large eddy simulation: a review." In: *Computers & Fluids* 39.4 (2010), pp. 553–567 (cit. on p. 11).

[VKDB14] V. Vuorinen, J.-P. Keskinen, C. Duwig, and B. Boersma. “On the implementation of low-dissipative Runge–Kutta projection methods for time dependent flows using OpenFOAM®.” In: *Computers & Fluids* 93 (2014), pp. 153–163 (cit. on pp. 7, 10).

[WM08] X. Wu and P. Moin. “A direct numerical simulation study on the mean velocity characteristics in turbulent pipe flow.” In: *Journal of Fluid Mechanics* 608 (2008), pp. 81–112 (cit. on pp. 50, 51, 77).

[WRV+10] S. A. Wright, R. F. Radel, M. E. Vernon, P. S. Pickard, and G. E. Rochau. *Operation and analysis of a supercritical CO2 Brayton cycle*. 2010 (cit. on pp. 1, 2).

[XLP+04] X. Xu, J. S. Lee, R. H. Pletcher, A. M. Shehata, and D. M. McEligot. “Large eddy simulation of turbulent forced gas flows in vertical pipes with high heat transfer rates.” In: *International Journal of Heat and Mass Transfer* 47.19-20 (2004), pp. 4113–4123 (cit. on p. 24).

[YOI+07] J. Yang, Y. Oka, Y. Ishiwatari, J. Liu, and J. Yoo. “Numerical investigation of heat transfer in upward flows of supercritical water in circular tubes and tight fuel rod bundles.” In: *Nuclear Engineering and Design* 237.4 (2007), pp. 420–430 (cit. on p. 73).

[Yoo13] J. Y. Yoo. “The Turbulent Flows of Supercritical Fluids with Heat Transfer.” In: *Annual Review of Fluid Mechanics* 45.1 (2013), pp. 495–525 (cit. on pp. 73, 74).

[YYC03] J. You, J. Y. Yoo, and H. Choi. “Direct numerical simulation of heated vertical air flows in fully developed turbulent mixed convection.” In: *International Journal of Heat and Mass Transfer* 46.9 (2003), pp. 1613–1627 (cit. on p. 23).

[ZMS12] F. Zonta, C. Marchioli, and A. Soldati. “Modulation of turbulence in forced convection by temperature-dependent viscosity.” In: *Journal of Fluid Mechanics* 697 (2012), pp. 150–174 (cit. on p. 6).

[ZOS12] F. Zonta, M. Onorato, and A. Soldati. “Turbulence and internal waves in stably-stratified channel flow with temperature-dependent fluid properties.” In: *Journal of Fluid Mechanics* 697.4 (2012), pp. 175–203 (cit. on p. 7).

Institut für Kernenergetik und
Energiesysteme

Universität Stuttgart
Pfaffenwaldring 31

D- 70569 Stuttgart